UNIVERSIDADE FEDERAL DO CEARÁ

TECHNOLOGY CENTER

DEPARTMENT OF TELEINFORMATICS ENGINEERING

DIEGO DA MOTA COLARES

THE INFLUENCE OF SrTiO$_3$ ADDITION ON THE DIELECTRIC PROPERTIES OF Ba$_2$TiSi$_2$O$_8$ FOR HIGH FREQUENCY MICROWAVE COMPONENTS

FORTALEZA

2025

DIEGO DA MOTA COLARES

THE INFLUENCE OF SrTiO$_3$ ADDITION ON THE DIELECTRIC PROPERTIES OF Ba$_2$TiSi$_2$O$_8$ FOR HIGH FREQUENCY MICROWAVE COMPONENTS

Thesis presented to the Graduate Program in Teleinformatics Engineering at Universidade Federal do Ceará, as a partial requirement for obtaining the title of Doctor in Teleinformatics Engineering. Concentration area: Applied Electromagnetism.
Advisor: Prof. Dr. Antonio Sergio Bezerra Sombra.

FORTALEZA

2025

DIEGO DA MOTA COLARES

THE INFLUENCE OF SrTiO$_3$ ADDITION ON THE DIELECTRIC PROPERTIES OF Ba$_2$TiSi$_2$O$_8$ FOR HIGH FREQUENCY MICROWAVE COMPONENTS

Thesis presented to the Graduate Program in Teleinformatics Engineering at Universidade Federal do Ceará, as a partial requirement for obtaining the title of Doctor in Teleinformatics Engineering. Concentration area: Applied Electromagnetism. Advisor: Prof. Dr. Antonio Sergio Bezerra Sombra.

Approved on 16/06/2025

Documento assinado digitalmente
gov.br **ANTONIO SERGIO BEZERRA SOMBRA**
Data: 16/06/2025 16:49:46-0300
Verifique em https://validar.iti.gov.br

———————————————————
ANTONIO SERGIO BEZERRA SOMBRA
UFC - Orientador

Documento assinado digitalmente
gov.br **JOSE CLAUDIO DO NASCIMENTO**
Data: 16/06/2025 18:55:24-0300
Verifique em https://validar.iti.gov.br

———————————————————
JOSE CLAUDIO DO NASCIMENTO
UFC - Examinador Interno

Documento assinado digitalmente
gov.br **FRANCISCO NIVALDO AGUIAR FREIRE**
Data: 17/06/2025 13:35:19-0300
Verifique em https://validar.iti.gov.br

———————————————————
FRANCISCO NIVALDO AGUIAR FREIRE
UFC - Examinador Externo ao Programa

Documento assinado digitalmente
gov.br **CLAUDIO LENZ CESAR**
Data: 16/06/2025 18:11:50-0300
Verifique em https://validar.iti.gov.br

———————————————————
CLAUDIO LENZ CÉSAR
UFRJ - Examinador Externo à Instituição

Documento assinado digitalmente
gov.br **HUMBERTO DIONISIO DE ANDRADE**
Data: 16/06/2025 18:33:28-0300
Verifique em https://validar.iti.gov.br

———————————————————
HUMBERTO DIONÍSIO DE ANDRADE
UFERSA - Examinador Externo à Instituição

To my parents, Maria da Conceição da Mota
and Francisco Pereira Colares.

ACKNOWLEDGMENTS

"Electricity flows through all things. The Universe is a symphony of alternating currents."

Nikola Tesla

ABSTRACT

This thesis investigated the structural, morphological, and dielectric properties of $Ba_2TiSi_2O_8$ (BTS) with $SrTiO_3$ (STO) additions (0, 5, 10, 15, and 20 wt%) across both radio frequency (RF, f < 300 MHz) and microwave (MW, 300 MHz < f < 300 GHz) ranges. The ceramic composites were synthesized via the solid-state reaction method, uniaxially pressed at 15.2 MPa into cylindrical disks, and sintered at 1200°C for 4 hours. Morphological analysis via Scanning Electron Microscopy (SEM) revealed distinct microstructural evolution with STO incorporation. X-ray diffraction studies were conducted for phase identification and structural refinement. Complex Impedance Spectroscopy (CIS) analysis correlated dielectric properties with microstructural features, where the Maxwell-Wagner-Sillars model best explained the observed behavior. The ceramic composites exhibited activation energies (E_a) ranging from 1.76 to 1.92 eV. Thermal capacitance coefficients (TCC) for 10-15% STO-added compositions fell within ±1500 ppm·°C^{-1}. Nyquist plots analyzed dielectric behavior, with grain and grain boundary effects modeled using equivalent circuits (CPE). For MW-range analysis, the temperature coefficient of resonant frequency (τ_f) obtained via the Silva-Fernandes-Sombra (SFS) method indicated optimal thermal stability for 3% STO addition (τ_f = +9.23 ppm·°C^{-1}), making it ideal for antenna applications. Hakki-Coleman measurements showed improved quality factors ($53.64 \leq Q \leq 110.50$), reduced loss tangents (tan δ), and permittivity (ε_r) values. Numerical simulations demonstrated >96% electromagnetic efficiency when the composites functioned as antennas.

Keywords: composites; capacitors; antennas.

RESUMO

Esta tese investigou as propriedades estruturais, morfológicas e dielétricas de $Ba_2TiSi_2O_8$ (BTS) com adições de $SrTiO_3$ (STO) em proporções de 0, 5, 10, 15 e 20% em peso, abrangendo as faixas de radiofrequência (RF, $f < 300$ MHz) e micro-ondas (MW, 300 MHz $< f < 300$ GHz). Os compósitos cerâmicos foram sintetizados por meio do método de reação em estado sólido, prensados uniaxialmente a 15,2 MPa em discos cilíndricos e sinterizados a 1200 °C por 4 horas. A análise morfológica, realizada por Microscopia Eletrônica de Varredura (MEV), revelou uma evolução microestrutural distinta com a incorporação de STO. Estudos de difração de raios X foram conduzidos para identificação de fases e refinamento estrutural. A análise por Espectroscopia de Impedância Complexa (CIS) correlacionou as propriedades dielétricas com as características microestruturais, sendo que o modelo de Maxwell-Wagner-Sillars foi o que melhor explicou o comportamento observado. Os compósitos cerâmicos apresentaram energias de ativação (Ea) variando entre 1,76 e 1,92 eV. Os coeficientes de capacitância térmica (TCC) para composições com 10–15% de STO ficaram dentro de ± 1500 ppm·°C^{-1}. Diagramas de Nyquist foram usados para analisar o comportamento dielétrico, modelando os efeitos do grão e das fronteiras de grão por meio de circuitos equivalentes com elementos de fase constante (CPE). Para a análise na faixa de micro-ondas, o coeficiente de temperatura da frequência ressonante (τ_f), obtido pelo método Silva-Fernandes-Sombra (SFS), indicou estabilidade térmica ideal para adição de 3% de STO ($\tau_f = +9,23$ ppm·°C^{-1}), tornando-o adequado para aplicações em antenas. As medições de Hakki-Coleman mostraram fatores de qualidade aprimorados ($53,64 \leq Q \leq 110,50$), tangentes de perdas (tan δ) reduzidas e valores de permissividade (ε_r) adequados. Simulações numéricas demonstraram eficiência eletromagnética superior a 96% quando os compósitos funcionaram como antenas.

Palavras-chave: compósitos; capacitores; antenas.

LIST OF FIGURES

LIST OF TABLES

LIST OF ABBREVIATIONS AND ACRONYMS

AC - Alternating Current

BW - Bandwidth

DC - Direct Current

DRA - Dielectric Resonator Antenna

EDX - Energy Dispersive X-ray Detector

EIS - Electrochemical Impedance Spectroscopy

HEM - Hybrid Electric Mode

HFSS - Ansoft's High Frequency Structure Simulator

ICDD - International Centre for Diffraction Data

ICSD - Inorganic Crystal Structure Database

ITS - Intelligent Transport Systems

LOCEM - Laboratory of Telecommunications and Materials Science & Engineering

LTCC - Low Temperature Co-fired Ceramic

SEM - Scanning Electron Microscopy

FEM - Finite Element Method

MW - Microwave

DR - Dielectric Resonator

RF - Radio Frequency

Rwp - Weighted Residual Error

TCC - Temperature Coefficient of Capacitance

TE - Transverse Electric Mode

TM - Transverse Magnetic Mode

VSWR - Voltage Standing Wave Ratio

LIST OF SYMBOLS

A - Area of parallel-plate capacitor [m²]

C - Capacitance [F]

C* - Complex electrical capacitance [F]

C' - Real part of capacitance [F]

C" - Imaginary part of capacitance [F]

D - Distance between parallel plates or dielectric thickness [m]

D - Diameter of dielectric disk resonator [m]

G* - Complex electrical conductance [S]

G' - Real part of conductance [S]

G" - Imaginary part of conductance [S]

I - Current flowing through the system [A]

I* - Complex current [A]

I_0 - Current amplitude [A]

Y - Admittance [S]

Y* - Complex electrical admittance [S]

Y' - Real part of admittance [S]

Y" - Imaginary part of admittance [S]

J_0, J_1, J_2 - Bessel functions of orders zero, one, and two

K_0, K_1, K_2 - Modified Bessel functions of orders zero, one, and two

L - Length of dielectric resonator [m]

L - Inductance [H]

l - Longitudinal field variations

m - Mass [kg]

m'_a - Displaced water mass [kg]

m_a - Water mass [kg]

m_s - Solid mass [kg]

$m_{p(a+s)}$ - Mass of water-solid system in pycnometer [kg]

n - Diffraction order

n - CPE phase exponent

P_a - Diffuse polarization [C/m²]

P_{as} - Static final diffuse polarization [C/m²]

Q - Electric charge [C]

q - Proportionality factor for CPE

Q_L - Total system loss

Q_u - Unloaded quality factor

Q_a - Dielectric losses

Q_c - Losses due to metal plate conductivity

Q_r - Radiation losses

Q_{ext} - External coupling losses

R - Radius of Debye semicircle model [Ω]

R - Electrical resistance element [Ω]

R_L - Wire length resistance [Ω]

R_p - Parallel resistance [Ω]

r_s - Series resistance [Ω]

R_{exp} - Expected R factor

S_{11} - Reflection coefficient

t - Time [s]

T - Curie temperature [K]

v - Volume [m³]

v_s - Solid volume [m³]

v'_a - Displaced water volume with solid in pycnometer [m³]

v - Capacitor volume [m³]

V - Applied potential difference or voltage [V]

V* - Complex voltage [V]

V_0 - Voltage amplitude [V]

Z - Impedance [Ω]

Z* - Complex impedance [Ω]

|Z| - Magnitude of complex impedance [Ω]

Z' - Real part of impedance [Ω]

Z" - Imaginary part of impedance [Ω]

α - Geometry/wavelength-dependent parameter

$α_L$ - Linear expansion coefficient

β - Geometry/wavelength-dependent parameter

B - Magnetic flux density [T]

D - Electric flux density [C/m²]

ε - Dielectric constant

ε_0 - Absolute permittivity of vacuum [F/m]

ε_s - Static dielectric constant (low frequency)

$\varepsilon\infty$ - Static dielectric constant (high frequency)

ε - Complex relative permittivity

ε' - Real part of dielectric constant

ε" - Imaginary part of dielectric constant

E - Electric field vector [V/m]

H - Magnetic field vector [A/m]

J - Electric current density vector [A/m²]

η - Electromagnetic efficiency

tan δ - Dielectric loss tangent

Δf - Bandwidth [Hz]

τ - Dielectric relaxation time [s]

τ_f - Temperature coefficient of resonant frequency [ppm/°C]

μ - Permeability of non-magnetic metal [H/m]

σ - Conductivity [S/m]

ρ - Density [kg/m³]

ρ_s - Solid density [kg/m³]

ρ_a - Water density at room temperature [kg/m³]

ρ - Resistivity [Ω·m]

λ - Wavelength [m]

λ_0 - Resonant wavelength in free space [m]

λ_9 - Guided wavelength in infinite dielectric rod [m]

χ - Quality factor of fit

ω - Angular frequency [rad/s]

ϕ - Phase angle between complex current and voltage [rad]

SUMARY

1 INTRODUCTION

Electroceramic materials are essential for radio frequency (RF) engineering circuits (1-3). Historically, the discovery of ferroelectricity in $BaTiO_3$ (barium titanate) ceramic matrices in 1942 marked a breakthrough in electronics, particularly for ceramic capacitor development, due to its colossal dielectric permittivity (4).

This has driven intense scientific efforts to develop novel ceramic composites through chemical reactions, as modern applications demand stringent parameters including high permittivity, low dielectric loss, and exceptional thermal stability (5).

The field underwent further transformation in the 1960s with ceramic dielectric resonators revolutionizing telecommunications. This advancement originated from Hakki and Coleman's pioneering microwave characterization method (6), which enabled replacement of bulky metallic microwave oscillator cavities with compact hybrid (metal-ceramic) electronic components.

Subsequent progress included the 1984 development of $(Zr,Sn)TiO_4$ electroceramics, exhibiting exceptional microwave properties ($\varepsilon_r \approx 38$, $Q \times f \approx 50,000$ GHz) and near-zero temperature coefficient of resonant frequency ($\tau_f = 0\pm5$ ppm/°C) (7). Recent studies suggest the feasibility of nanoscale dielectric antennas (NRAs) utilizing surface plasmon radiation in the terahertz regime (8).

Figure 1 - Ceramic resonators.

Source: Public domain image.

1.1 Ba$_2$TiSi$_2$O$_8$ Ceramic Matrix

Currently, barium titanium silicate Ba$_2$TiSi$_2$O$_8$ (BTS) is used in various interesting technological applications such as piezoelectric, optical and microwave devices. This material has been studied since 1965 when it was found in Fresno County, California (9). In 1976, Japanese researchers identified significant piezoelectric properties in BTS crystals with k_{15} = 0.28 (10). These properties indicated BTS as a good candidate for pressure sensors. In 2012, scientists presented a new method to prepare BTS as dense monolithic dielectrics or high-surface-area catalytic powders through a Pechini process (11).

Recently, the BTS ceramic matrix, produced via solid-state reaction, has been studied for radio frequency (RF) and microwave (MW) applications (12-14). However, achieving the ideal requirements for electronic devices in the RF and MW ranges remains a scientific challenge. Thus, it becomes necessary to combine different ceramic matrices to obtain ceramic composites with improved electrical properties and high thermal stability.

Figure 2 – Crystal structure of Ba$_2$TiSi$_2$O$_8$ ceramic matrix.
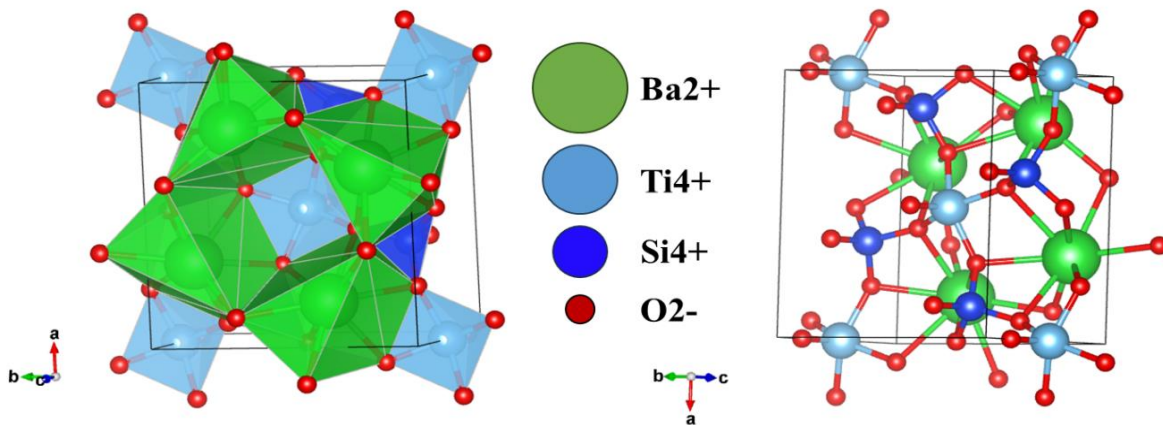
Source: Public domain image.

1.2 SrTiO₃ Ceramic Matrix

In the 1950s, the ceramic matrix $SrTiO_3$ (STO) was discovered, featuring a cubic perovskite crystal structure (ABO_3-type), where Ti^{4+} ions occupy the centers of oxygen octahedra while Sr^{2+} ions fill the interstitial voids. This structure undergoes a transition to a tetragonal phase below ~105 K due to crystal lattice instabilities (15).

STO's dielectric characteristics at radio frequencies are particularly notable, distinguished by low loss tangent ($\sim 10^{-4}$) and high relative permittivity (~290) at room temperature (16). These properties have motivated research demonstrating STO's potential applications in energy storage devices, capacitors, and telecommunications system components (17,18).

Additionally, STO exhibits superconductivity at temperatures between 0.05 K and 0.4 K through Niobium doping ($SrTi_{1-x}Nb_xO_3$), where Ti^{4+} is replaced by Nb^{5+} in the crystal lattice (19). Therefore, by combining STO with other ceramic matrices, it's possible to obtain composites with optimal dielectric parameters for both radio frequency and microwave applications.

Figure 3 – Crystal structure of SrTiO₃ ceramic matrix.
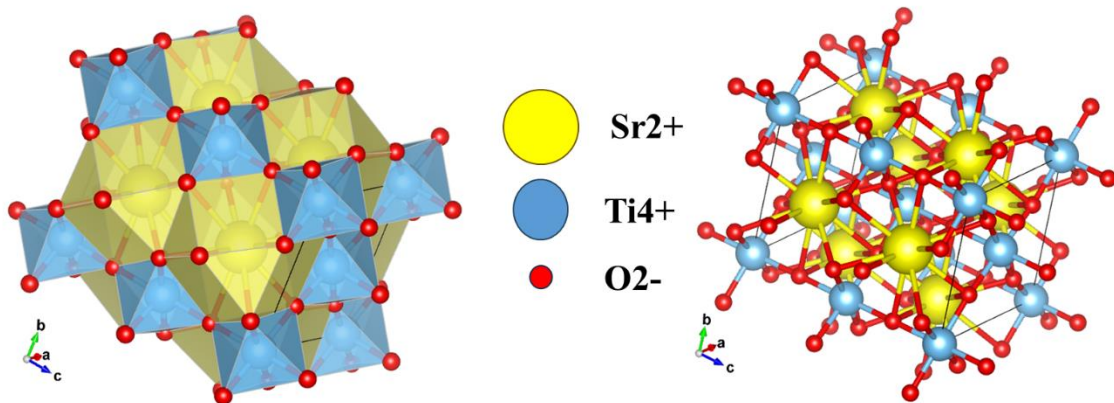
Source: Prepared by the author.

2 OBJECTIVES

2.1 General Objective

To develop solid-state synthesized $Ba_2TiSi_2O_8$ (BTS)-$SrTiO_3$ (STO) ceramic composites with optimized dielectric properties for applications as capacitors, temperature sensors, and dielectric resonator antennas (DRAs) operating at radio frequency (RF) and microwave (MW) ranges.

2.2 Specific Objectives

- Produce the $Ba_2TiSi_2O_8$ (BTS) ceramic matrix via solid-state reaction.
- Obtain ceramic composites by adding different molar proportions of $SrTiO_3$ to the BTS matrix.
- Identify and structurally characterize the formed phases through X-ray diffraction with Rietveld refinement.
- Study the sample microstructures using scanning electron microscopy (SEM)
- Investigate the electrical and dielectric properties of the composites in the radio frequency (RF) range via complex impedance spectroscopy (CIS), including parameters such as conductivity, dielectric permittivity, activation energy, and Nyquist plots.
- Analyze the thermal stability of the composites by evaluating the capacitance variation with temperature (TCC) in the RF range.
- Characterize the dielectric behavior in the microwave (MW) range, focusing on permittivity, loss tangent, and temperature coefficient of resonant frequency (τf)
- Analyze the temperature coefficient of resonant frequency (τ_f) of the BTS–STO composites.
- Investigate the feasibility of using BTS–STO composites as dielectric resonator antennas (DRAs) through experimental measurements and electromagnetic simulations using HFSS® software.

3 THEORETICAL BACKGROUND

3.1 X-Ray Diffraction (XRD)

X-ray diffraction is a materials characterization technique where X-ray beams strike a material. As a result, these beams scatter in specific directions due to interaction with the material's atomic planes (20). It is recommended that the material be in powdered and homogenized form (particles < 10 μm) to prevent the diffraction from favoring any particular direction. X-ray diffraction is governed by Bragg's Law. Thus, Equation 1 shows how this law describes this optical phenomenon:

$$n \cdot \lambda = 2\, d \sin(\theta) \tag{1}$$

Where n, λ, d e θ represent the diffraction order, wavelength, interplanar spacing, and incidence angle, respectively (20). Figure 4 illustrates the X-ray diffraction phenomenon in a crystalline sample.

Figure 4 – Bragg's Law representation showing X-ray diffraction process.
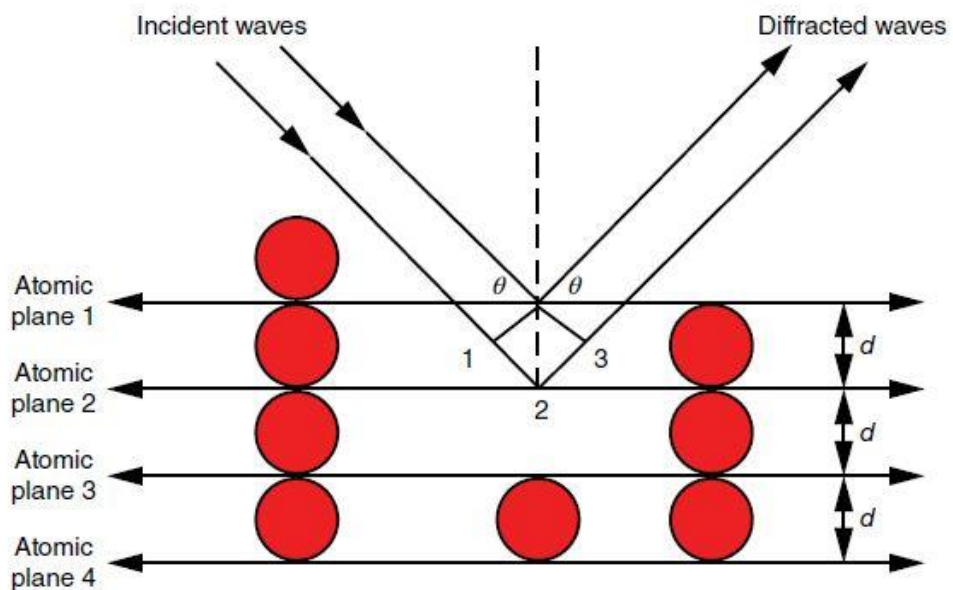
Source: Adapted from Pandey (2019).

From the raw X-ray diffraction data, a quantitative interpretation is nevertheless required. Thus, the Rietveld method was developed to numerically analyze the data and predict information about the materials' crystal structures (21).

Thus, the Rietveld method is based on an iterative numerical process that uses least-squares minimization algorithms to progressively fit a theoretical crystallographic model to the experimental diffraction pattern (21). An additional advantage of the Rietveld method compared to others is that it considers the entire diffraction profile, unlike other methods that analyze only isolated peaks (22).

Among the statistical parameters that are fundamental for a good refinement, we can mention Rwp (R-weighted pattern) [21, 22]:

$$R_{wp} = \sqrt{\frac{\sum_{i=1}^{N} w_i [y_i(obs) - yi(cal)]^2}{\sum_{i=1}^{N} w_i [y_i(obs)]^2}}$$

(2)

where y_i *(obs)* is the observed intensity, y_i *(cal)* is the calculated intensity, and w_i is the statistical weight. In addition to R_{wp} , there is also R_{exp} (expected R-factor) , calculated as (21, 22):

$$R_{exp} = \sqrt{\frac{N - P}{\sum_{i=1}^{N} w_i [y_i(obs)]^2}}$$

(3)

Where N is the total number of observed data points and P is the number of refined parameters. When R_{exp} approaches R_{wp} , the experimental measurements are indeed in good agreement with the theoretical model, indicating the precision of the experimental data. Additionally, a third statistical parameter called the Goodness of Fit (χ^2) can be defined mathematically as (21, 22):

$$\chi^2 = \left(\frac{R_{wp}}{R_{exp}}\right)^2$$

(4)

3.2 Scanning Electron Microscopy (SEM)

Scanning Electron Microscopy (SEM) is a technique that uses electron beams to acquire images and provide morphological information at scales ranging from micrometers to nanometers, making it extremely important for materials characterization (23). This remarkable detail in analysis is possible due to its much shorter wavelength compared to visible light. The SEM is divided into four main components, each with an important role in the image formation process.

The first component is the electron gun, which contains a source that generates the electron beam. This beam is then focused through a series of electromagnetic lenses, with each lens progressively reducing the electron beam diameter (24). The system also includes scanning coils that control the electron beam to examine the material's surface. Finally, a detector sends the signal to an amplifier connected to a computer, which displays the images produced by this process.

Figure 5 – SEM equipment schematic.
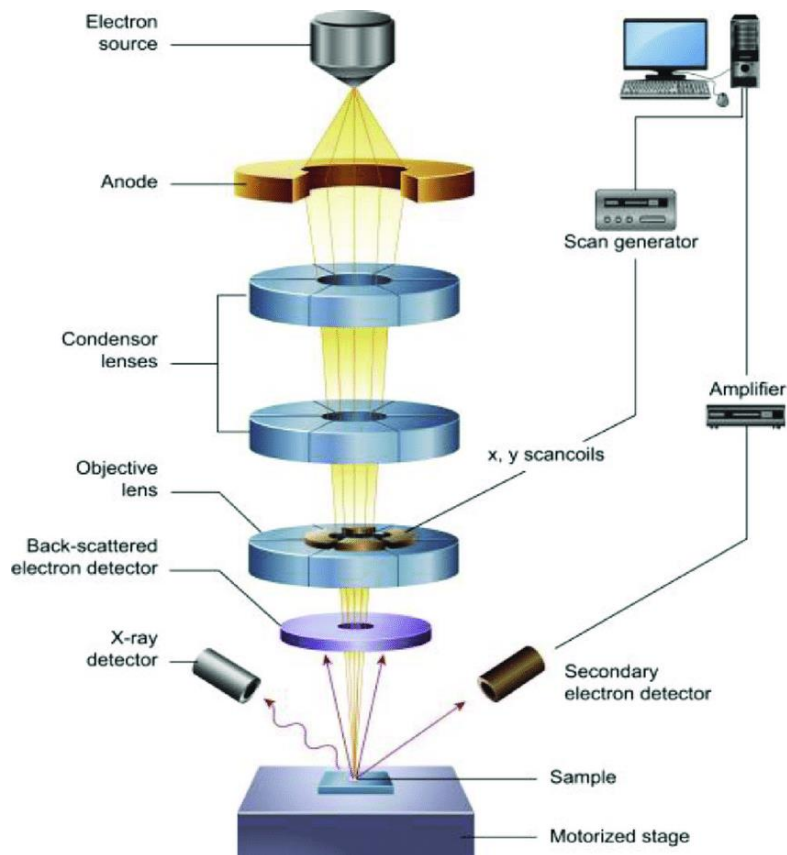
Source: Public domain.

3.3 Applied Electromagnetism

To better understand electroceramics, it is essential to comprehend how dielectric materials behave under electric and magnetic fields. This understanding is only possible through Maxwell's equations, which unified electromagnetism. The four Maxwell's equations are:

$$\nabla \cdot \boldsymbol{D} = \rho \tag{5}$$

$$\nabla \cdot \boldsymbol{B} = 0 \tag{6}$$

$$\nabla \times \boldsymbol{E} = \frac{-\partial \boldsymbol{B}}{\partial t} \tag{7}$$

$$\nabla \times \boldsymbol{H} = \boldsymbol{J} + \frac{\partial \boldsymbol{D}}{\partial t} \tag{8}$$

It is known that **D**, **B**, **E**, **H**, **J**, and ρ represent, respectively, electric flux density, magnetic flux density, electric field, magnetic field, net current density, and free charge density. Equation 5 is called Gauss's law for the electric field, whose interpretation states that electric charges are sources (or sinks) of electric field (25). Equation 6 is Gauss's law for the magnetic field; the understanding of this equation can be stated as: the magnetic field has no "sources", meaning there are no magnetic monopoles (25). Equation 7 is Faraday's law of induction; the statement of this law says that a time-varying magnetic field generates an electric field (25).

Finally, Equation 8 is the Ampère-Maxwell law, which was essential for predicting the propagation of electromagnetic waves in a vacuum (25). Moreover, there are also constitutive relations that enable the determination and understanding of materials' dielectric properties when subjected to electromagnetic fields (25). Mathematically, we have:

$$\boldsymbol{B} = \mu\boldsymbol{H} \tag{9}$$

$$\boldsymbol{D} = \varepsilon\boldsymbol{E} \tag{10}$$

$$\boldsymbol{J} = \sigma\boldsymbol{E} \tag{11}$$

The parameters μ, ε, and σ represent, respectively, the magnetic permeability, dielectric permittivity, and conductivity of the material (26). Thus, by measuring these variables, one can study the dielectric Properties.

Moreover, the magnetic permeability and dielectric permittivity of materials can assume relative values compared to those in a vacuum, denoted respectively μ_r e ε_r. According to the literature, the values of magnetic permeability and dielectric permittivity in a vacuum are: $\mu_r = 1{,}257 \times 10^{-6} H \cdot m^{-1}$ e $\varepsilon_0 = 8{,}854 \times 10^{-12} F \cdot m^{-1}$ [26]. Thus, mathematically we have:

$$\mu_r = \frac{\mu}{\mu_0} \tag{12}$$

$$\varepsilon_r = \frac{\varepsilon}{\varepsilon_0} \tag{13}$$

With the above physical definitions established, we can now introduce a vital parameter for electromagnetism: capacitance (C). By definition, capacitance represents a material's ability to store electric charge (Q) when subjected to an electric voltage (V) (27). Mathematically, this is expressed as:

$$C = \frac{Q}{V} \tag{14}$$

In an ideal parallel-plate capacitor, as illustrated in Figure 6 below, it is known that the capacitance depends on the dielectric's area dimensions (A) and material thickness (d) (27). Therefore, we can calculate the capacitance as:

$$C = \frac{\varepsilon A}{d} \tag{15}$$

Figure 6 – Ideal parallel plate capacitor representation.
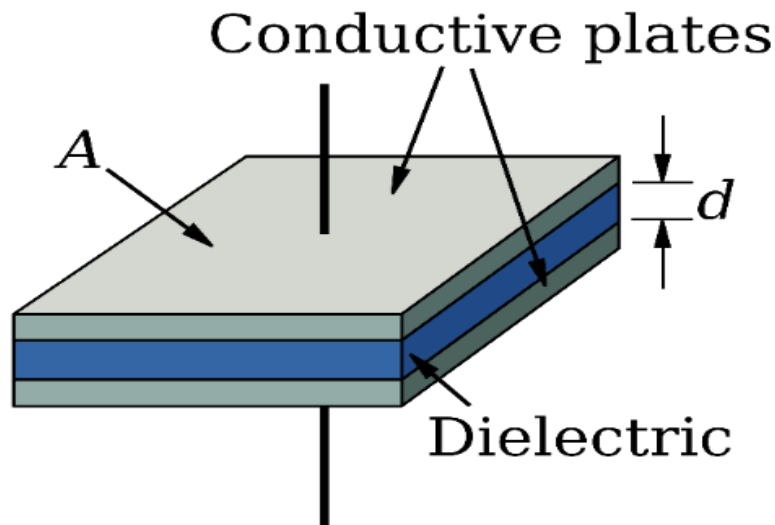
Source: Public domain.

When a material is subjected to an alternating current (AC) electric field, another highly important variable emerges: impedance (Z). To better explain this physical parameter, consider Figure 7, which illustrates an RLC circuit powered by an AC source.

Figure 7 – RLC circuit diagram.
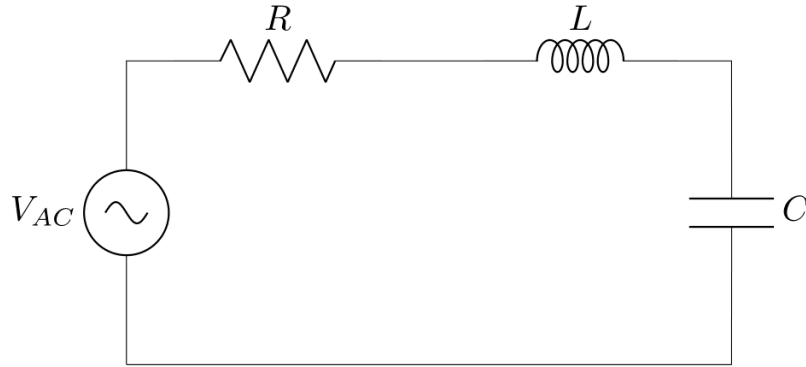
Source: Prepared by the author.

Therefore, impedance can be defined as a physical parameter that measures the total opposition an electrical circuit presents when traversed by alternating current (AC) with a specific angular velocity (ω) or frequency (f). When referring to the opposition of electric current that dissipates energy as heat (Joule effect) in the circuit, this corresponds to the element called resistance (R) (27).

However, when this opposition to electric current refers to capacitive (C) or inductive (L) elements, this variable is called reactance (X). The following equation clarifies this definition:

$$Z = R + jX \tag{16}$$

$$|Z| = \sqrt{R^2 + X^2} \tag{17}$$

As observed above, reactance represents the purely imaginary component of impedance, while resistance constitutes the purely real component (27). Naturally, the magnitude of impedance is used to measure the total opposition to current in the analyzed circuit Furthermore, the reactance component associated solely with the capacitor (C) is called capacitive reactance (X_C), while the component linked to the inductor (L) is termed inductive reactance (X_L). However, X_C e X_L exhibit opposite phases (27). Mathematically, these definitions are established as follows:

$$X = X_L - X_C \tag{17}$$

$$X_L = \omega L \tag{18}$$

$$X_C = \frac{1}{\omega C} \tag{19}$$

$$\omega = 2\pi f \tag{20}$$

$$\Rightarrow X = 2\pi f L - \frac{1}{2\pi f C} \tag{21}$$

Similarly, when a material is subjected to alternating current, its dielectric permittivity will also exhibit complex values, as occurs with impedance (27). Therefore, in this new context, the permittivity becomes:

$$\varepsilon^* = \varepsilon' - j\varepsilon'' \tag{22}$$

Where ε' is the real part and ε'' is the imaginary part. Here, the real part of permittivity is related to energy storage capacity, while the imaginary part is associated with energy dissipation as heat (20, 27). To better quantify this energy storage performance, we can further define the loss tangent (tan δ) and quality factor (Q) as:

$$\tan \delta = \frac{\varepsilon''}{\varepsilon'} \tag{23}$$

$$Q = \frac{1}{\tan \delta} = \frac{\varepsilon'}{\varepsilon''} \tag{24}$$

The higher the quality factor (Q), the greater the material's capacity to store energy per cycle before releasing it (20, 27). Furthermore, it is important to emphasize that dielectrics with high Q values are particularly suitable for applications as resonators, antennas, and sensors. Equation 25 demonstrates this precisely:

$$Q = 2\pi \frac{Stored\ energy}{Dissipated\ energy\ per\ cycle} \tag{25}$$

3.4 Radio Frequency Impedance Spectroscopy

By definition, Impedance Spectroscopy (EIS) is a materials characterization technique that measures the response of a sample's dielectric properties to an alternating current (AC) electrical signal across frequency ranges and temperature conditions (28). Consequently, EIS analysis begins with the complex impedance of a circuit. Through electromagnetic equations, it becomes possible to extract and study electrical parameters such as conductivity, permittivity, and loss tangent (28). Additionally, EIS can determine the transport mechanisms occurring in a material during polarization phenomena. A generic schematic of the EIS technique is shown in Figure 8.

Figure 8 – Schematic illustration of the EIS technique.
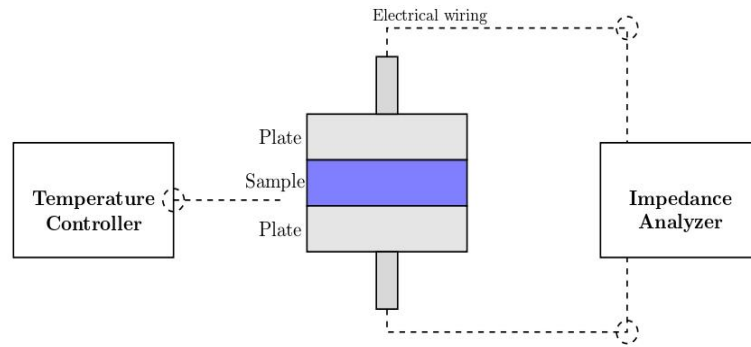
Source: Prepared by the author.

The capacitance of materials depends not only on current and frequency but also on temperature. Therefore, the TCC (Temperature Coefficient of Capacitance) is the parameter that indicates how much the capacitance changes with temperature variation (28). The TCC can be calculated as:

$$TCC = \left(\frac{C(T) - C_0}{C_0 \cdot (T - T_0)} \right) \times 10^6 [ppm/°C] \tag{25}$$

Capacitors can also be classified according to the TCC using standardized categories. For example, Class 1 capacitors have a TCC range of 0 ± 30 ppm/°C (29). According to the literature, materials exhibit different types of relaxations, which creates the need for models to fully understand this phenomenon (30). Examples of relaxation models include Debye, Cole-Cole, Cole-Davidson, Havriliak-Negami, and Maxwell-Wagner-Sillars (30).

3.5 Dielectric Relaxation Models

3.5.1 Debye Model

The first model to quantify the phenomenon of dielectric relaxation was proposed in 1929 by Debye. The Debye model describes the existence of a single relaxation time (τ), meaning it is a mono-exponential relaxation model (30). Therefore, this model is suitable for materials with dominant polarization. Mathematically, the model is expressed more clearly as follows (30):

$$\varepsilon^*(\omega) = \varepsilon_\infty + \frac{\varepsilon_s - \varepsilon_\infty}{1 + (j\omega\tau)} \tag{26}$$

Where ε_s is the static permittivity, and, ε_∞ is the high-frequency permittivity. The real and imaginary parts are given by Equations 26 and 27 (30):

$$\varepsilon'(\omega) = \varepsilon_\infty + \frac{\varepsilon_s - \varepsilon_\infty}{1 + (\omega\tau)^2} \tag{27}$$

$$\varepsilon''(\omega) = \frac{(\varepsilon_s - \varepsilon_\infty)(\omega\tau)}{1 + (\omega\tau)^2} \tag{28}$$

Figure 9 – Debye model plot.
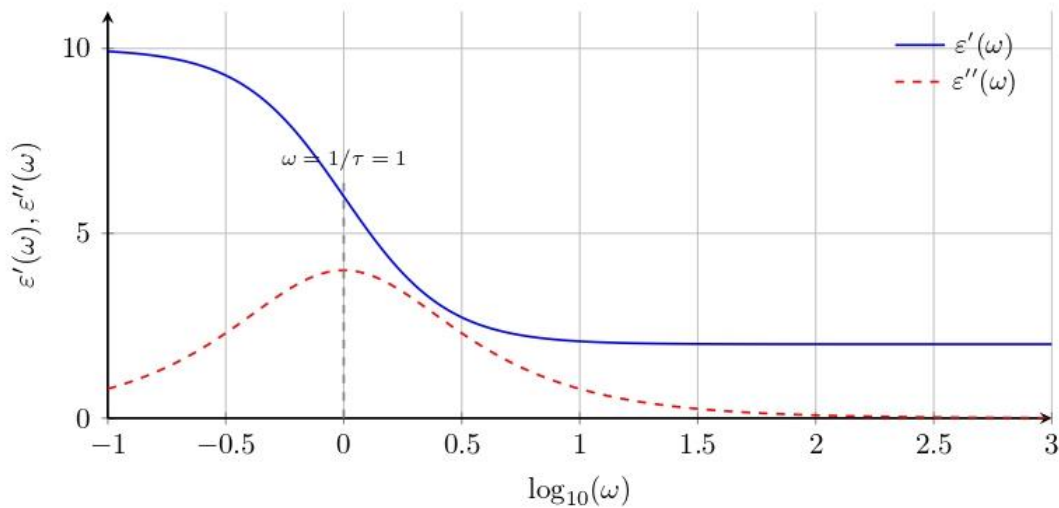
Source: Prepared by the author.

3.5.2 Cole-Cole Model

The Cole-Cole model introduces a new parameter $1 - \alpha$ within the Debye equation as an exponent, aiming to explain cases that the Debye model could not justify (31). The function of this parameter is to broaden the relaxation by considering dispersion in real systems.

Thus, the Cole-Cole model is focused on understanding dipole-dipole interactions (31). Equation 29 shows how this model was engineered, along with Figure 10, which illustrates the graph of this function (31).

$$\varepsilon^*(\omega) = \varepsilon_\infty + \frac{\varepsilon_s - \varepsilon_\infty}{1 + (j\omega\tau)^{1-\alpha}} \tag{29}$$

$$\varepsilon'(\omega) = \varepsilon_\infty + \frac{(\varepsilon_s - \varepsilon_\infty)[1 + (\omega\tau)^{1-\alpha}\sin(\frac{\alpha\pi}{2})]}{1 + 2(\omega\tau)^{1-\alpha}\sin(\frac{\alpha\pi}{2}) + (\omega\tau)^{2(1-\alpha)}} \tag{30}$$

$$\varepsilon''(\omega) = \frac{(\varepsilon_s - \varepsilon_\infty)(\omega\tau)^{1-\alpha}\cos(\frac{\alpha\pi}{2})}{1 + 2(\omega\tau)^{1-\alpha}\sin(\frac{\alpha\pi}{2}) + (\omega\tau)^{2(1-\alpha)}} \tag{31}$$

Figure 10– Cole-Cole model plot.
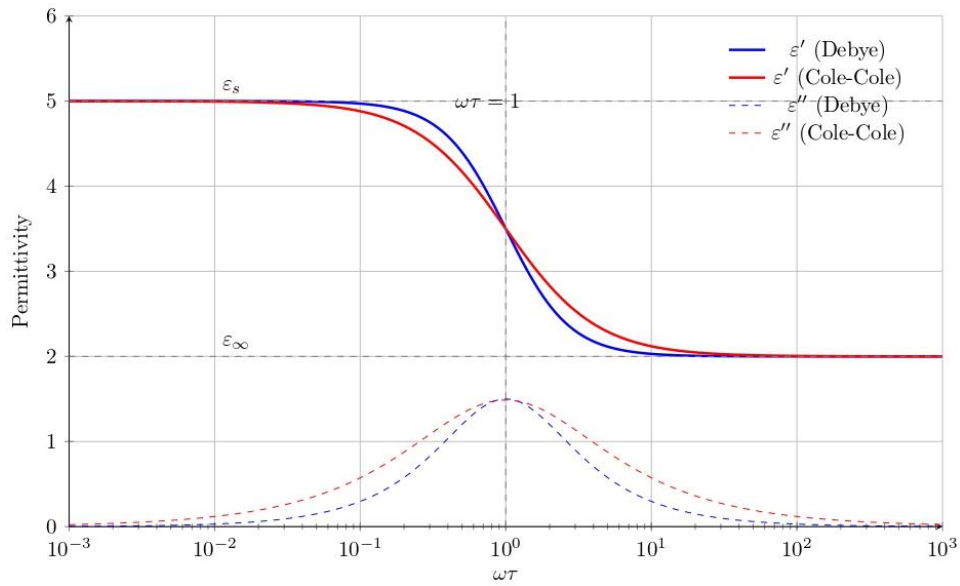
Source: Prepared by the author.

3.5.3 Cole-Davidson Model

Following the evolution of the models, we now have the Cole-Davidson model, which complements the Cole-Cole model. By introducing the variable β, which essentially determines the asymmetry of a material's relaxation times, it has been successfully applied to glycerin as well as in glasses and polymers (32).

Equation 32 shows how this model works mathematically (32):

$$\varepsilon^*(\omega) = \varepsilon_\infty + \frac{\varepsilon_s - \varepsilon_\infty}{1 + (j\omega\tau)^\beta} \tag{32}$$

By separating the real and imaginary parts, we have (32):

$$\varepsilon'(\omega) = \varepsilon_\infty(\varepsilon_s - \varepsilon_\infty)\cos(\beta\phi)(\omega\tau)\beta(\omega\tau)^{-\beta} \tag{33}$$

$$\varepsilon''(\omega) = \varepsilon_\infty(\varepsilon_s - \varepsilon_\infty)\sin(\beta\phi)(\omega\tau)\beta(\omega\tau)^{-\beta} \tag{34}$$

$$\phi = arctan(\omega\tau) \tag{35}$$

Figure 11 illustrates the graph of the Cole-Davidson model, showing how the real and complex parts behave.

Figure 11 – Cole-Davidson model plot.
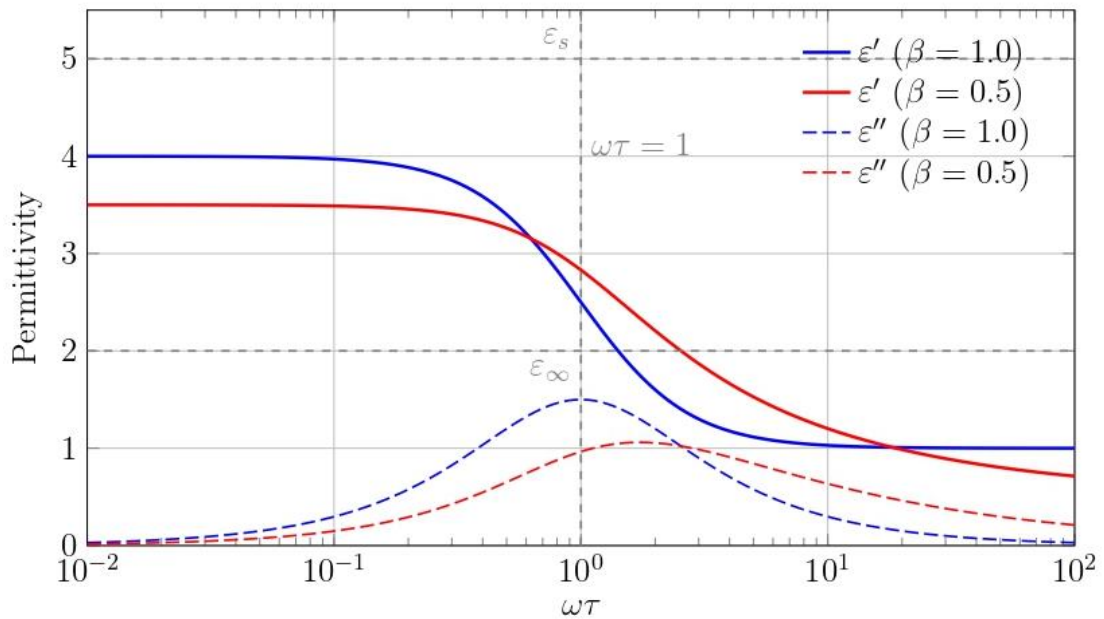
Source: Prepared by the author

3.5.4 Havriliak-Negami Model

The Havriliak-Negami (HN) model is a generalization of the previous models. Specifically, this model achieves better asymmetric distributions and broader relaxation times (33). The main materials to which this model is applied include: amorphous polymers, electrolytic solutions, and ceramics. Equations (36), (37), and (38) are, respectively, the complex permittivity, real permittivity, and imaginary permittivity (33).

$$\varepsilon^*(\omega) = \varepsilon_\infty + \frac{\varepsilon_s - \varepsilon_\infty}{[1 + (j\omega\tau)^{1-\alpha}]^\beta} \tag{36}$$

$$\varepsilon'(\omega) = \varepsilon_\infty + \frac{(\varepsilon_s - \varepsilon_\infty)[1 + \cos[\beta \cdot \theta(\omega)]}{[1 + 2(\omega\tau)^{1-\alpha}\sin\left(\frac{\alpha\pi}{2}\right) + (\omega\tau)^{2(1-\alpha)}]^{\beta/2}} \tag{37}$$

$$\varepsilon''(\omega) = \varepsilon_\infty + \frac{(\varepsilon_s - \varepsilon_\infty)[1 + \sin[\beta \cdot \theta(\omega)]}{[1 + 2(\omega\tau)^{1-\alpha}\sin\left(\frac{\alpha\pi}{2}\right) + (\omega\tau)^{2(1-\alpha)}]^{\beta/2}} \tag{38}$$

$$\theta(\omega) = arctan\left(\frac{(\omega\tau)^{1-\alpha}\cos\left(\frac{\alpha\pi}{2}\right)}{1 + (\omega\tau)^{1-\alpha}\sin\left(\frac{\alpha\pi}{2}\right)}\right) \tag{39}$$

Figure 12 illustrates the Havriliak-Negami graph, showing how the real and complex parts behave in relation to the other models previously mentioned.

Figure 12 – Havriliak-Negami model plot.
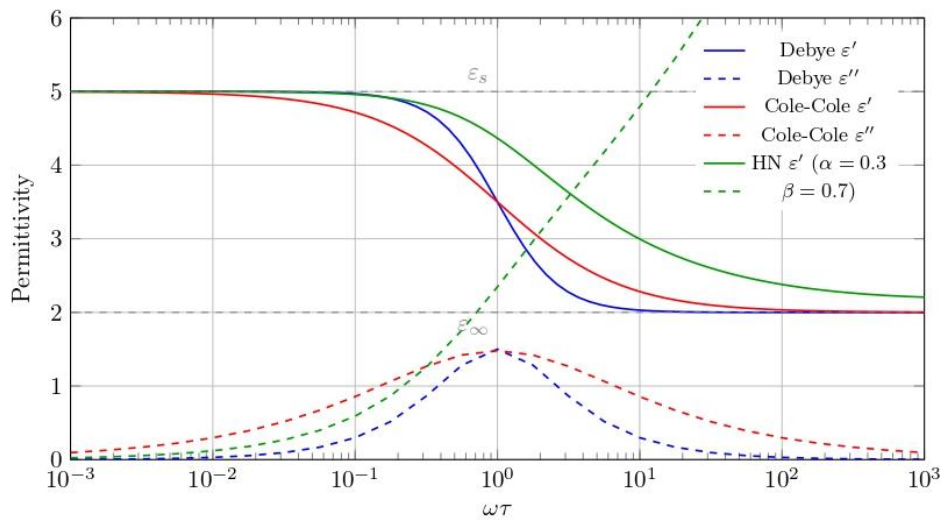
Source: Prepared by the author

3.5.5 Maxwell-Wagner-Sillars Model

In the literature, it is reported that the Maxwell-Wagner-Sillars (MWS) model defines the structure of materials as being composed of conductive grain layers interspersed with insulating grain boundaries (34). Thus, at low frequencies, charge carriers accumulate at the resistive grain boundaries, while at high frequencies, the charge carriers are located in the conductive grains, where they can move more freely (34). This model is effective for understanding the dielectric behavior where internal electrical heterogeneities occur in polycrystalline electroceramics (34). Figure 13 illustrates the description of this model, and Figure 14 shows the graphs of this model.

Figure 13 – Schematic Illustration of the Maxwell-Wagner-Sillars Model.
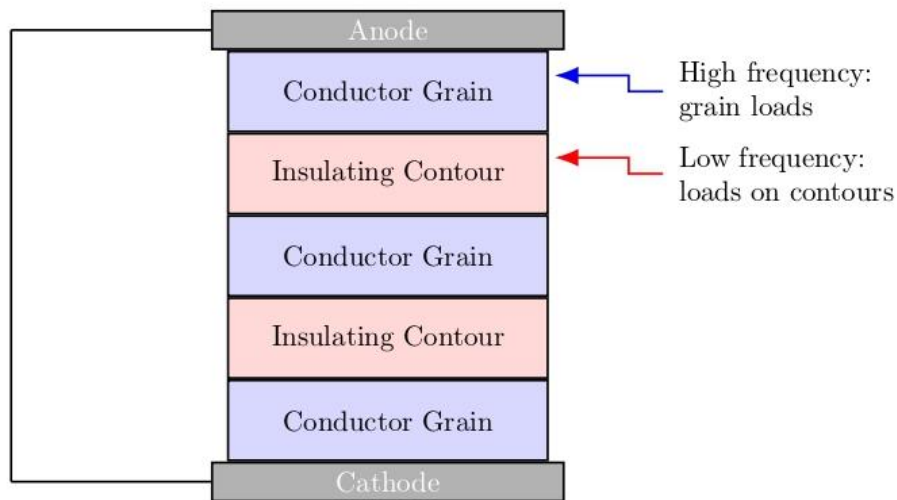
Source: Prepared by the author.

The equations that govern this model are [34]:

$$\varepsilon_{eff}^{*} = \varepsilon_{eff}^{'} - j\varepsilon_{eff}^{''} \tag{40}$$

$$\varepsilon_{eff}^{*} = \frac{d_g + d_{gb}}{\dfrac{d_g}{\varepsilon_g^{*}} + \dfrac{d_{gb}}{\varepsilon_{gb}^{*}}} \tag{41}$$

Where: ε_{eff}^{*} it is the effective complex permittivity; d_g, d_{gb} they are the average thicknesses of the grains and grain boundaries; ε_g^{*} , ε_{gb}^{*} they are the complex permittivities of the grains and grain boundaries (34).

Figure 14 – Maxwell-Wagner-Sillars model plot.
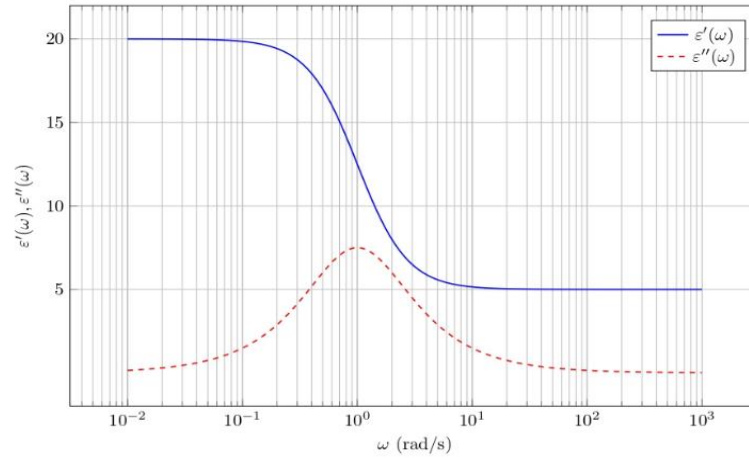
Source: Prepared by the author.

3.6 Nyquist diagram

According to the literature, the Nyquist diagram is used to analyze the dielectric parameters of polycrystalline materials, as it allows for an understanding of how the grains and grain boundaries behave, also correlating the relaxation processes that occur (35). Mathematically, the Nyquist diagram is a plot of the imaginary impedance versus the real impedance, that is, Z" versus Z'.

Consequently, for a more accurate analysis of this electromagnetic phenomenon, it is essential to model the Nyquist diagram using equivalent circuits. In this context, the use of constant phase elements (CPE) is important, as electrode roughness or even diffusion may occur, thus altering the nature of this element toward a more capacitive, resistive, or inductive behavior (35).

Equation 42 shows how to calculate the impedance of a resistor in series with a CPE (28):

$$Z_{CPE}(\omega) = q^{-1}(i\omega)^{-n} \tag{42}$$

Where q is a fitted numerical parameter and n is an exponential parameter that, depending on its value, will determine the nature of the CPE. Thus, when $n = 1$, the behavior is capacitive; when $n = 0$, it is resistive; and when $n = -1$, it is inductive (28, 35).

Generally, materials exhibit three arcs in the Nyquist diagram, derived from the effects of the grain, grain boundary, and electrode, but in many cases, these three arcs result in only one (35). The most appropriate equivalent circuit for representing these three arcs is typically composed of three resistors, each in parallel with a CPE, with these sets connected in series, as depicted in Figure 15 (28, 35). Mathematically, the total impedance is calculated as:

$$Z_{total}(\omega) = \sum_{k=1}^{3} \frac{R_k}{1 + R_k q_k (i\omega)^{nk}}$$

(43)

Figure 15 – Nyquist diagram.
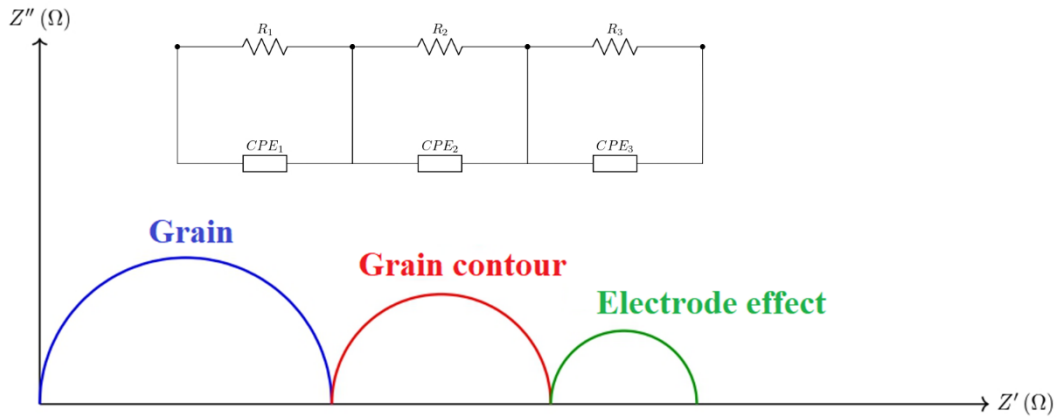
Source: Prepared by the author.

3.7 Analysis of Dielectric Properties in Microwaves (WM)

Dielectric materials also exhibit interesting electrical properties when subjected to electromagnetic fields with frequencies in the microwave range (GHz) (36). Among the many applications, the most well-known is the dielectric resonator antenna (DRA). The physical explanation of how resonators function as antennas begins when they are placed in an electromagnetic field, which excites them to oscillate in their natural modes, similar to a resonant cavity (37). This generates oscillating electromagnetic fields which, in turn, create displacement currents and consequently result in the emission of electromagnetic radiation (36, 37). Figure 16 illustrates an array of DRAs excited by a probe that emits electromagnetic radiation. The resonance frequency depends on the geometry of the DRAs. As a result, DRAs

with cylindrical geometry exhibit wave functions in the Transverse Electric (TE) mode along the z-axis and the Transverse Magnetic ™ mode along the z-axis. Mathematically, we have [38]:

$$\psi_{TE_{npm}} = J_n\left(\frac{X_{np}}{a}\rho\right)\begin{Bmatrix}\sin n\emptyset\\\cos n\emptyset\end{Bmatrix}\sin\left[\frac{(2m+1)\pi z}{2d}\right] \tag{44}$$

$$\psi_{ME_{npm}} = J_n\left(\frac{X'_{np}}{a}\rho\right)\begin{Bmatrix}\sin n\emptyset\\\cos n\emptyset\end{Bmatrix}\sin\left[\frac{(2m+1)\pi z}{2d}\right] \tag{45}$$

Where J_n is the Bessel function of the first kind, a is the radius of the cylinder, and d is the height of the cylinder.

Figure 16 – DRA (Dielectric Resonator Antenna) array.
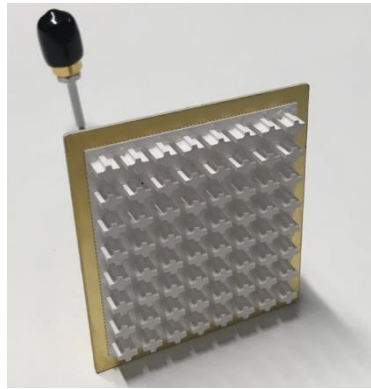
Source: Public domain.

The antenna parameters of DRAs are essential for understanding and evaluating how this technology can be useful in society. One such parameter is the radiation intensity $U(\theta, \phi)$, which is a mathematical function that indicates the spatial distribution of the radiated power (38). Equation 46 clearly shows the definition of radiation intensity (38).

$$U(\theta, \phi) = r^2 \cdot S_{rad}(r, \theta, \phi) \tag{46}$$

Where: S_{rad} (r, θ, ϕ) is the radiated power density (W/m²) in the direction of (θ, ϕ) and r is the distance from the antenna. The total power is calculated as the integral of $U(\theta, \phi)$ over all solid angles, and the radiation pattern, as (38):

$$P_{rad} = \int_0^{2\pi} \int_0^{\pi} U(\theta, \phi)\, sin\theta d\theta d\phi \tag{47}$$

According to the literature, the directivity $D(\theta, \phi)$ is a function that measures the amount of electromagnetic radiation an antenna emits in certain directions in space (38). Its formal definition is given by equation (48), and its maximum value by equation 49 (38):

$$D(\theta, \phi) = \frac{U(\theta, \phi)}{U_{iso}} = \frac{4\pi U}{P_{rad}} \tag{48}$$

$$D_{max}(\theta, \phi) = \frac{U_{max}}{U_0} = \frac{4\pi U_{max}}{P_{rad}} \tag{49}$$

The gain $G(\theta, \phi)$ of an antenna is defined as a function that relates the radiation intensity to the input power, as indicated by equation (50) (38). Furthermore, the gain can also be expressed as a function of directivity and electromagnetic radiation efficiency (η) through equation 51 (38):

$$G(\theta, \phi) = \frac{4\pi U}{P_{ent}} \tag{50}$$

$$G(\theta, \phi) = \eta \cdot D(\theta, \phi) \tag{51}$$

For a better understanding of the concept of antenna gain, Figure 17 shows the radiation pattern of an isotropic antenna versus a directional radiation pattern in a specific direction.

Figure 17 – Isotropic vs. directional antenna radiation patterns.
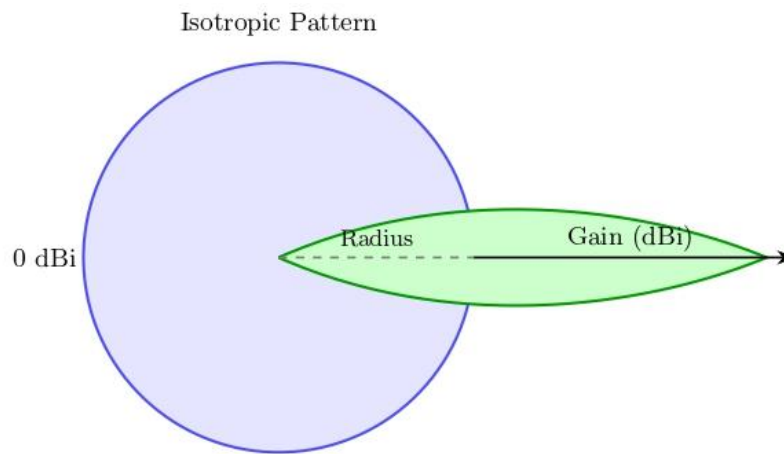
Source: Prepared by the author.

3.8 Monopole Measurement

According to the literature, the monopole technique with the aid of a network analyzer is essential for analyzing the use of resonators as antennas (39). Basically, this technique consists of a probe, a ground plane, and the network analyzer. With this in mind, one of the prerequisites for indicating that a resonator can function as an antenna is when the monopole measurements show a reflection coefficient (S_{11}) of at least less than -10 dB (39). Mathematically, S_{11} can be calculated as (39):

$$S_{11} = \frac{Z_L - Z_0}{Z_L + Z_0} \tag{52}$$

Where Z_L is the load impedance and Z_0 is the characteristic impedance of the transmission line, which is typically 50 Ω.

Air gaps can originate from manufacturing defects in DRAs. These tiny spaces, usually on the order of micrometers, can alter the S_{11} response of antenna resonators, affecting directivity, gain, and electromagnetic efficiency (40, 41). Figure 18 shows the monopole measurement technique.

Figure 18 – Monopole measurement setup illustration.
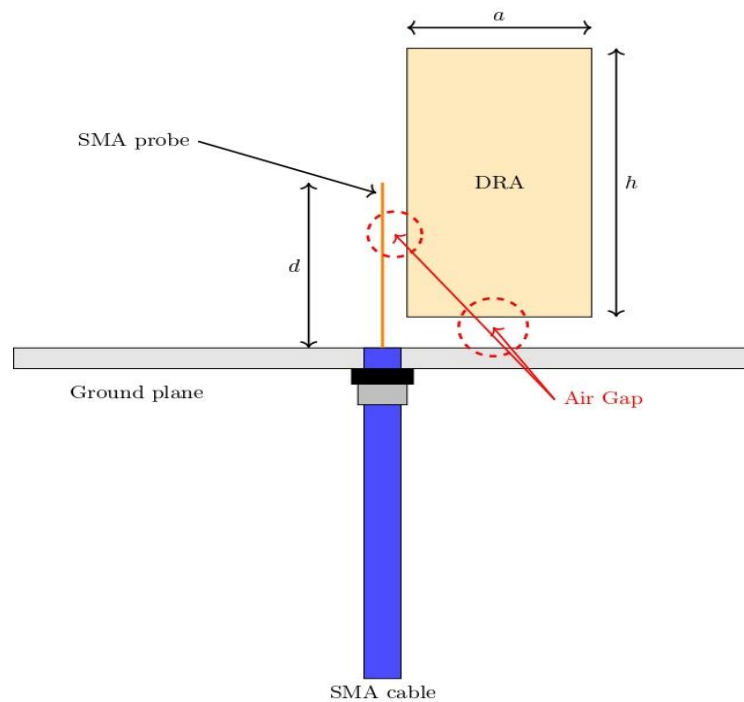
Source: Prepared by the author.

3.9 Hakki-Coleman Method

The Hakki-Coleman method is a widely used technique for extracting the loss tangent (tan δ), permittivity (ε′), and quality factor (Q) of ceramic resonators at microwave (MW) frequencies (42). These parameters are crucial for use in simulations and other experimental tests involving DRAs. For this, the dielectric geometry must be cylindrical, with a diameter-to-height ratio of 2:1, and it must be excited in the TE_{011} mode (42). Thus, using equations 53, 54, and 55, these parameters can be obtained (42):

$$\varepsilon' = \frac{1 - \left(\frac{D}{\lambda_0}\right)^2}{1 - \left(\frac{D}{\lambda_0}\right)^2 \cdot \left(\frac{c}{\pi D f_{011}}\right)^2} \tag{53}$$

$$Q = \left(\frac{1}{Q_d} + \frac{1}{Q_c}\right)^{-1} \tag{54}$$

$$Q_d = \frac{1}{\tan \delta} \tag{55}$$

Where λ_0 is the wavelength in vacuum, c is the speed of light, f_{011} is the resonance frequency of the TE_{011} , D is the diameter of the dielectric resonator, Q_d is the quality factor due to dielectric losses, and Q_c is the quality factor due to conductor losses (42). Figure 19 shows an illustration of the Hakki-Coleman Method.

Figure 19 – Illustration of the Hakki-Coleman Method.
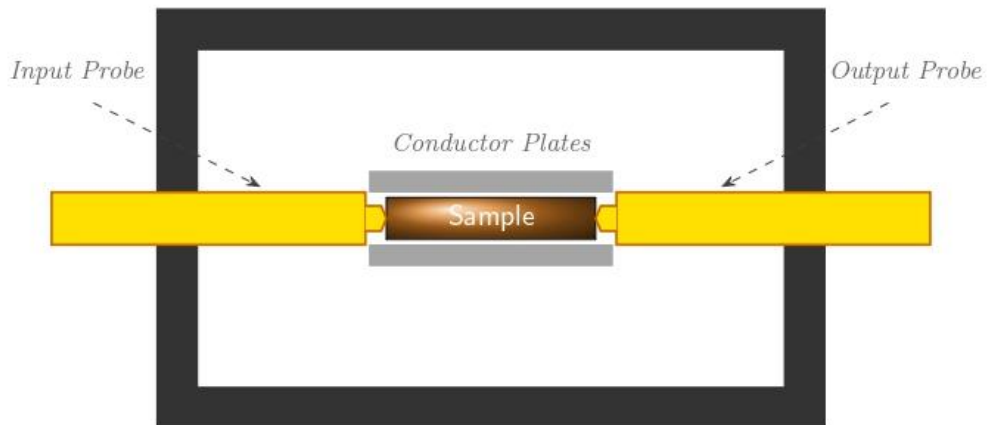
Source: Prepared by the author.

3.10 Silva-Fernandes-Sombra Method

The Silva-Fernandes-Sombra method is an alternative approach for calculating the Temperature Coefficient of Resonant Frequency (τ_f), particularly for materials with high dielectric losses (tanδ> 10^{-2}) (43). This method consists of a refractory ceramic, a ground plane, a feed system, probes coupled to a vector network analyzer, and a heating system, as shown in Figure 20 (43).

Thus, this method has a higher success rate than the traditional Courtney method. In summary, the Silva-Fernandes-Sombra method monitors the frequency of the DRA using the dominant hybrid mode HE$_{11}\delta$, which is less sensitive to dielectric losses $HE_{11\delta}$ the operating frequency is calculated using Equation 56 (43) :

$$f_{HE_{11\delta}} = \frac{6.324c}{2\pi a\sqrt{\varepsilon + 2}}\left[0.27 + 0.36\left(\frac{a}{2h}\right) + 0.02\left(\frac{a}{2h}\right)^2\right] \tag{56}$$

However, the equation that determines τ_f is Equation 57. Dielectrics with values between ±10 ppm/°C exhibit good thermal stability, which enables the application of these materials as DRAs (44). Mathematically, we have (44):

$$\tau_f = \frac{1}{f_1} \cdot \frac{\Delta f}{\Delta T} \cdot 10^6 [ppm/°C]. \tag{57}$$

Figure 20 – Illustration of the Silva-Fernandes-Sombra Method.
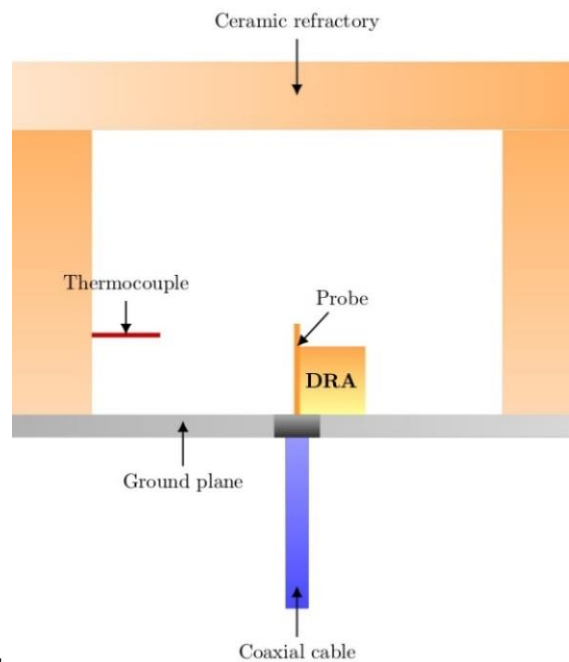
Source: Prepared by the author.

4 EXPERIMENTAL PROCEDURES

This chapter aims to describe the equipment used, the methodology employed in the radiofrequency and microwave characterizations, the structural and morphological analyses of the samples, as well as the manufacturing process of the test specimens. All these steps are illustrated in the flowchart presented in Figure 21, which shows the logical sequence of the processes carried out.

Figure 21 – Flowchart of the procedures.
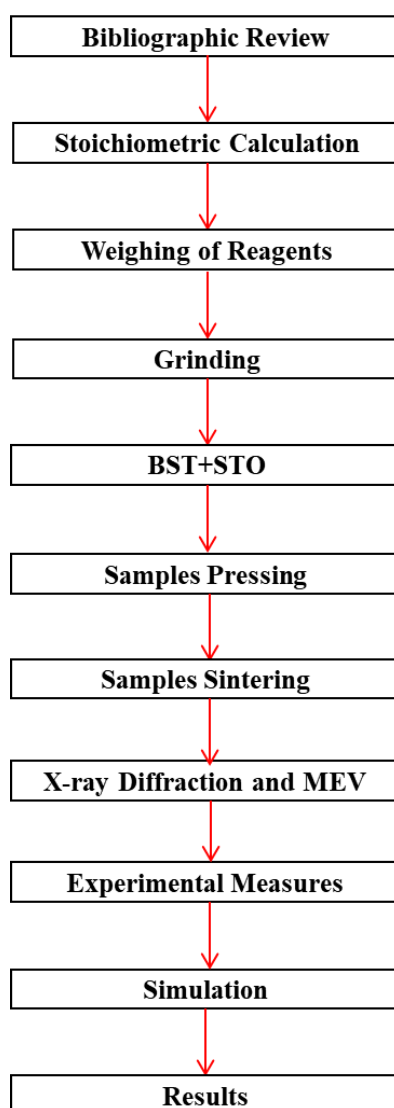
Source: Prepared by the author.

4.1 Preparation of the Ba₂TiSi₂O₈ e SrTiO₃ Matrices

The Ba₂TiSi₂O₈ matrix was fabricated using the solid-state reaction method, following the appropriate stoichiometry from the literature. However, the SrTiO₃ matrix was used in its commercial form (Aldrich, 99.9%). The synthesis of the Ba₂TiSi₂O₈ ceramic matrix was carried out via solid-state reaction, as described in Equation (58). High-purity reagents BaCO₃ (99.99%, Vetec), TiO₂ (99.8%, Aldrich), and SiO₂ (99.9%, Aldrich) were used and weighed according to the stoichiometric ratio given by Equação 58 (45–47).

$$2BaCO_3 + 2SiO_2 + TiO_2 \xrightarrow{\Delta} Ba_2TiSi_2O_8 + 2CO_2 \tag{58}$$

The reagents were milled in a planetary ball mill operating at 360 rpm for 4 hours, and then the homogeneous mixture was calcined at 1100 °C for 6 hours, as shown in Figure 22.

Figure 22 – Planetary ball mill.

Source: Public domain.

4.2 X-ray Diffraction

For the XRD analysis, a Rigaku D/max-B XPert Pro MPD-Panalytical diffractometer was used, with Cu-Kα radiation (1.5406 Å), a scan range of 10° to 80° (2θ), a step size of 0.013°, and operating at 40 kV and 40 mA. This equipment is from the Federal University of Ceará, specifically from the X-ray Laboratory in the Department of Physics, as shown in Figure 23. The phases were identified by correlating the experimental results with data from the Inorganic Crystal Structure Database (ICSD) (46, 47).

Figure 23 – Rigaku D Diffractometer.
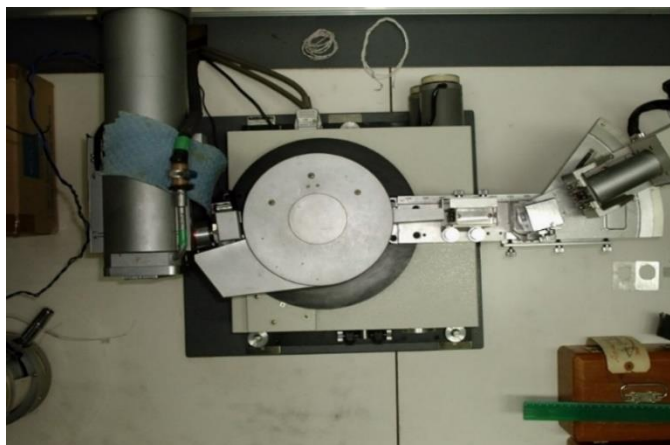
Source: Public domain.

4.3 Scanning Electron Microscopy (SEM)

SEM analysis was performed using a Quanta 450 FEG scanning electron microscope with a magnification factor of 2500, as shown in Figure 24. This equipment is owned by the Federal University of Ceará, specifically by the Central Analytical Facility.

Figure 24 – SEM Equipment.

Source: Public domain.

4.4 Fabrication of Ceramic Composites

Next, 5–20% of STO was added to the BTS ceramic matrix. The composites were named BTS, BTS-5STO, BTS-10STO, BTS-15STO, and BTS-20STO. The composites were compacted using uniaxial pressure of 15.20 MPa into cylindrical disc shapes. The samples

were then sintered at 1200 °C for 4 hours. Afterwards, the cylindrical discs were coated with silver paint on both sides in order to fabricate a capacitor. The discs were then heated in a resistive furnace at 500 °C for 2 hours. Figure 25 shows the fabricated ceramic cylinders.

Figure 25 – Ceramic cylinders of the produced composites.

Source: Prepared by the author.

4.5 Pycnometry

To calculate the relative density (D_r) of the samples, it is first necessary to determine the experimental density of the specimens (ρ_{body}). For this purpose, the pycnometry method was used. This method is defined as a procedure to experimentally obtain the density of a body using the principle of buoyancy, through a 25 mL container filled with pure (distilled) water, as shown in Figure 25 (48).

$$\rho_{body} = \frac{m_{body} \cdot \rho_{water}}{m_{body} + m_{pic+water} - m_{pic+water+body}} \qquad (59)$$

Where m_{body} is the mass of the specimen, ρ_{water} is the density of water $m_{pic+water}$ is the mass of the pycnometer filled with water, and $m_{pic+water+body}$ is the mass of the pycnometer filled with water and the specimen. Additionally, the theoretical density (D) was calculated as a weighted average of the component densities using Equation 60 (48):

$$D = \frac{100}{\frac{\%mass\ (\alpha)}{d_{monocrystal}\ (\alpha)} + \frac{\%mass\ (\beta)}{d_{monocrystal}\ (\beta)}} \tag{60}$$

Where $d_{monocrystal}$ is the density of the monocrystal of the phase present in the composite, and, *%mass* is the mass fraction of the phase present in the composite. Once the theoretical density and experimental density are obtained, the relative density can now be calculated as:

$$D_r = \frac{\rho_{body}}{D} \cdot 100\% \tag{61}$$

Figure 26 – Pycnometer.

Source: Public domain.

4.6 Radio-Frequency Measurements

The measurements of the dielectric resonators in radiofrequency began initially at room temperature (30ºC), increasing up to 380 ºC. The equipment used was a Solartron® impedance analyzer model SI1260, operating in the range of 100 Hz to 1 MHz, with the Impedbeta data acquisition software, also from Solartron®.

This equipment is owned by the Federal University of Ceará, as shown in Figure 27. By inputting the sample dimensions into the software, dielectric parameters such as permittivity, conductivity, activation energy, temperature coefficient of capacitance (TCC), and Nyquist plot are extracted.

Figure 27 – Impedance Analyzer.

Source: Prepared by the author.

4.7 Microwave Measurements

For the microwave measurements, the three previously mentioned methods were used: Monopole Measurements, Hakki-Coleman Technique, and Silva-Fernandes-Sombra Method. The monopole measurements were first performed, where the DRA is placed on the probe to measure the S_{11} and Impedances (Z', Z''). These parameters are crucial for the simulations that will calculate antenna parameters such as directivity, gain, and electromagnetic efficiency. Figure 28 shows the monopole measurement equipment, which is owned by the Federal University of Ceará. It consists of a ground plane, probes, connectors, and a HP8716ET network analyzer.

Figure 28 – Monopole Measurement Equipment.

Source: Prepared by the author.

Secondly, the Hakki-Coleman Technique was used, which consists of two conductive (metal) plates where the probe will excite the ceramic sample. This measurement is essential to determine the loss tangent, quality factor, and permittivity of the sample, as explained earlier. Figure 29 shows the equipment used from the Federal University of Ceará.

Figure 29 – Hakki-Coleman Technique Equipment.

Source: Public domain.

Finally, the Silva-Fernandes-Sombra Method was used to calculate thermal stability, that is, to measure the Temperature Coefficient of Resonance Frequency (τ_f). This method is exclusive to the researchers of LOCEM (Telecommunications and Materials Science and Engineering Laboratory) at UFC. Figure 30 illustrates the equipment.

Figure 30 – Silva-Fernandes-Sombra Method Equipment.
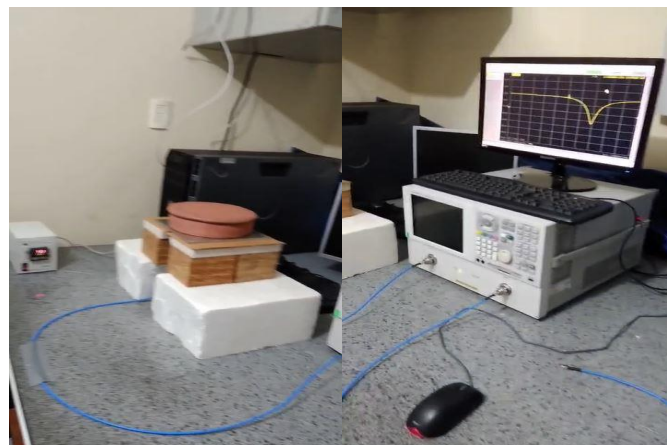
Source: Prepared by the author.

4.8 Numerical Simulation

The numerical simulations were performed using the Ansys HFSS software. This software is a widely used simulation program in the field of telecommunications engineering to calculate directivity, gain, and electromagnetic efficiency of various antennas (12, 13, 55). In this context, the model used for the simulation was a simplification of the Monopole Measurements, as shown in Figure 31.

It is important to note that the input data for this model are the sample geometries, such as height and radius. In addition to these variables, the input data also includes: S_{11}, impedances (Z', Z''), permittivity (ε'), and loss tangent (tan δ), which are obtained through the Hakki-Coleman Method and Monopole Measurements (12). The final result of the simulation, as shown in Figure 32, indicates the amount of radiation, directivity, gain, electromagnetic efficiency, and radiation pattern of the DRA (13).

Figure 31 – Model used in the simulation.
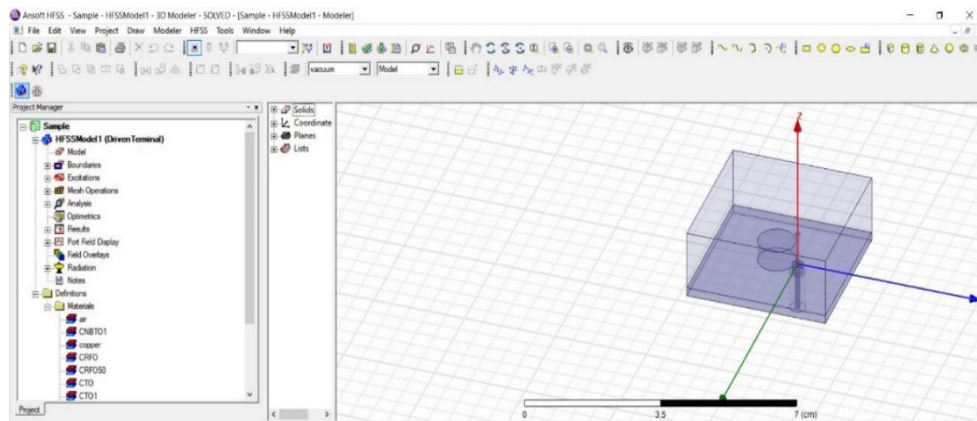
Source: Prepared by the author.

Figure 32 – Numerical simulation output.
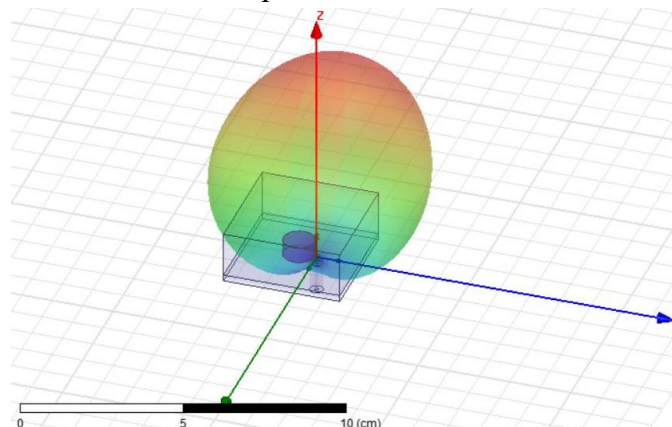
Source: Prepared by the author.

5 RESULTS AND DISCUSSIONS

5.1 X-Ray Diffraction

The Rietveld refinement of the pure BTS sample is shown in Figure 30 (a), and no spurious phases were observed; the observed peaks are compatible with the crystallographic record ICSD 201845. The statistical parameters obtained from the Rietveld refinement for the BTS matrix were $\chi 2 = 1.44$, $R_{Bragg} = 5.9\%$ e $R_{wp} = 17.86\%$, confirming an adequate refinement consistent with the literature (21, 22).

From Figure 33 (b), a significant change in the standard deviation of the fractions is observed starting from BTS – 5STO. This indicates that, in addition to the BTS and STO phases, a spurious crystalline phase called $Ba_{0.3}Sr_{0.7}TiO_3$ (BSTO) emerges. This phase is present in all the composites, confirming a chemical reaction between BTS and STO. The densification of the samples was calculated by the ratio between the monocrystal density obtained through the Rietveld Refinement and the density of the samples obtained through pycnometry (46). All samples exhibited a high degree of densification, with values exceeding 90%. The high densification of electro-ceramics contributes to the increase of dielectric parameters, such as relative permittivity (47).

Table 1 Refinement parameters from the Rietveld method and the mass proportion determined for the analyzed samples.

Samples	Statistical Parameters			Mass fraction (%)			Density (%)
	R_{WP} (%)	χ^2	R_B(%)	$Ba_2TiSi_2O_8$	$(Ba_{0.3}Sr_{0.7})TiO_3$	$SrTiO_3$	
BTS	17.86	1.44	5.9	100	-	-	92.15
BTS – 5STO	15.67	1.23	5.2	92.7	6.2	1.1	90.38
BTS – 10STO	15.94	1.31	6.1	86.5	9.6	3.9	91.19
BTS – 15STO	15.60	1.25	6.0	80.0	10.5	9.5	91.08
BTS – 20STO	16.23	1.40	6.2	75.2	11.6	13.2	91.62

Source: Prepared by the author.

Figure 33 (a-e)- XRD patterns and Rietveld refinement.
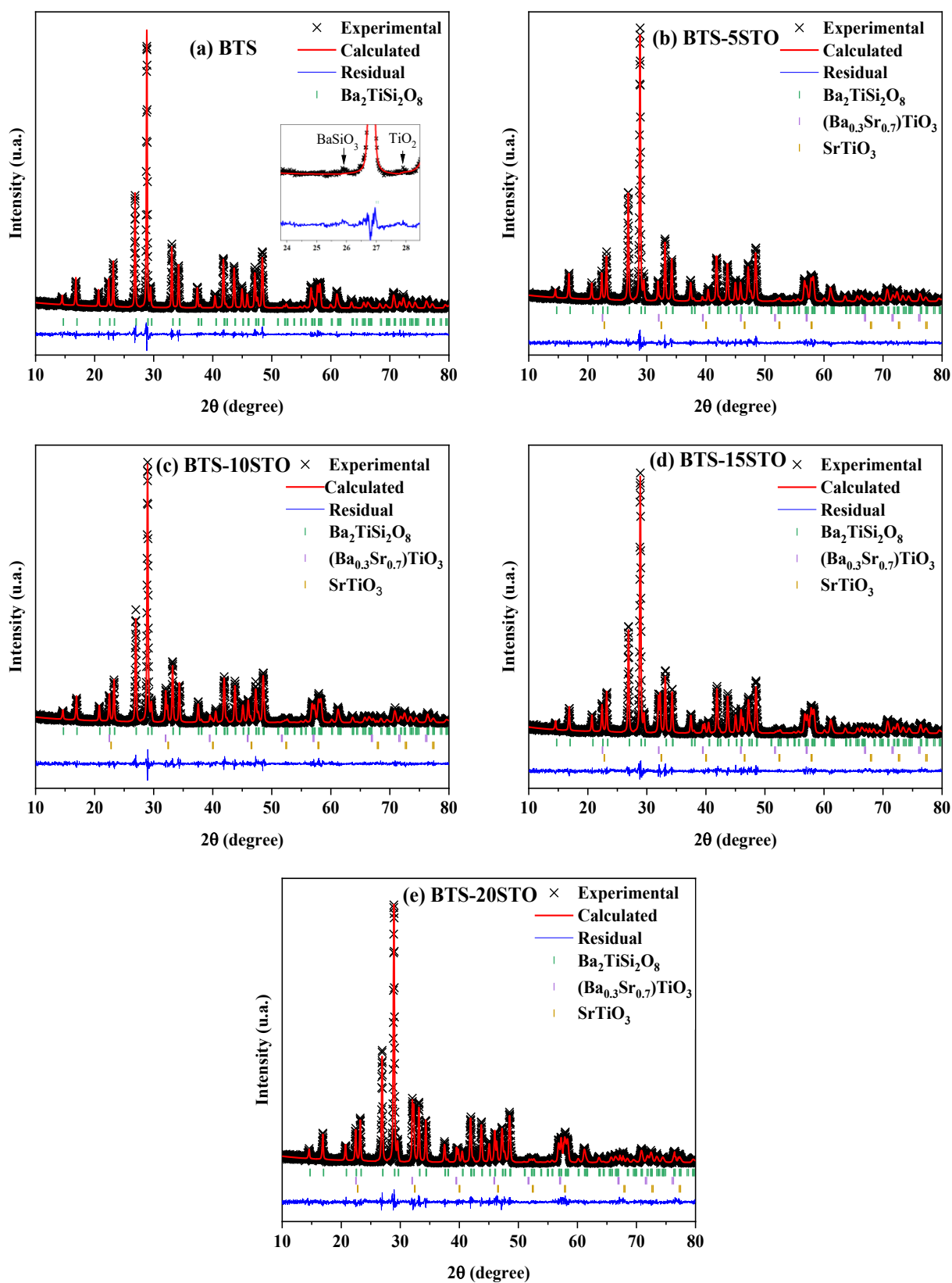
Source: Prepared by the author.

5.2 Scanning Electron Microscopy (SEM)

Figure 34 presents the micrographs of the BTS – STO ceramic composites obtained by Scanning Electron Microscopy (SEM) with a magnification of 2500x. The images show a microstructure with distinct shapes and a heterogeneous distribution composed of grains of various sizes.

The grain morphology changed, which may be related to modifications in the crystalline phases that were previously reported in the previous section. This morphological change demonstrates how the different chemical compositions of the composites affect the development and coalescence of the grains (48, 49).

Figure 34- Surface micrographs (2500× magnification).
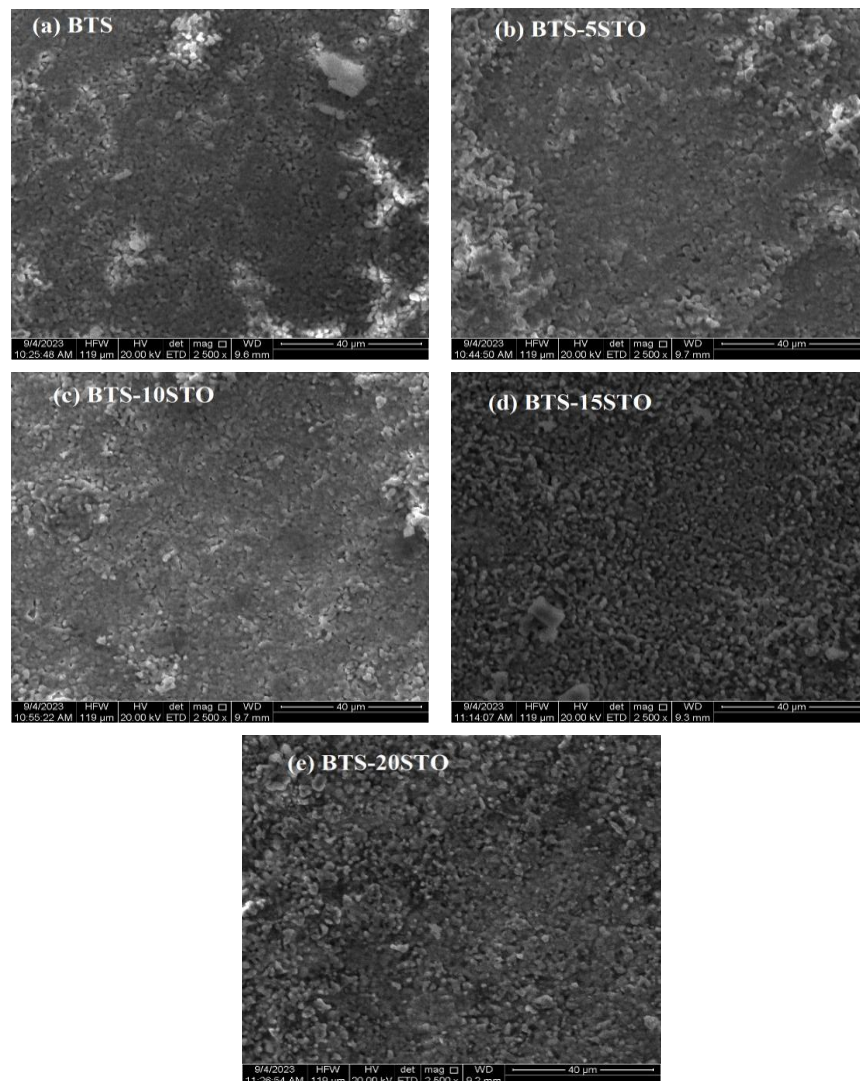
Source: Prepared by the author.

5.3 Dielectric Analysis in Radiofrequency (RF)

Figure 35 shows the spectra of relative permittivity (ε'_r) from 100 Hz to 1 MHz for all samples at room temperature (25°C). It was observed that the addition of STO to the composites increased ε'_r at room temperature. This increase in ε'_r can be attributed to the appearance of the $(Ba_{0.3}Sr_{0.7})TiO_3$ phase, which, according to the literature, has a high permittivity ($\varepsilon'_r \sim 623$) (53), and the secondary phase of $SrTiO_3$, which has a significantly higher ε'_r compared to the BTS ceramic matrix ($\varepsilon'_r \sim 18.90$) (12-14, 54-56).

It can be observed that as the frequency increases, the values of ε'_r decrease. This phenomenon is related to the polarization process to which the material is subjected in the frequency range analyzed, which, in this case, is dipole polarization. As the frequency increases, the total polarization of the system decreases because the intrinsic dipoles of the samples cannot keep up with the applied electric field; ε'_r follows the polarization trend and decreases. This phenomenon is explained by the theoretical model of two layers of Maxwell-Wagner-Sillars (MWS) (57-58).

According to this model, the structure of the materials consists of layers of conductive grains intercalated by insulating grain boundaries (56-59). Thus, at low frequencies, charge carriers accumulate at the boundaries of the resistive grains, while at high frequencies, the carriers are present in the conductive grains and can move with greater freedom (56-59).

Figure 35 - Room temperature permittivity vs. frequency.
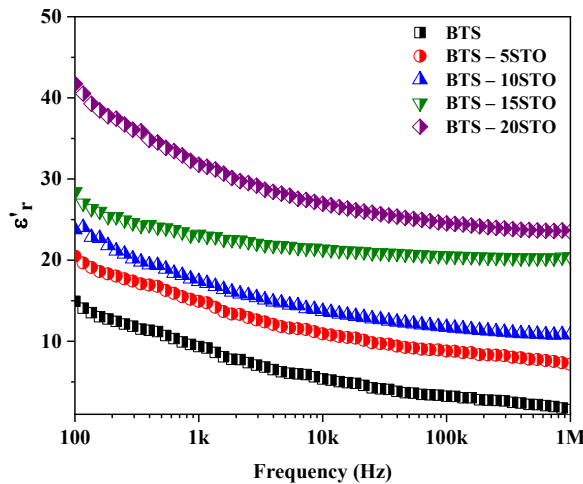
Source: Prepared by the author.

The spectra of ε'_r with temperature variation (300°C – 380°C) are shown in Figure 36. It is observed that ε'_r increases with the rise in temperature; however, the samples still exhibit behavior consistent with the Maxwell-Wagner-Sillars model.

Figure 36 - Permittivity of samples with frequency and temperature variation.
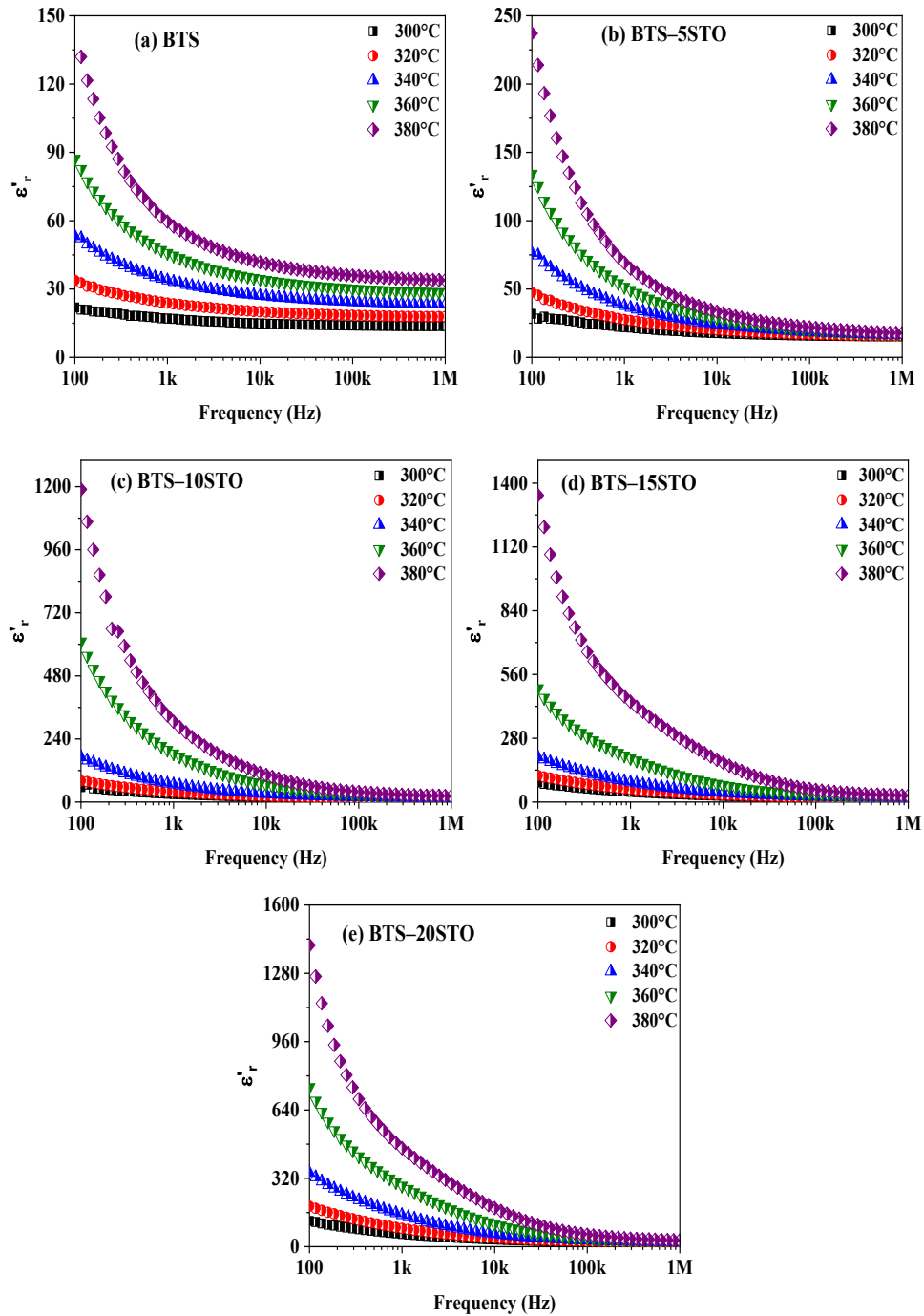
Source: Prepared by the author.

Figure 37 shows the behavior of conductivity versus frequency for the temperature range 300°C – 380°C, with a numerical fit performed using Jonscher's equation (universal power law) in equation 62 (59-64).

$$\sigma' = \sigma_{DC} + A(\omega)^n .$$ (62)

σ': total conductivity; σ_{DC}: Direct current conductivity A, n: thermally activated quantities; ω: frequency

The importance of this analysis lies in the fact that the numerical values of A e n and n in Jonscher's equation have a physical meaning that appropriately explains the conduction process (59-64). The parameter A provides the polarization intensity (61, 62), and the parameter n determines the type of charge carrier hopping (61, 62). Thus, n can be divided into two cases: when $n < 1$, the charge carriers perform translational hopping (61, 62). However, for $n > 1$, the charge carriers perform localized hopping in their vicinity (61, 62). It is noted that the charge carriers in the samples only performed translational hopping ($n < 1$).

Table 2 Adjustment of AC conductivity parameters using Jonscher's power law.

Temperature (°C)	σ_{DC} (Ω/m)	A	n	R^2
BTS				
300	1.41×10^{-6}	1.20×10^{-9}	0.761	0.999
320	8.64×10^{-6}	1.88×10^{-8}	0.774	0.993
340	7.53×10^{-5}	1.64×10^{-9}	0.843	0.994
360	5.10×10^{-4}	4.54×10^{-10}	0.879	0.998
380	7.38×10^{-4}	5.95×10^{-10}	0.904	0.999

Temperature (°C)	σ'_{DC} (Ω/m)	A	n	R^2
BTS5				
300	7.35×10^{-7}	2.94×10^{-9}	0.917	0.991
320	5.03×10^{-6}	3.13×10^{-8}	0.869	0.993
340	2.17×10^{-5}	1.44×10^{-7}	0.818	0.992
360	1.25×10^{-4}	5.20×10^{-6}	0.785	0.994
380	3.46×10^{-4}	2.53×10^{-6}	0.772	0.997

Temperature (°C)	σ'_{DC} (Ω/m)	A	n	R^2
BTS10				
300	5.99×10^{-7}	1.49×10^{-9}	0.782	0.995
320	2.68×10^{-6}	4.08×10^{-9}	0.753	0.998
340	1.42×10^{-5}	1.21×10^{-8}	0.712	0.994
360	1.65×10^{-4}	2.81×10^{-8}	0.687	0.991
380	6.72×10^{-4}	3.46×10^{-8}	0.632	0.998

Temperature (°C)	σ'_{DC} (Ω/m)	A	n	R^2
BTS15				
300	3.18×10^{-6}	9.18×10^{-9}	0.651	0.990
320	2.95×10^{-6}	3.21×10^{-8}	0.638	0.999
340	7.68×10^{-6}	5.10×10^{-8}	0.591	0.996
360	6.50×10^{-5}	3.71×10^{-7}	0.569	0.997
380	4.45×10^{-4}	2.99×10^{-6}	0.522	0.993

Temperature (°C)	σ'_{DC} (Ω/m)	A	n	R^2
BTS20				
300	1.98×10^{-6}	1.84×10^{-8}	0.536	0.999
320	3.49×10^{-6}	1.55×10^{-7}	0.520	0.995
340	2.12×10^{-5}	1.65×10^{-7}	0.507	0.996
360	1.43×10^{-4}	6.11×10^{-7}	0.475	0.992
380	2.57×10^{-4}	3.81×10^{-6}	0.406	0.991

Source: Prepared by the author.

.

Figure 37: Conductivity spectra with temperature variation.
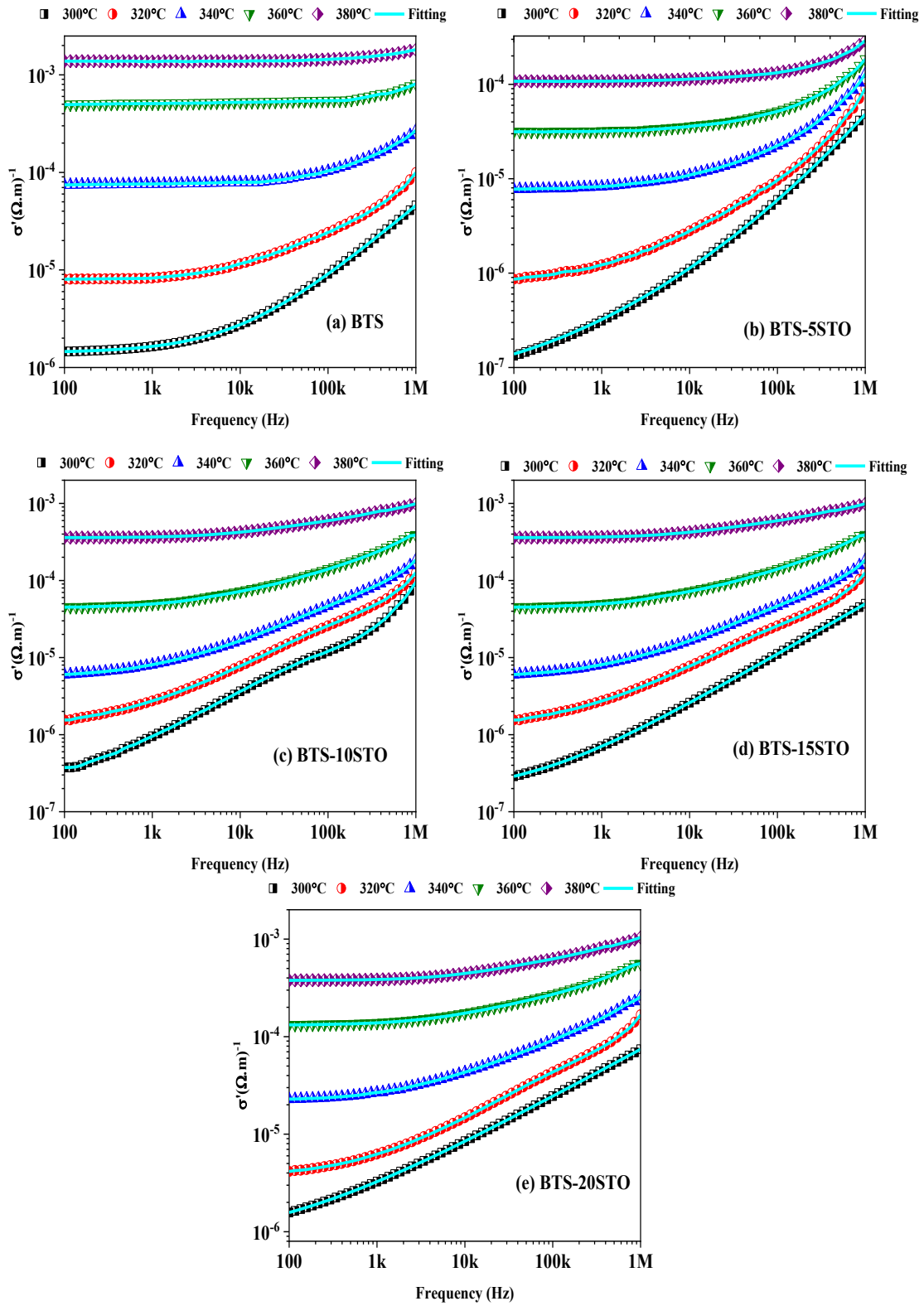
Source: Prepared by the author.

Figure 38 shows the spectra of imaginary impedance (Z″) at different temperatures (300°C – 380°C). It was observed that the values of Z″ increase around 10 Hz – 1 KHz for BTS, while the other composites (BTS – 5STO, BTS – 10STO, BTS – 15STO, BTS – 20STO) show an increase in the range of 10 Hz – 100 Hz. Furthermore, the peaks of imaginary impedance gradually shifted to higher frequencies, showing broadening and asymmetry as the temperature increases, indicating a non-Debye behavior and highlighting a temperature-dependent phenomenon (59-64).

Figure 38 (a-e) Z''Spectrum as a function of temperature for all samples.
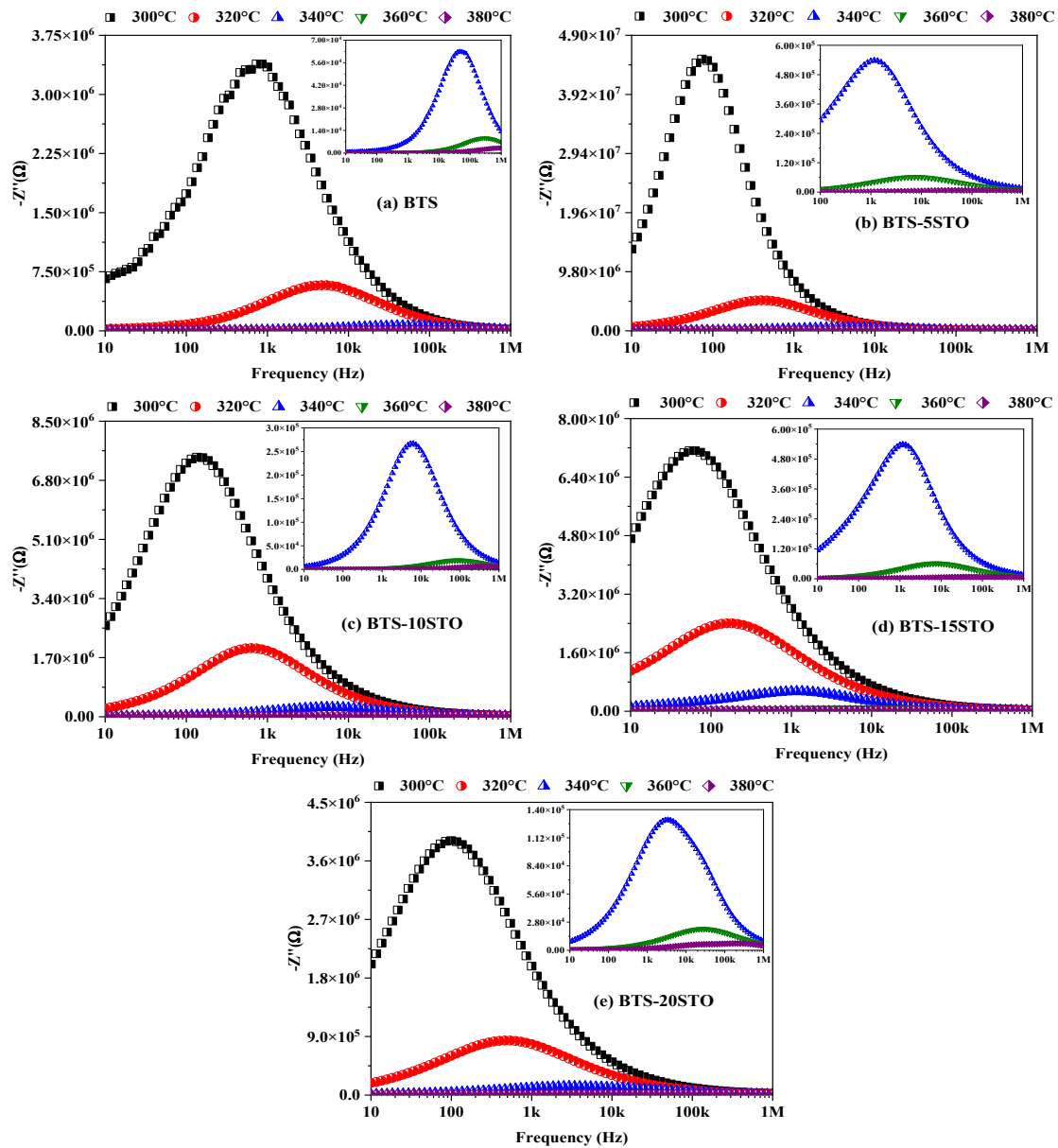
Source: Prepared by the author.

5.4 Nyquist Diagram

Figure 36 shows the Nyquist diagrams ($-Z'' \times Z'$) of the samples. The behavior of these diagrams consists of semicircles, which are consistent with the non-Debye behavior of dielectric materials (62–64). As shown in Figure 39, an equivalent circuit composed of two parallel associations of a resistor (R) and a constant phase element (CPE) was used to determine the dielectric contributions of the grain and grain boundary of the samples (14, 54, 55, 60–64). Through this model, it is possible to extract parameters from the grains and grain boundaries, which typically exhibit different electrical and microstructural characteristics (60–64). The total impedance of the circuit can be calculated using Equation 63.

$$Z_T(\omega) = Z_g(\omega) + Z_{gb}(\omega) \tag{63}$$

$$Z_g(\omega) = \frac{R_1 + qR_1^2\omega^n\cos\left(\frac{n\pi}{2}\right)}{R_1^2q^2\omega^{2n} + 2R_1q\omega^n\cos\left(\frac{n\pi}{2}\right) + 1} - jq\frac{R_1^2\omega^n sen\left(\frac{n\pi}{2}\right)}{R_1^2q^2\omega^{2n} + 2R_1q\omega^n\cos\left(\frac{n\pi}{2}\right) + 1} \tag{64}$$

$$Z_{bg}(\omega) = \frac{R_2 + qR_2^2\omega^n\cos\left(\frac{n\pi}{2}\right)}{R_1^2q^2\omega^{2n} + 2R_1q\omega^n\cos\left(\frac{n\pi}{2}\right) + 1} - jq\frac{R_2^2\omega^n sen\left(\frac{n\pi}{2}\right)}{R_1^2q^2\omega^{2n} + 2R_1q\omega^n\cos\left(\frac{n\pi}{2}\right) + 1} \tag{65}$$

q: proportionality factor; $n = -1$; inductive behavior; $n = 0$; resistive behavior; $n = +1$; capacitive behavior.

The characteristics of the equivalent circuit for each sample are shown in **R_g** (grain resistance), **P_g** (grain capacitance), **n_g** (electrical nature exponent in the grain), **R_{gb}** (grain boundary resistance), **P_{gb}** (grain boundary capacitance), **n_{gb}** (electrical nature exponent of the grain boundary). The values of **n_g** and **n_{gb}** for all samples remained in the range of $0.8 \leq n < 1$ for both the grain and the grain boundary. Thus, the samples exhibit a strong capacitive character, indicating that electrode surface roughness or charge carrier accumulation are the likely causes of this capacitive tendency (60–64). These parameters were obtained through numerical simulations using the software Electrochemical Impedance Spectroscopy Spectrum Analyzer (EISSA®) (62).

Table 3 – Equivalent Circuit Parameters from 300°C to 380°C.

Temperature (ºC)	Grain			Grain boundary		
	R_g (Ω)	P_g (F)	n_g	R_{gb} (Ω)	P_{gb} (F)	n_{gb}
BTS						
300	9.31×10^6	1.35×10^{-10}	0.79	4.43×10^4	5.01×10^{-5}	0.80
320	7.30×10^6	8.08×10^{-10}	0.99	6.91×10^5	4.75×10^{-5}	0.98
340	1.96×10^5	1.66×10^{-10}	0.94	1.49×10^3	8.29×10^{-5}	0.98
360	9.14×10^5	5.02×10^{-10}	0.95	2.47×10^3	4.73×10^{-5}	0.91
380	1.96×10^5	9.87×10^{-10}	0.97	8.62×10^3	3.61×10^{-5}	0.97
BTS-5STO						
300	9.75×10^7	2.92×10^{-10}	0.91	2.92×10^5	2.85×10^{-5}	0.91
320	5.37×10^7	1.30×10^{-10}	0.93	4.18×10^5	1.30×10^{-5}	0.92
340	5.94×10^5	8.33×10^{-10}	0.95	8.43×10^3	8.83×10^{-5}	0.94
360	3.71×10^5	3.64×10^{-10}	0.97	3.53×10^3	1.62×10^{-5}	0.95
380	1.01×10^5	2.69×10^{-10}	0.98	1.01×10^3	1.23×10^{-5}	0.96
BTS-10STO						
300	5.95×10^7	2.96×10^{-10}	0.90	2.76×10^5	1.24×10^{-5}	0.89
320	2.28×10^7	3.46×10^{-10}	0.91	5.42×10^5	2.47×10^{-5}	0.90
340	8.12×10^5	6.37×10^{-10}	0.93	9.93×10^3	4.17×10^{-5}	0.91
360	5.92×10^5	9.88×10^{-10}	0.94	7.80×10^3	8.42×10^{-5}	0.93
380	1.16×10^5	4.31×10^{-10}	0.95	4.60×10^3	4.89×10^{-5}	0.94
BTS-15STO						
300	2.49×10^6	8.02×10^{-10}	0.89	1.68×10^5	5.02×10^{-5}	0.89
320	8.73×10^6	1.32×10^{-10}	0.90	9.97×10^5	2.78×10^{-5}	0.91
340	1.12×10^5	6.87×10^{-10}	0.91	9.73×10^3	6.87×10^{-5}	0.94
360	2.33×10^5	5.59×10^{-10}	0.92	7.54×10^3	5.02×10^{-5}	0.93
380	1.94×10^5	5.31×10^{-10}	0.93	2.80×10^3	1.43×10^{-5}	0.92
BTS-20STO						
300	1.35×10^6	1.09×10^{-10}	0.85	6.92×10^5	1.58×10^{-5}	0.86
320	2.98×10^6	1.76×10^{-10}	0.86	1.52×10^5	1.14×10^{-5}	0.87
340	5.56×10^6	1.87×10^{-10}	0.88	4.28×10^4	3.50×10^{-5}	0.90
360	9.99×10^6	1.97×10^{-10}	0.91	8.06×10^3	7.18×10^{-5}	0.92
380	1.25×10^6	3.15×10^{-10}	0.92	1.56×10^3	3.15×10^{-5}	0.93

Source: Prepared by the author.

Figure 39 Nyquist plot with an electrical equivalent circuit for all samples.
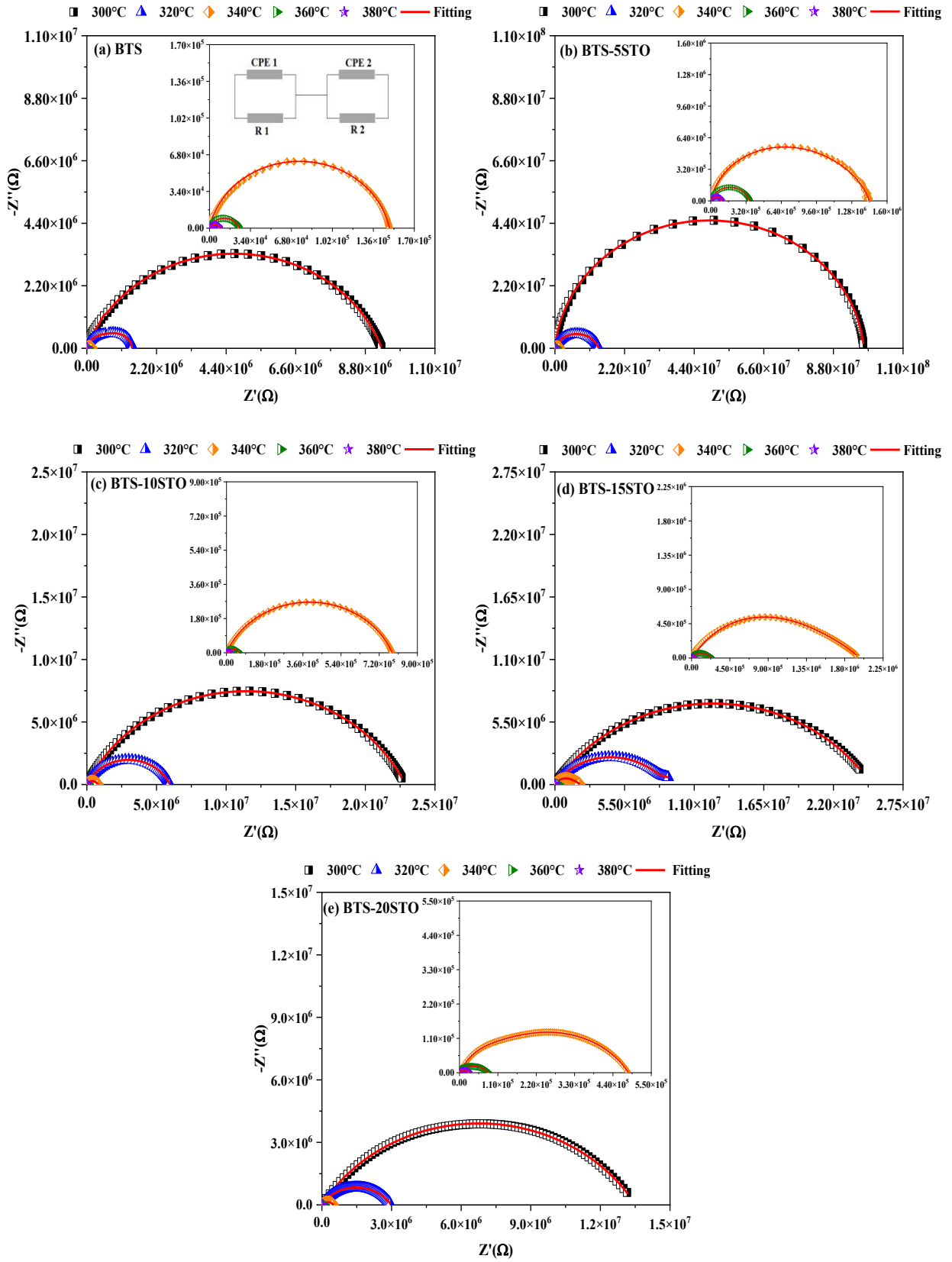
Activation energy (E_a) is a parameter associated with charge movement or dipole reorientation (14, 54, 55, 60-64). Consequently, the activation energy was calculated using the Arrhenius equation based on conductivity (σ') through Equation 66, and also derived from the peak frequency of imaginary impedance (f_{max}) using Equation 67 (14, 54, 55, 60-64).

$$E_a = -kT \cdot \ln\left(\frac{\sigma'}{\sigma_0}\right) \tag{66}$$

$$E_a = -kT \cdot \ln\left(\frac{f_{max}}{f_0}\right) \tag{67}$$

Where: σ_0, f_0: pre-exponential factors for conductivity and imaginary impedance frequency, respectively; f_{max}: peak frequency of Z"; E_a: activation energy; k: Boltzmann constant; T: absolute temperature in Kelvin.

As shown in Table 4 and Figure 40, the activation energy was observed to increase with higher $SrTiO_3$ content in the samples. This rise in activation energy is explained by the known activation energy values of $SrTiO_3$ (E_a = 1.31 eV) and the secondary phase $(Ba_{0.3}Sr_{0.7})TiO_3$ (E_a = 1.024 eV) (65, 66). Additionally, a strong numerical agreement was noted between the activation energies calculated from σ' and Z".

Table 4 Activation energy obtained by σ' and Z".

Samples	Ea / σ' (eV)	Ea /Z'' (eV)
BTS	1.76	1.73
BTS5	1.82	1.80
BTS10	1.84	1.82
BTS15	1.86	1.83
BTS20	1.93	1.92

Source: Prepared by the author.

Source: Prepared by the author.

The Thermal Capacitance Coefficient (TCC) indicates how the dielectric's capacitance changes in response to temperature variations at various operating frequencies (14, 54, 55, 60–64). The TCC was calculated using Equation 64 in the temperature range from 30 to 100 °C.

$$TCC = \frac{C_{100} - C_{30}}{C_{30}(100 - 30)} \tag{64}$$

Where C_{100} is the capacitance measured at $100\,°C$ and C_{30} is the capacitance measured at room temperature $30\,ºC$.

The TCC results shown in Table 5 were obtained in the frequency range of 100 Hz to 1 MHz. The BTS–10STO and BTS–15STO samples exhibited the lowest TCC values among the analyzed samples, falling within the range of ±1500 ppm/°C. Materials within this TCC range have high potential for application as Class 1 capacitors (61).

Table 5 TCC values for all samples.

Source: Prepared by the author.

5.5 Dielectric Analysis in the Microwave (MW) Range

Initially, a 3% concentration (BTS-3STO) was added, as this sample, as shown

Samples	TCC (ppm°C^{-1})/1000				
	Frequency				
	100 Hz	1 KHz	10 KHz	100 KHz	1 MHz
BTS	-6.56	-6.31	-5.92	-5.24	-4.59
BTS-5STO	-5.52	-4.91	-4.00	-3.57	-3.32
BTS-10STO	-1.03	-0.86	-0.76	-0.60	-0.54
BTS-15STO	-0.70	-0.64	-0.54	-0.41	-0.31
BTS-20STO	-1.31	-1.25	-1.07	-0.94	-0.81

later, exhibits high thermal stability. Subsequently, the samples were analyzed using the Hakki-Coleman technique, which allowed the extraction of the following parameters: ε_r (relative permittivity), tgδ (dielectric loss tangent), and Q (quality factor) in the microwave range (67). It is worth noting that the ceramic pieces were geometrically favorable for this measurement, meaning the ratio between the diameter (D) and height (*a*) was 2:1 (67). Table 6 shows the corresponding parameters for each sample. It is observed that with the increase in STO addition, there is a growth in permittivity (ε_r) up to the BTS-10STO composition, accompanied by an increase in the loss tangent (tgδ). However, above this concentration, a reduction in tgδ and an increase in the Q are observed. The BTS-20STO sample stands out for presenting the lowest loss tangent and the highest quality factor.

Table 6 – Microwave Measurements Obtained by the Hakki-Coleman Method.

Samples	a (mm)	D (mm)	ε_r	Tgδ (10^{-3})	Q
BTS	5.07	10.42	9.69	18.79	53.64
BTS-3STO	4.87	10.19	10.29	23.47	42.93
BTS-5STO	4.85	10.18	10.42	31.48	32.04
BTS-10STO	4.79	10.50	10.12	35.12	28.71
BTS-15STO	5.04	10.82	9.56	22.19	45.43
BTS-20STO	5.06	10.79	11.42	9.01	110.50

Source: Prepared by the author.

5.6 Microwave (MW) Range Dielectric Analysis

The results of the thermal analysis using the Silva-Fenandes-Sombra method are shown in Table 7. It was observed that as the concentrations of STO were added, the thermal stability, i.e., the temperature coefficient of the resonance frequency (τ_f) , decreased. The reduction of τ_f in the samples was expected, as STO has τ_f (68). The BTS-3STO sample is within the ideal range to be applied as a DRA, as its $\tau_f \sim$ 1700 ppm/°C (68). The BTS-3STO sample is within the ideal range to be applied as a DRA, as its τ_f s within the ±10 ppm/°C range (44). Figure 41 illustrates the τ_f graph as a function of the STO concentrations.

Table 7 - Measurements of (τ_f) obtained from the samples.

Samples	τ_f (ppm/°C)
BTS	-47.56
BTS-3STO	9.23
BTS-5STO	40.55
BTS-10STO	55.70
BTS-15STO	78.54
BTS-20STO	107.95

Source: Prepared by the author.

Figure 41 – τ_f vs. STO concentration plot.
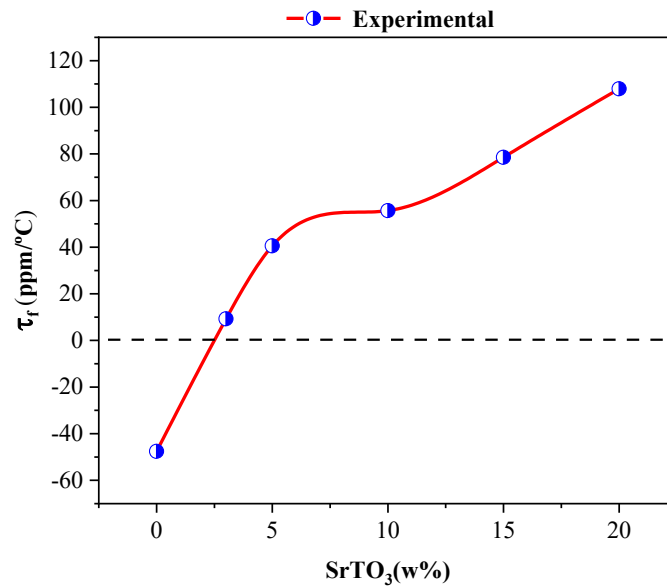
Source: Prepared by the author.

5.7 Analysis of the Numerical Simulation of DRAs

Finally, the data from the Monopole Measurements were used, which measured the reflection coefficient (S_{11}), resonance frequency (f_r), and the real and imaginary impedances (Z', Z''). These experimental data are presented together with the simulated results from HFSS in Table 8. Thus, there is a noticeable good agreement between the experimental and simulated results for all variables, with errors within the range of 5%. It is also observed that, as the percentage of STO in the samples increased, the resonance frequency decreased.

Table 8 – Experimental and simulated measurements of f_r , S_{11} e Z'.

Source: Prepared by the author.

	f_r (GHz)			S_{11} (dB)			Z'$_{peak}$ (Ω)		
	Exp.	Sim.	error (%)	Exp.	Sim.	error (%)	Exp.	Sim.	error (%)
BTS	5.42	5.41	0.24	-27.57	-27.31	0.94	181.39	173.67	4.19
BTS-3STO	5.34	5.33	0.18	-26.56	-27.17	2.24	161.13	164.16	1.88
BTS-5STO	5.25	5.26	0.19	-33.12	-34.27	3.47	221.75	230.86	4.12
BTS-10STO	5.17	5.19	0.38	-23.31	-24.18	3.73	138.78	139.57	0.56
BTS-15STO	4.80	4.81	0.20	-28.98	-30.43	5.00	124.19	125.13	0.75
BTS-20STO	4.74	4.75	0.21	-30.92	-31.98	3.42	118.89	119.92	0.86

.

Figures 42 and 43 show, respectively, the graphs of the S_{11} parameter as a function of the operating frequency and the real and imaginary impedances (Z' and Z''), also as a function of the operating frequency. From these, it is possible to better observe the numerical agreement between the input data and the simulated results of the DRAs.

Figure 42 – Experimental vs. simulated S_{11} parameters.
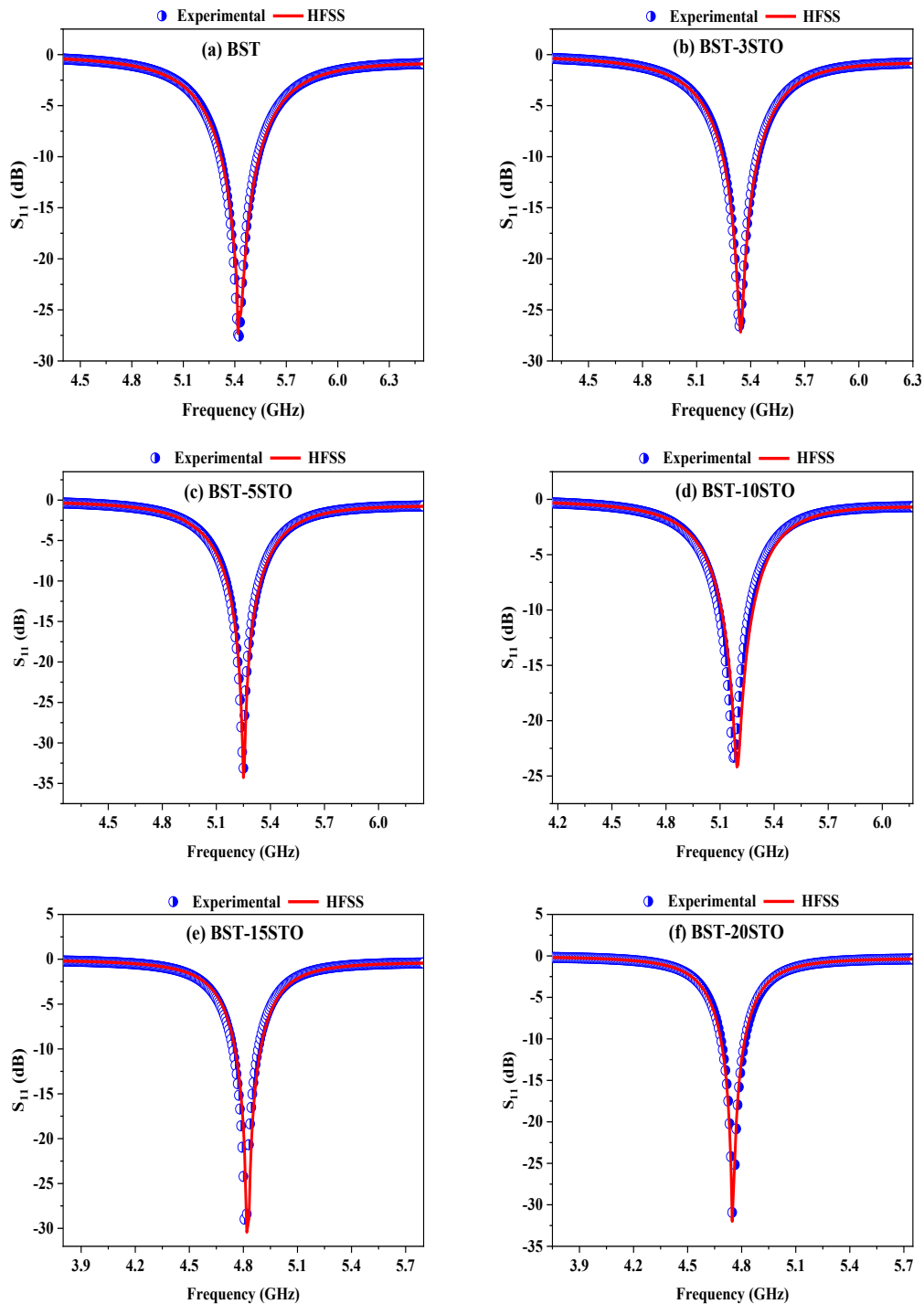
Source: Prepared by the author.

Figure 43 – Experimental vs. simulated Z' and Z" plots.
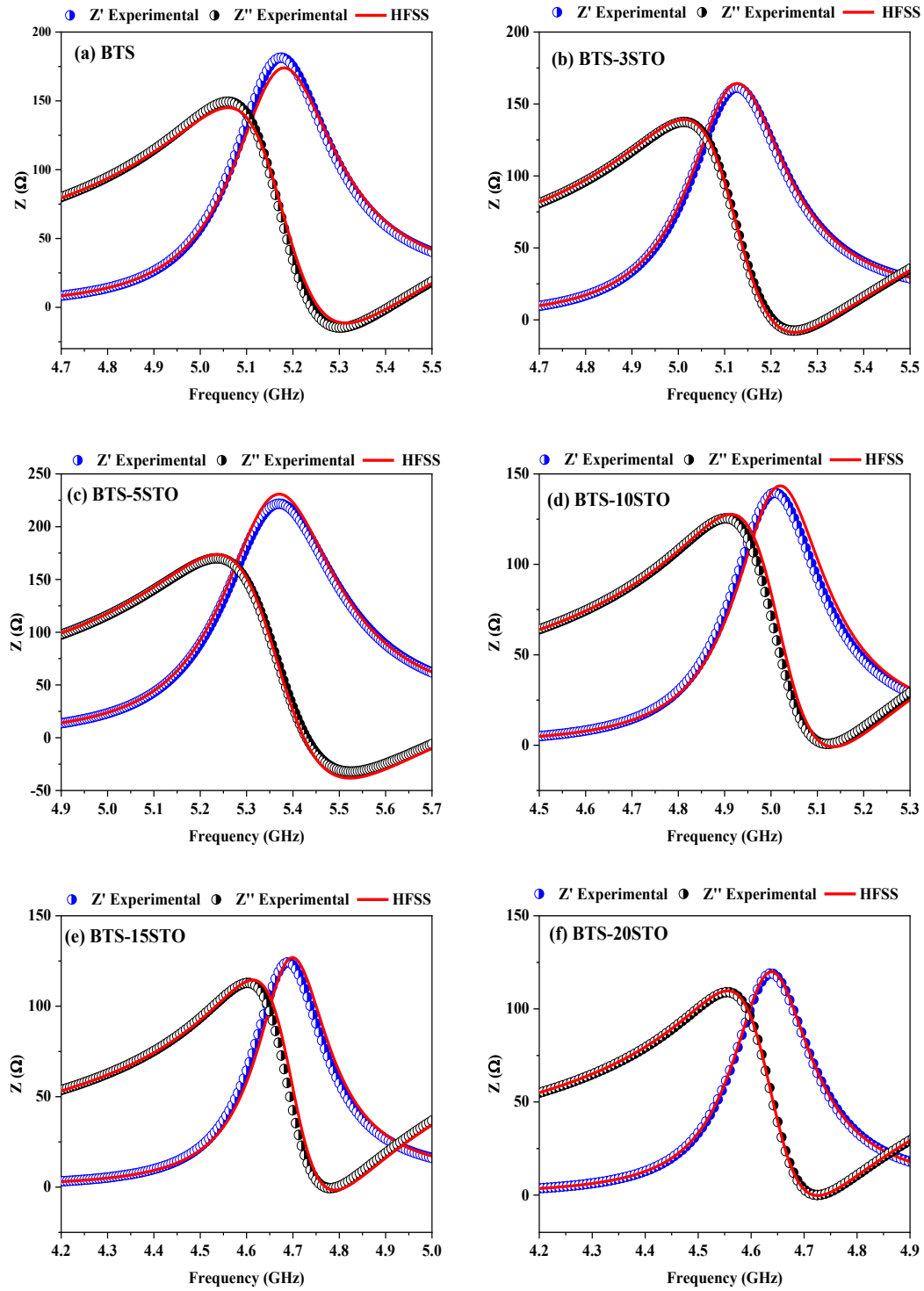
Source: Prepared by the author.

Lastly, the antenna parameters, which were Gain, Directivity, and electromagnetic efficiency, were calculated using HFSS. Table 9 shows these results for all samples. All samples exhibited high efficiency (>96%), especially the BTS-20STO sample, which had the highest gain and directivity.

A general trend was observed where the addition of STO improved the antenna parameters and ensured high electromagnetic efficiency. The gain in dBi of the DRAs is shown in Figure 44.

Table 9 – Radiation characteristics: gain, directivity, and radiation efficiency.

Antenna	Gain (dBi)	Directivity (dBi)	Efficiency (%)
BTS	4.78	4.94	96.76
BTS-3STO	4.73	4.84	97.72
BTS-5STO	5.02	5.13	97.85
BTS-10STO	5.09	5.28	96.25
BTS-15STO	4.83	5.01	96.40
BTS-20STO	5.74	5.89	97.35

Source: Prepared by the author.

Figure 44 – 3D gain patterns (in dBi) of DRAs.
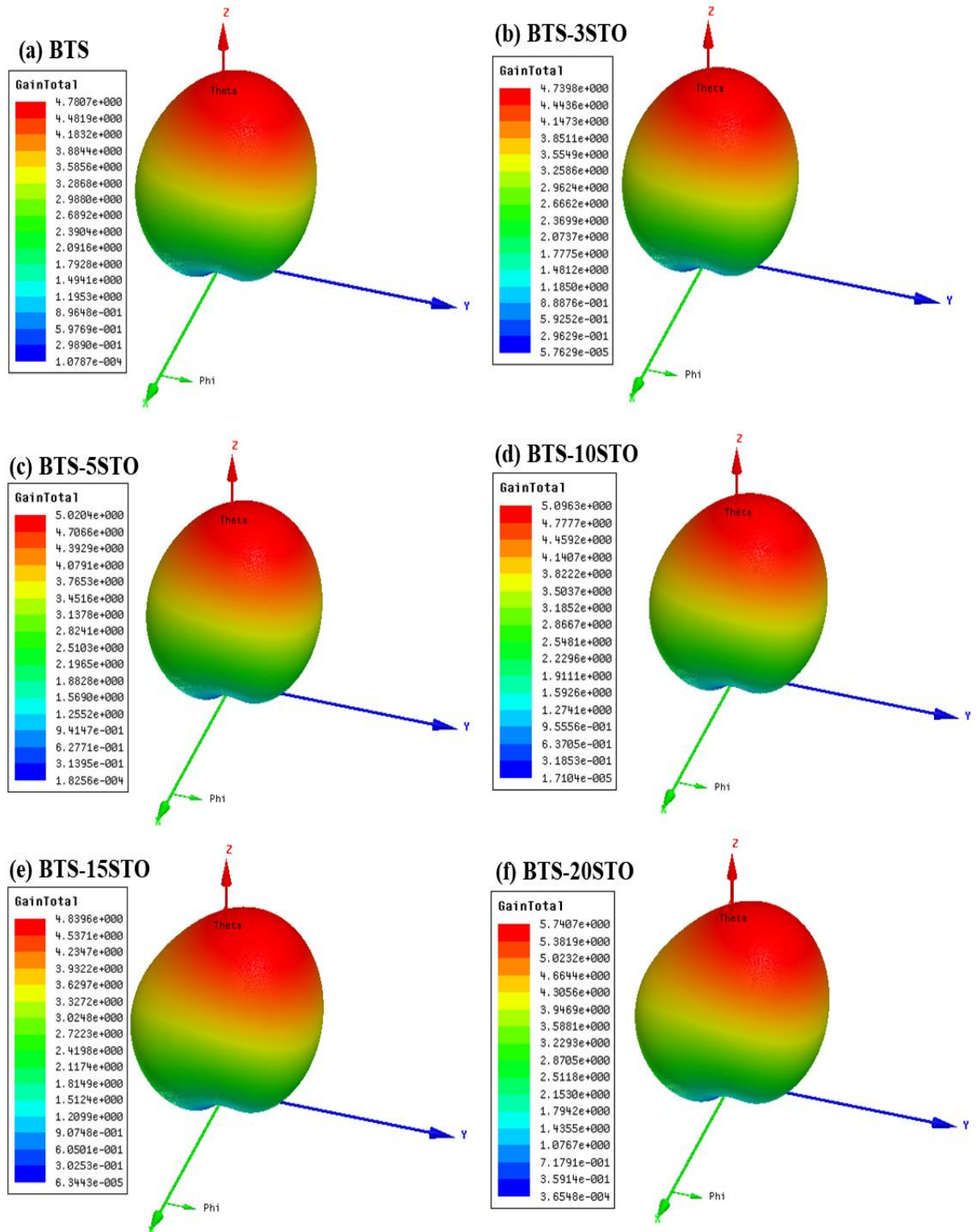
6 CONCLUSIONS

In this thesis, the effects of $SrTiO_3$ (STO) addition on the structural and dielectric properties of BTS in the radio frequency (RF) and microwave (MW) ranges were investigated. X-ray diffraction analysis demonstrated that the addition led to the formation of a secondary $Ba_{0.3}Sr_{0.7}TiO_3$ (BSTO) phase. The material morphology was studied using scanning electron microscopy, revealing a dependence of grain size on the $SrTiO_3$ content.

Subsequently, the electrical properties of the samples in the RF range were studied using impedance spectroscopy (IS), where it was observed that the relative dielectric permittivity (ε_r) progressively increased with STO additions. Through conductivity and impedance analysis, it was possible to conclude that the relaxation effects observed in the samples may have been caused by the Maxwell-Wagner mechanism.

The temperature coefficient of capacitance (TCC) was evaluated, and the BTS–10STO and BTS–15STO samples exhibited values closest to the suitable range for capacitive component applications (± 1500 ppm°C^{-1}). Regarding activation energy, an increase in its value was observed with the addition of $SrTiO_3$, which is attributed to the presence of the secondary BSTO and STO phases, with $E_a = 1.024$ eV and $E_a = 1.31$ eV, respectively.

Concerning dielectric analysis in the MW range, the results indicated that both the resonant frequency (f_r) and the temperature coefficient of resonant frequency (τ_f) decreased with increasing STO content. The significant reduction in τ_f can be explained by the high positive τ_f value of STO ($\tau_f \sim 1700$ ppm/°C). Numerical simulations using HFSS were employed to analyze the materials' behavior as dielectric resonators (DRAs). It was found that all ceramic composites exhibited a return loss (S_{11}) below -10 dB, gain between 4.78 and 5.74 dBi, and radiation efficiency above 96%. Based on the obtained results, BTS and its composites with STO are excellent candidates for DRAs operating in the C-band (4–8 GHz).

7 FUTURE PERSPECTIVES

- Doping BTS with rare-earth ions (Nd^{3+}/Tm^{3+}) to apply these composites in optical devices (markers).
- Producing new ceramic composites by adding $CoFe_2O_4$ to the BTS ceramic matrix for application as magnetic sensors.
- Testing BTS-STO composites using impedance spectroscopy at low temperatures (cryogenic temperatures) to assess potential applications in electronic components.

REFERENCES

1 MOULSON, A. J.; HERBERT, J. M. *Electroceramics: materials, properties, applications*. 1st ed. Chichester: John Wiley & Sons, 2003. Available at: https://doi.org/10.1002/0470867965. Accessed on: Apr. 14, 2025.

2 CALLISTER JR., W. D.; RETHWISCH, D. G. *Materials science and engineering*. Hoboken: John Wiley & Sons, 2014.

3 CHUNG, D. D. L.; XI, X. A review of cement-based materials as electroceramics. *Ceramics International*, Amsterdam, v. 49, n. 15, p. 24621-24642, 2023. Available at: https://doi.org/10.1016/j.ceramint.2023.05.107. Accessed on: Apr. 14, 2025.

4 NEWNHAM, R. E.; CROSS, L. E. Ferroelectricity in silicates. *Materials Research Bulletin*, Oxford, v. 9, p. 1021-1032, 1974.

5 CHANG, Kai. *RF and microwave wireless systems*. Hoboken: John Wiley & Sons, 2004.

6 HAKKI, B. W.; COLEMAN, P. D. A dielectric resonator method of measuring inductive capacities in the millimeter range. *IRE Transactions on Microwave Theory and Techniques*, Piscataway, v. 8, n. 4, p. 402-410, 1960.

7 WAKINO, K. et al. Microwave characteristics of $(Zr,Sn)TiO_4$ and $BaO-PbO-Nd_2O_3-TiO_2$ dielectric resonators. *Journal of the American Ceramic Society*, Hoboken, v. 67, n. 4, p. 278-281, 1984.

8 YADUVANSHI, R. S.; VARSHNEY, G. *Nano dielectric resonator antennas for 5G applications*. 1st ed. Boca Raton: CRC Press, 2020. Available at: https://doi.org/10.1201/9781003029342. Accessed on: Apr. 14, 2025.

9 ALFORS, J. T. et al. Seven new barium minerals from Eastern Fresno County, California. *California Division of Mines and Geology*, Sacramento, 1965.

10 KIMURA, M.; FUJINO, Y.; KAWAMURA, T. New piezoelectric crystal: Synthetic fresnoite ($Ba_2Si_2TiO_8$). *Applied Physics Letters*, Melville, v. 29, n. 4, p. 227-228, 1976.

11 WONG, C. L. et al. Synthesis and crystal chemical evolution of fresnoite powders. *Journal of Solid State Chemistry*, Amsterdam, v. 187, p. 165-171, 2012. Available at: https://doi.org/10.1016/j.jssc.2011.12.031. Accessed on: Apr. 14, 2025.

12 ABREU, R. F. et al. Evaluation of dielectric properties of the barium titanium silicate ($Ba_2TiSi_2O_8$) for microwave applications. *Journal of Materials Science: Materials in Electronics*, Dordrecht, v. 32, p. 7034-7048, 2021. Available at: https://doi.org/10.1007/s10854-021-05414-7. Accessed on: Apr. 14, 2025.

13 ABREU, R. F. et al. Enhanced microwave dielectric properties of the $Ba_2TiSi_2O_8$ ceramic by the addition of TiO_2. *Journal of Electronic Materials*, New York, v. 52, p. 8050-8064, 2023. Available at: https://doi.org/10.1007/s11664-023-10718-x. Accessed on: Apr. 14, 2025.

14 ABREU, R. F. et al. Study of electrical properties with temperature variation by complex impedance spectroscopy (CIS) and effects on the $Ba_2TiSi_2O_8$–TiO_2 matrix. *Applied Physics A*, Heidelberg, v. 130, n. 138, 2024. Available at: https://doi.org/10.1007/s00339-024-07295-z. Accessed on: Apr. 14, 2025.

15 COWLEY, R. A. Lattice dynamics and phase transitions of strontium titanate. *Physical Review*, College Park, v. 134, n. 4A, p. A981-A997, 1964. Available at: https://doi.org/10.1103/PhysRev.134.A981. Accessed on: Apr. 14, 2025.

16 LI, J. et al. Sintering and dielectric properties of $SrTiO_3$-based ceramics. *MRS Online Proceedings Library*, Warrendale, v. 1397, p. 45-51, 2012. Available at: https://doi.org/10.1557/opl.2012.533. Accessed on: Apr. 14, 2025.

17 TKACH, A. et al. Lattice dynamics and dielectric response of Mg-doped $SrTiO_3$ ceramics in a wide frequency range. *Journal of Applied Physics*, Melville, v. 97, n. 4, p. 044104, 2005. Available at: https://doi.org/10.1063/1.1849822. Accessed on: Apr. 14, 2025.

18 LI, L. et al. The thermal sensitivity and dielectric properties of $SrTiO_3$-based ceramics. *Ceramics International*, Amsterdam, v. 30, n. 7, p. 1073-1078, 2004.

19 KOONCE, C. S. et al. Superconducting transition temperatures of semiconducting $SrTiO_3$. *Physical Review*, College Park, v. 163, n. 2, p. 380-390, 1967. Available at: https://doi.org/10.1103/PhysRev.163.380. Accessed on: Apr. 14, 2025.

20 PANDEY, R. K. (ed.). *Fundamentals of electroceramics*. Hoboken: John Wiley & Sons, 2019. Available at: https://doi.org/10.1002/9781119057352. Accessed on: Apr. 14, 2025.

21 RIETVELD, H. M. A profile refinement method for nuclear and magnetic structures. *Journal of Applied Crystallography*, Copenhagen, v. 2, p. 65-71, 1969.

22 RIETVELD, H. M. Line profiles of neutron powder-diffraction peaks for structure refinement. *Acta Crystallographica*, Copenhagen, v. 22, p. 151-152, 1967.

23 GOLDSTEIN, J. et al. *Scanning electron microscopy and X-ray microanalysis*. 4th ed. New York: Springer, 2017.

24 REIMER, L. *Scanning electron microscopy: physics of image formation and microanalysis*. 2nd ed. Berlin: Springer, 1998.

25 GRIFFITHS, D. J. *Introduction to electrodynamics*. 4th ed. Cambridge: Cambridge University Press, 2013.

26 NUSSENZVEIG, H. M. *Curso de física básica: eletromagnetismo*. v. 3. São Paulo: Edgard Blücher, 1997.

27 YOUNG, H. D. et al. *Física III: eletromagnetismo*. 12th ed. São Paulo: Pearson, 2009.

28 BARSOUKOV, E.; MACDONALD, J. R. *Impedance spectroscopy: theory, experiment, and applications*. 2nd ed. Hoboken: John Wiley & Sons, 2005.

29 INTERNATIONAL ELECTROTECHNICAL COMMISSION. *IEC 60384-8: fixed capacitors for use in electronic equipment – Part 8: sectional specification – fixed capacitors of ceramic dielectric, Class 1*. Geneva: IEC, 2020.

30 JONSCHER, A. K. *Dielectric relaxation in solids*. London: Chelsea Dielectrics Press, 1983.

31 COLE, K. S.; COLE, R. H. Dispersion and absorption in dielectrics. *The Journal of Chemical Physics*, Melville, v. 9, n. 4, p. 341-351, 1941. Available at: https://doi.org/10.1063/1.1750906. Accessed on: Apr. 14, 2025.

32 DAVIDSON, D. W.; COLE, R. H. Dielectric relaxation in glycerine. *The Journal of Chemical Physics*, Melville, v. 19, n. 12, p. 1484-1490, 1951. Available at: https://doi.org/10.1063/1.1748105. Accessed on: Apr. 14, 2025.

33 HAVRILIACK, S.; NEGAMI, S. A complex plane representation of dielectric and mechanical relaxation processes in some polymers. *Polymer*, Amsterdam, v. 8, n. 4, p. 161-210, 1967. Available at: https://doi.org/10.1016/0032-3861(67)90021-3. Accessed on: Apr. 14, 2025.

34 SILLARS, R. W. The properties of a dielectric containing semiconducting particles of various shapes. *Journal of the Institution of Electrical Engineers*, London, v. 80, n. 484, p. 378-394, 1937. Available at: https://doi.org/10.1049/pws.1937.0015. Accessed on: Apr. 14, 2025.

35 MACDONALD, J. R. *Impedance spectroscopy: theory, experiment, and applications*. 3rd ed. Hoboken: Wiley, 2005.

36 PETOSA, A. *Dielectric resonator antenna handbook*. Norwood: Artech House, 2007.

37 KAJFEZ, D.; GUILLON, P. *Dielectric resonators*. 2nd ed. Atlanta: Noble Publishing, 1998.

38 BALANIS, C. A. *Antenna theory: analysis and design*. 3rd ed. Hoboken: Wiley, 2005.

39 LONG, S. A. et al. The resonant cylindrical dielectric cavity antenna. *IEEE Transactions on Antennas and Propagation*, Piscataway, v. 31, n. 3, p. 406-412, 1983.

40 JUNKER, G. P. et al. Effect of air gap on cylindrical dielectric resonator antenna operating in TM01 mode. *Electronics Letters*, Stevenage, v. 30, n. 2, p. 97-98, 1994.

41 JUNKER, G. P. et al. Effect of fabrication imperfections for ground-plane-backed dielectric-resonator antennas. *IEEE Antennas and Propagation Magazine*, Piscataway, v. 37, n. 1, p. 40-47, 1995.

42 HAKKI, B. W.; COLEMAN, P. D. A dielectric resonator method of measuring inductive capacities in the millimeter range. *IRE Transactions on Microwave Theory and Techniques*, Piscataway, v. 8, n. 4, p. 402-410, 1960.

43 SILVA, M. A. S. et al. An alternative method for the measurement of the microwave temperature coefficient of resonant frequency (τf). *Journal of Applied Physics*, Melville, v. 112, n. 7, p. 074106, 2012. Available at: https://doi.org/10.1063/1.4755799. Accessed on: Apr. 14, 2025.

44 SEBASTIAN, M. T. et al. Measurement of microwave dielectric properties and factors affecting them. *In:* SEBASTIAN, M. T.; JANTUNEN, H. (ed.). *Microwave materials and applications*. Chichester: John Wiley & Sons, 2017. V. 1, p. 1-51.

45 SKOOG, D. A. et al. *Fundamentals of analytical chemistry*. 9th ed. São Paulo: Cengage Learning, 2014.

46 KARAMANOV, A.; PELINO, M. Evaluation of the degree of 79rystallization in glass-ceramics by density measurements. *Journal of the European Ceramic Society*, Amsterdam, v. 19, n. 5, p. 649-654, 1999.

47 SHARIF, N. S. A. et al. Improved densification and dielectric properties of ZBS-doped ceramics. *Journal of Materials Science*, Dordrecht, v. 53, p. 12345-12356, 2018.

48 GERMAN, R. M. Coarsening in sintering: grain shape distribution, grain size distribution, and grain growth kinetics in solid-pore systems. *Critical Reviews in Solid State and Materials Sciences*, Boca Raton, v. 35, n. 4, p. 263-305, 2010.

49 KRELL, A.; KLIMKE, J. Effects of the homogeneity of particle coordination on solid-state sintering of transparent alumina. *Journal of the American Ceramic Society*, Hoboken, v. 89, n. 6, p. 1985-1992, 2006.

50 WANG, J. et al. Effective strategy to optimize energy storage properties and dielectric relaxation behaviors of strontium barium titanate ceramics. *Journal of Materials Science: Materials in Electronics*, Dordrecht, v. 32, p. 10726-10733, 2021. Available at: https://doi.org/10.1007/s10854-021-05730-y. Accessed on: Apr. 14, 2025.

51 LI, J. et al. Sintering and dielectric properties of $SrTiO_3$-based ceramics. *MRS Online Proceedings Library*, Warrendale, v. 1397, p. 45-51, 2012. Available at: https://doi.org/10.1557/opl.2012.533. Accessed on: Apr. 14, 2025.

52 TKACH, A. et al. Lattice dynamics and dielectric response of Mg-doped $SrTiO_3$ ceramics in a wide frequency range. *Journal of Applied Physics*, Melville, v. 97, n. 4, p. 044104, 2005. Available at: https://doi.org/10.1063/1.1849822. Accessed on: Apr. 14, 2025.

53 LI, L. et al. The thermal sensitivity and dielectric properties of $SrTiO_3$-based ceramics. *Ceramics International*, Amsterdam, v. 30, n. 7, p. 1073-1078, 2004.

54 COLARES, D. da M. et al. Effect of Bi_2O_3 addition on the dielectric properties in radio frequency range of the $BiCu_3Ti_3FeO_{12}$ matrix. *Emergent Materials*, Cham, v. 8, n. 2, p. 615-623, 2025. Available at: https://doi.org/10.1007/s42247-025-01001-2. Accessed on: Apr. 14, 2025.

55 ABREU, R. F. et al. Evaluation of the $Sr_2TiSi_2O_8$ ceramic matrix for radiofrequency and microwave applications. *Journal of Materials Science: Materials in Electronics*, Dordrecht, v. 34, p. 457, 2023. Available at: https://doi.org/10.1007/s10854-023-09925-3. Accessed on: Apr. 14, 2025.

56 MAHATO, D. K. et al. Dielectric relaxation in double perovskite oxide, Ho_2CdTiO_6. *Bulletin of Materials Science*, Bangalore, v. 34, n. 3, p. 455-462, 2011.

57 SAHOO, S. et al. Frequency and temperature dependent electrical characteristics of CaTiO3 nano-ceramic prepared by high-energy ball milling. *Journal of Advance d Ceramics*, Beijing, v. 2, n. 3, p. 291–300, 2013.

58 ACHARYA, T.; CHOUDHARY, R. N. P. Dielectric behavior of manganese titanate in the paraelectric phase. *Applied Physics A*, Heidelberg, v. 121, p. 707-714, 2015. Available at: https://doi.org/10.1007/s00339-015-9463-y. Accessed on: Apr. 14, 2025.

59 PUROHIT, V.; PADHEE, R.; CHOUDHARY, R. N. P. Dielectric and impedance spectroscopy of Bi(Ca0.5Ti0.5)O3 ceramic. *Ceramics International*, Amsterdam, v. 44, n. 4, p. 3993–3999, mar. 2018.

60 BEZERRA JUNIOR, M. H. et al. Impedance spectroscopy analysis of an $FeNbO_4$ matrix with different additions of TiO_2 and the effects of temperature variation. *Journal of Materials Science: Materials in Electronics*, Dordrecht, v. 32, p. 5936-5944, 2021. Available at: https://doi.org/10.1007/s10854-021-05314-w. Accessed on: Apr. 14, 2025.

61 ABREU, T. O. et al. Evaluation of the effect of the addition of TiO_2 on the dielectric behaviour of $YNbO_4$ ceramic using impedance spectroscopy. *Journal of Materials Science:*

Materials in Electronics, Dordrecht, v. 35, p. 570, 2024. Available at: https://doi.org/10.1007/s10854-024-12315-y. Accessed on: Apr. 14, 2025.

62 SALES, J. C. et al. Influence of TiO_2 addition on the $Mg_4Nb_2O_9$ ceramic phase and its application in the radiofrequency region. *Materials Today: Proceedings*, Amsterdam, v. 49, p. 50-55, 2024. Available at: https://doi.org/10.1016/j.matpr.2024.04.089. Accessed on: Apr. 14, 2025.

63 NOGUEIRA, F. E. A. et al. Elevated thermal stability of the dielectric properties of $CaMoO_4$–TiO_2 composites under temperature variations. *Journal of Materials Science: Materials in Electronics*, Dordrecht, v. 35, p. 1470, 2024. Available at: https://doi.org/10.1007/s10854-024-13227-7. Accessed on: Apr. 14, 2025.

64 NOGUEIRA, F. E. A. et al. High thermal stability of the dielectric properties of the $La_2Ti_2O_7$–$La_4Ti_9O_{24}$ composites under temperature variation. *Journal of the Australian Ceramic Society*, Cham, v. 60, n. 3, p. 987-994, 2024. Available at: https://doi.org/10.1007/s41779-024-01106-7. Accessed on: Apr. 14, 2025.

65 LI, J. et al. Sintering and dielectric properties of $SrTiO_3$-based ceramics. *MRS Online Proceedings Library*, Warrendale, v. 1397, p. 45-51, 2012. Available at: https://doi.org/10.1557/opl.2012.533. Accessed on: Apr. 14, 2025.

66 WU, T. et al. Influence of Sr/Ba ratio on the energy storage properties and dielectric relaxation behaviors of strontium barium titanate ceramics. *Journal of Materials Science: Materials in Electronics*, Dordrecht, v. 24, p. 4105-4112, 2013. Available at: https://doi.org/10.1007/s10854-013-1368-y. Accessed on: Apr. 14, 2025.

67 COLARES, D. da M. et al. Improving the microwave dielectric properties of $BiCu_3Ti_3FeO_{12}$ with the addition of Bi_2O_3. *Journal of Electromagnetic Waves and Applications*, London, v. 36, n. 3, p. 321-331, 2022. Available at: https://doi.org/10.1080/09205071.2021.1968958. Accessed on: Apr. 14, 2025.

68 SUN, Y. et al. Dielectric behavior of $(1-x)LaAlO_3$–$xSrTiO_3$ solid solution system at microwave frequencies. *Japanese Journal of Applied Physics*, Tokyo, v. 37, n. 10R, p. 5625-5629, 1998. Available at: https://iopscience.iop.org/1347-4065/37/10R/5625. Accessed on: Apr. 14, 2025.

PUBLICATIONS DERIVED FROM THE THESIS

1- ABREU, R. F.; ABREU, T. O.; COLARES, D. da M.; SATURNO, S. O.; NASCIMENTO, J. P. C.; NOBREGA, F. A. C.; GHOSH, A.; VASCONCELOS, S. J. T.; SALES, J. C.; ANDRADE, H. D. de; QUEIROZ JÚNIOR, I. S.; SOMBRA, A. S. B. Barium titanium silicate ($Ba_2TiSi_2O_8$) for microwave applications. *Journal of Materials Science: Materials in Electronics* , Dordrecht, v. 32, p. 7034-7048, 2021. Available at: https://doi.org/10.1007/s10854-021-05414-7. Accessed on: Apr. 14, 2025.

2- ABREU, R. F.; SATURNO, S. O.; COLARES, D. da M.; SILVA, F. R.; NOBREGA, F. A. C.; NOGUEIRA, F. E. A.; NASCIMENTO, J. P. C.; VASCONCELOS, S. J. T.; CARMO, F. F.; ABREU, T. O.; GHOSH, A.; SALES, J. C.; SILVA, R. S.; SALES, A. J. M.; SILVA, M. A. S.; SOMBRA, A. S. B. Enhanced microwave dielectric properties of the $Ba_2TiSi_2O_8$ ceramic by the addition of TiO_2. *Journal of Electronic Materials Science: Materials in Electronics*, Dordrecht, p. 1-15, 2023. Available at: https://doi.org/10.1007/s11664-023-10718-x. Accessed on: Apr. 14, 2025.

3- ABREU, R. F.; SATURNO, S. O.; NOBREGA, F. A. C.; COLARES, D. da M.; NASCIMENTO, J. P. C.; VASCONCELOS, S. J. T.; NOGUEIRA, F. E. A.; FREITAS, D. B. de; CARMO, F. F.; GHOSH, A.; ABREU, T. O.; SILVA, M. A. S.; SILVA, R. S.; TRUKHANOV, S. V.; ZHOU, D.; SINGH, C.; SOMBRA, A. S. B. Study of electrical properties with temperature variation by complex impedance spectroscopy (CIS) and effects on the $Ba_2TiSi_2O_8$-TiO_2 matrix. *Applied Physics A*, Heidelberg, v. 130, n. 2, p. 1-11, 2024. Available at: https://doi.org/10.1007/s00339-024-07295-z. Accessed on: Apr. 14, 2025

4- ABREU, R. F.; SATURNO, S. O.; COLARES, D. da M.; NOBREGA, F. A. C.; SILVA, P. M. O.; CARMO, F. F.; NASCIMENTO, J. P. C.; ABREU, T. O.; SALES, J. C.; SILVA, M. A. S. da; SILVA, R. S. da; SOMBRA, A. S. B. Increased thermal stability and dielectric properties of $Ba_2TiSi_2O_8$-$CaTiO_3$ composites for high frequency applications. . *Applied Physics A*, Heidelberg,v. 131, p. 391, 2025. Available at: https://doi.org/10.1007/s00339-025-08516-9. Accessed on: Apr. 14, 2025

5- COLARES, D. da M.; ABREU, R. F; NOBREGA, F. A. C.; NASCIMENTO, J. P. C.; CARMO, F. F.; SILVA, M. A. S.; SILVA, R. S.; SINGH, C.; LACERDA, R.; SOMBRA, A. S. B. Effect of $SrTiO_3$ addition on the thermal stability of $Ba_2TiSi_2O_8$ matrix in the radio frequency range. *Ceramics International*, Amsterdam, 2025 Available at: https://doi.org/10.1016/j.ceramint.2025.07.315. Accessed on: Apr. 14, 2025.

OTHER RELEVANT PUBLICATIONS

1- COLARES, D. da M.; ABREU, R. F.; SILVA, F. R.; ABREU, T. O.; NOBREGA, F. A. C.; FREITAS, D. B.; NASCIMENTO, J. P. C.; OLIVEIRA, F. G. S.; VASCONCELOS, I. F.; GHOSH, A.; VASCONCELOS, S. J. T.; SALES, J. C.; SILVA, R. S.; SOMBRA, A. S. B. Improving the microwave dielectric properties of $BiCu_3Ti_3FeO_{12}$ with the addition of Bi_2O_3. *Journal of Electromagnetic Waves and Applications*, Lodon, v. 36, n. 3, p. 321-331, 2021. Available at: https://doi.org/10.1080/09205071.2021.1968958. Accessed on: Apr. 14, 2025.

2- NOBREGA, F. A. C.; ABREU, R. F.; COLARES, D. D. M.; SILVA, M. A. S.; CARMO, F. F.; ABREU, T. O.; SOMBRA, A. S. B. Influence of the addition of $CaTiO_3$ on the microwave dielectric properties of the $BaMoO_4$ matrix. *Materials Chemistry and Physics*, Amsterdam, v. 289, p. 126478, 2022. Available on: https://doi.org/10.1016/j.matchemphys.2022.126478. Accessed on: Apr. 14, 2025.

3- COLARES, D. da M.; ABREU, R. F.; NOBREGA, F. A. C.; NASCIMENTO, J. P. C.; FREITAS, D. B.; CARMO, F. F.; ABREU, T. O.; SILVA, M. A. S.; SILVA, R. S.; SOMBRA, A. S. B. Effect of Bi_2O_3 Addition on the dielectric properties in radio frequency range of the $BiCu_3Ti_3FeO_{12}$ matrix. *Emergent Materials*, Lodon, 2025. Available on: https://doi.org/10.1007/s42247-025-01001-2. Accessed on: Apr. 14, 2025.

4- ABREU, R. F.; NOBREGA, F. A. C.; COLARES, D. da M.; SATURNO, S. O.; NASCIMENTO, J. P. C.; ABREU, T. O.; GHOSH, A.; CARMO, F. F.; SILVA, M. A. S.; SALES, A. J. M.; SILVA, R. S.; SOMBRA, A. S. B. Evaluation of the $Sr_2TiSi_2O_8$ ceramic matrix for radiofrequency and microwave applications. *Journal of materials science: materials in electronics*, Dordrecht, v. 34, n. 457, 2023 Available on: https://doi.org/10.1007/s10854-023-09925-3. Accessed on: Apr. 14, 2025.

FILED PATENTS

1- SOMBRA, A. S. B.; COLARES, D. da M.; FREITAS, D. B. de; ABREU, R. F.; VASCONCELOS, S. J. T. A new $BiCu_3Ti_3FeO_{12}$ (BCTFO) composite with bismuth oxide (Bi_2O_3) addition with a temperature coefficient of resonant frequency (τf) close to zero in the microwave region. Brazil, Protocol: BR 10 2020 005805-3. Deposit date: Mar. 24, 2020.

2- SOMBRA, A. S. B.; MACHADO, Y. de L.; BESSA, V. L.; COLARES, D. da M.; SILVA, A. J. O. da; FREIRE, F. N. A.; NASCIMENTO, J. P. C. do; ABREU, T. O.; SILVA, M. A. S. da. Synthesis and characterization of lanthanum vanadate $LaVO_4$ (LVO) and titanium dioxide (TiO_2) composite with a temperature coefficient of resonant frequency (τf) close to zero for microwave engineering applications. Brazil, Protocol: BR 10 2020 020636-2. Deposit date: Oct. 7, 2020.

3- SOMBRA, A. S. B.; ABREU, R. F.; COLARES, D. da M.; ABREU, T. O.; NOBREGA, F. A. C.; SILVA, A. J. O. da; SATURNO, S. O.; SILVA, F. R. da; NASCIMENTO, J. P. C. do; MACHADO, Y. de L. Enhanced thermal stability of the $Ba_2TiSi_2O_8$ matrix with TiO_2 addition for operation in the microwave region. Brazil, Protocol: BR 10 2021 015932-4. Deposit date: Aug. 12, 2021.

4- SOMBRA, A. S. B.; ABREU, R. F.; SILVA, M. A. S. da; CARMO, F. F. do; COLARES, D. da M.; NOBREGA, F. A. C.; NASCIMENTO, J. P. C. do; ABREU, T. O. Development of a new $Sr_2TiSi_2O_8$ dielectric matrix with high thermal stability in the microwave region. Brazil, Protocol: BR 10 2022 015899-1. Deposit date: Aug. 11, 2022. Publication date: Feb. 20, 2024.

5- SOMBRA, A. S. B.; COLARES, D. da M.; ABREU, R. F.; NASCIMENTO, J. P. C. do; NOBREGA, F. A. C.; CARMO, F. F. do; SILVA, M. A. S. da; SATURNO, S. O. High thermal stability of the $Ba_2TiSi_2O_8$ matrix with $SrTiO_3$ addition for use in microwave region components. Brazil, Protocol: BR 10 2024 016638-8. Deposit date: Aug. 14, 2024.

ANNEX A - IMPROVING THE MICROWAVE DIELECTRIC PROPERTIES OF BiCu₃Ti₃FeO₁₂ WITH THE ADDITION OF Bi₂O₃. JOURNAL OF ELECTROMAGNETIC WAVES AND APPLICATIONS.

Improving the microwave dielectric properties of BiCu₃Ti₃FeO₁₂ with the addition of Bi₂O₃

D. da M. Colares [a,b], R. F. Abreu [a,b], F. R. Silva [d], T. O. Abreu [b,c], F. A. C. Nobrega [b,c], D. B. Freitas[a,b], J. P. C. do Nascimento[b,d], F. G. S. Oliveira[e], I. F. Vasconcelos[e], A. Ghosh[f], S. J. T. Vasconcelos[c,d], J. C. Sales [g], R. S. Silva[h] and A. S. B. Sombra [b]

[a]Telecommunication Engineering Department, Federal University of Ceará (UFC), Fortaleza, Brazil; [b]LOCEM-Telecommunication and Materials Science and Engineering of Laboratory (LOCEM), Physics Department, Federal University of Ceará (UFC), Campus PICI, Fortaleza, Ceará, Brazil; [c]Department of Organic and Inorganic Chemistry, Science Center, Federal University of Ceará (UFC), Brazil; [d]Federal Institute of Education, Science and Technology of Ceará, PPGET, Fortaleza, Brazil; [e]Department of Metallurgical and Materials Engineering, Technology Center, Federal University of Ceará Campus do Pici, Fortaleza, Brazil; [f]LaMFA - Advanced Functional Materials Laboratory, Central Analítica, Physics Department, Federal University of Ceará - UFC, Fortaleza, Brazil; [g]Department of Civil Engineering, State University of Vale do Acaraú, Center for Exact Sciences and Technology; [h]Group Functional Nanomaterials, Physics Department, Federal University of Sergipe, Sao Cristóvão, SE, Brazil

ABSTRACT
In this work, the influence of the addition of Bi_2O_3 on the dielectric properties in the microwave range of $BiCu_3Ti_3FeO_{12}$ (BCTFO) ceramic matrix and its potential application as a dielectric resonator antenna are analysed. X-ray diffraction shows that a reaction between BCTFO and Bi_2O_3 occurs that results in the formation of new crystalline phases. The morphology of the samples is studied by field-emission scanning electron microscopy and demonstrates a dependence of the grain size on the Bi_2O_3 content. From the Mössbauer spectroscopic analysis, it is found that the Fe^{3+} ions replace the Ti^{4+} in the crystalline structure. The addition of Bi_2O_3 also reduces the dielectric permittivity (ϵ_r), dielectric loss (tan δ) and the coefficient of the resonance frequency (τ_f) values. Finally, numerical simulations are carried out in order to obtain the antenna parameters and they demonstrate that BCTFO could be a potential candidate for devices operating in the S-band.

1. Introduction

Electroceramic materials are known to exhibit interesting physical properties, such as electro-optical, acoustic-optical and non-linear dielectric effects, superconductivity and magnetism, which allow them to be applied in a wide range of applications. In particular, the dielectric properties of electroceramics, such as high permittivity and low losses, are crucial because they enable reductions in the size and cost of electronic components.

ANNEX B - EVALUATION OF DIELECTRIC PROPERTIES OF THE BARIUM TITANIUM SILICATE (Ba₂TiSi₂O₈) FOR MICROWAVE APPLICATIONS. JOURNAL OF MATERIALS SCIENCE: MATERIALS IN ELECTRONICS.

Evaluation of dielectric properties of the barium titanium silicate (Ba$_2$TiSi$_2$O$_8$) for microwave applications

R. F. Abreu[1,4,*], T. O. Abreu[2,·], D. da M. Colares[1,4], S. O. Saturno[1,4], J. P. C. do Nascimento[3,4,*], F. A. C. Nobrega[2], A. Ghosh[6], S. J. T. Vasconcelos[·,4], J. C. Sales[5], H. D. de Andrade[7], I. S. Queiroz Júnior[7], and A. S. B. Sombra[4,7]

[1] Telecommunication Engineering Department, Federal University of Ceará (UFC), Fortaleza, CE 60755-640, Brazil

[2] Department of Organic and Inorganic Chemistry, Science Center, Federal University of Ceará (UFC), Fortaleza, CE, Brazil

[3] Federal Institute of Education, Science and Technology of Ceará, PPGET, Fortaleza, CE, Brazil

[4] LOCEM - Telecommunications and Materials Science and Engineering of Laboratory (LOCEM), Campus Pici, P.O. Box 6030, Fortaleza, CE 60455-760, Brazil

[5] Department of Civil Engineering, Center for Exact Sciences and Technology, State University of Vale do Acaraú, Sobral, CE, Brazil

[6] LaMFA - Advanced Functional Materials Laboratory, Central Analítica, Physics Department, Federal University of Ceará - UFC, Fortaleza, CE 60440-554, Brazil

[7] Federal University of Semiarid Region, UFERSA, Mossoró, RN 59625-900, Brazil

ABSTRACT

This work presents the dielectric properties of Ba$_2$TiSi$_2$O$_8$ in the Radiofrequency (RF) and Microwave (MW) regions. X-ray diffraction analysis showed that the material was obtained as a single-phase without the presence of spurious phases. Complex impedance spectroscopy demonstrated that there was no significant change of permittivity with temperature, whereas the dielectric loss was less than 1. Nyquist diagrams were modelled through an equivalent circuit using two associations of R-CPE related to the grain and the grain boundary effects. The MW analysis showed $\varepsilon'_r = 11.01$ and $\tan \delta = 4.55 \times 10^{-2}$, values that are close to the results obtained in the RF region. Moreover, the τ_f value for Ba$_2$TiSi$_2$O$_8$ was equal to $- 47$ ppm/°C which is close to the values adequate for a microwave device application. The numerical simulation demonstrated the operation of the material as a Dielectric Resonator Antenna (DRA), where a reflection coefficient below $- 10$ dB, a realised gain of 6.739 dBi, a bandwidth of 452.96 MHz and a radiation efficiency around 100% were observed. The results indicate that Ba$_2$TiSi$_2$O$_8$ would be an interesting candidate in microwave operating devices in the C-band, as well as in devices operating in RF.

Address correspondence to E-mail: roterdan.fernandes@gmail.com; jpquimico3@gmail.com

ANNEX C - INFLUENCE OF THE ADDITION OF CaTiO₃ ON THE MICROWAVE DIELECTRIC PROPERTIES OF THE BaMoO₄ MATRIX. MATERIALS CHEMISTRY AND PHYSICS.

Influence of the addition of CaTiO₃ on the microwave dielectric properties of the BaMoO₄ matrix

F.A.C. Nobrega [a,c,*], R.F. Abreu [b,c], D.da M. Colares [b,c], M.A.S. Silva [a,c], F.F. do Carmo [a,c], T.O. Abreu [a,c], J.P.C. do Nascimento [d], J.C. Sales [e], R.S. Silva [f], J.C. Goes [c], A.S.B. Sombra [c]

[a] Department of Organic and Inorganic Chemistry, Science Center, Federal University of Ceará (UFC), Brazil
[b] Telecommunication Engineering Department, Federal University of Ceará (UFC), Fortaleza, Ceará, 60755-640, Brazil
[c] LOCEM Telecommunication and Materials Science and Engineering of Laboratory (LOCEM), Physics Department, Federal University of Ceara (UFC), Campus PICI, P. O. Box 6030, Fortaleza, Ceará, 60455-760, Brazil
[d] Federal Institute of Education, Science and Technology of Ceará, PPGET, Fortaleza, Ceará, Brazil
[e] State University of Vale do Acaraú, Center for Exact Sciences and Technology, Department of Civil Engineering, Brazil
[f] Group Functional Nanomaterials, Physics Department, Federal University of Sergipe, 49100 000, São Cristóvão, SE, Brazil

HIGHLIGHTS

- BaMoO₄ – CaTiO₃ composites demonstrated thermal-stability in the microwave region.
- New LTCC materials were obtained based on BaMoO₄ and CaTiO₃ phases.
- DRAs investigated can be used in S and C-band applications.

ARTICLE INFO

ABSTRACT

This work presents the study of the dielectric properties in the microwave region (MW) of BaMoO₄ ceramic and composites with CaTiO₃ (CTO). The BaMoO₄ matrix was synthesized by solid state reaction and characterized by X-ray diffraction. Ceramic composites were obtained by adding 20–80 mol% of CTO in the BaMoO4 matrix. The Silva-Fernandes-Sombra method was used to measure the resonant frequency temperature coefficient (τ_f), and the BaMoO₄ composite with 20% CTO showed an adequate value of relative dielectric permittivity ($\varepsilon_r = 8.90$), low dielectric loss tangent (tan $\delta = 9.89.10^{-4}$) and τ_f close to zero ($\tau_f = 3.48$ ppm °C^{-1}). BMO and its composites were applied as dielectric resonator antennas, and their far-field parameters were obtained through numerical simulation.

1. Introduction

Dielectric ceramics have attracted great attention from research and industry sectors due to their high values of permittivity and low values of dielectric loss, characteristics that give these ceramics the possibility of miniaturization and applications in various electronic circuits [1–5].

Barium molybdate, BaMoO₄ (BMO) is one of the most important inorganic materials among the molybdate families. This ceramic has a Scheelite-like structure and has numerous applications including solid state lasers, optical fibers, among others [6,7]. In the microwave region (MW) the BMO has the following properties: low relative dielectric permittivity ($\varepsilon_r = 9.84$), low loss tangent (tan $\delta = 5 \cdot 10^{-4}$), and moderate

value of the temperature coefficient of the resonant frequency ($\tau_f = -64$ ppm °C^{-1}), properties that are relevant for applications in devices that in this frequency range [8,9].

The τ_f of the BMO is far from the value considered ideal $-10 < \tau_f < 10$ ppm °C^{-1}, however, there is the possibility of obtaining a compound in this range of values, through the manufacture of ceramic composites with other ceramic materials with values of τ_f positive. Many titanates from the perovskite family have positive τ_f values such as CaTiO₃ (CTO) [1]. Thus, they are promising candidates for the fabrication of a ceramic composite with τ_f close to zero. CTO was chosen because of its wide range of technological applications, from microwaves to radio frequencies, and for its dielectric interesting properties: $\varepsilon_r = 156.83$, tan δ

ANNEX D - EVALUATION OF THE Sr₂TiSi₂O₈ CERAMIC MATRIX FOR RADIOFREQUENCY AND MICROWAVE APPLICATIONS. JOURNAL OF MATERIALS SCIENCE: MATERIALS IN ELECTRONICS.

Evaluation of the Sr₂TiSi₂O₈ ceramic matrix for radiofrequency and microwave applications

R. F. Abreu[1,2], F. A. C. Nobrega[2], D. da M. Colares[1,2], S. O. Saturno[1,2], J. P. C. do Nascimento[2,4,*], T. O. Abreu[2,3], A. Ghosh[5], F. F. do Carmo, M. A. S. Silva[2], A. J. M. Sales[2], R. S. Silva[6], and A. S. B. Sombra[2,6]

[1] Telecommunication Engineering Department, Federal University of Ceará (UFC), Fortaleza, Ceará 60755-640, Brazil

[2] LOCEM-Telecommunication and Materials Science and Engineering of Laboratory (LOCEM), Physics Department, Federal University of Ceará (UFC), Campus PICI, P.O. Box 6030, Fortaleza, Ceará 60455-760, Brazil

[3] Department of Organic and Inorganic Chemistry, Science Center, Federal University of Ceará (UFC), Fortaleza, Brazil

[4] Federal Institute of Education, Science and Technology of Ceará, PPGET, Fortaleza, Ceará, Brazil

[5] LaMFA - Advanced Functional Materials Laboratory, Central Analítica, Physics Department, Federal University of Ceará - UFC, Fortaleza, Ceará 60440-554, Brazil

[6] Group Functional Nanomaterials, Physics Department, Federal University of Sergipe, São Cristóvão, SE 49100-000, Brazil

ABSTRACT

This paper reviews the dielectric properties of Sr₂TiSi₂O₈ (STS) ceramic in the radio frequency (RF) and microwave (MW) regions. X-ray diffraction (XRD) analysis is used to demonstrate that a small secondary phase of $SrTiO_3$ is present in a synthesised STS ceramic. Complex impedance spectroscopy is performed, and the typical permittivity values of ceramic materials are observed. Nyquist diagrams are fitted based on an equivalent circuit using two associations of R-CPE related to the grain and the grain boundary effects. A dependence study of the changes in AC conductivity with frequency at different temperatures demonstrates that the conduction process is thermally activated, and a value of 1.0 eV is obtained for the activation energy. In the MW range, we observe values of $\varepsilon_r = 12.7$, $\tan \delta = 1.3 \times 10^{-2}$, and $\tau_f = -6.1$ ppm/°C, indicating interesting properties for applications in devices that operate in the MW region. A numerical simulation is employed to evaluate STS ceramic as a dielectric resonator antenna, and we observe a reflection coefficient of below -10 dB, a realised gain of 4.6 dBi, a bandwidth of 475 MHz, and a radiation efficiency of around 75%. The properties of the STS matrix presented here indicate that this ceramic would be a suitable candidate for the operation of devices in the C-band, as well as in devices operating in the RF range.

Address correspondence to E-mail: jpquimico3@gmail.com

Springer

ANNEX E - ENHANCED MICROWAVE DIELECTRIC PROPERTIES OF THE Ba$_2$TiSi$_2$O$_8$ CERAMIC BY THE ADDITION OF TIO$_2$. JOURNAL OF ELECTRONIC MATERIALS

Study of electrical properties with temperature variation by complex impedance spectroscopy (CIS) and effects on the Ba$_2$TiSi$_2$O$_8$–TiO$_2$ matrix

R. F. Abreu[1,2] · S. O. Saturno[1,2] · F. A. C. Nobrega[2,3] · D. da M. Colares[1,2] · J. P. C. do Nascimento[4] · S. J. T. Vasconcelos[2] · F. E. A. Nogueira[1,2] · D. B. de Freitas · P. F. do Carmo[3] · A. Ghosh[5] · T. O. Abreu[2,3,11] · M. A. S. Silva[2] · R. S. Silva[6] · S. V. Trukhanov[7,8] · Di Zhou[9] · C. Singh[10] · A. S. B. Sombra[1,2]

Abstract

The present work shows the dielectric properties of (100-X)Ba$_2$TiSi$_2$O$_8$–(X)TiO$_2$ composites (X in wt%) at radio frequency (RF) region (<300 MHz). X-ray diffraction and Rietveld's refinement showed the presence of Ba$_2$(Ti$_{7/9}$Si$_{2/9}$)$_9$O$_{20}$ (BTSO) phase in the studied composites. To analyze the relationship between the electrical properties and the microstructure of the matrix and composites, Impedance spectroscopy (IS) was used. The applied model that best describes the behavior found in the samples is the Havriliak–Negami model. From the IS it was observed that the dielectric relative permittivity presented high values in BTS10 ($X = 10\%$) and BTS20 ($X = 20\%$) which allows classifying them as Colossal permittivity materials. This is an important result due to the potential for applications in new storage systems, capacitive devices and microelectronics. Nyquist diagrams were employed to evaluate the contribution of the grain and grain boundary in the electrical response of the samples and fitted employing an equivalent circuit with two associations of R-CPE (constant phase element). Temperature coefficient of capacitance (TCC) was also obtained and it was possible to observe that there was an increase in the TCC value for the compounds in all frequencies. In addition, IS demonstrated that the activation energy decreasing with TiO$_2$ addition indicating a decrease in the resistive character of the materials.

Keywords Colossal permittivity · Ba$_2$TiSi$_2$O$_8$–TiO$_2$ composites · Impedance spectroscopy (IS)

✉ J. P. C. do Nascimento
jpquimico3@gmail.com

R. F. Abreu
roterdan.fernandes@gmail.com

1. Telecommunication Engineering Department, Federal University of Ceará (UFC), Fortaleza, Ceará 60755-640, Brazil

2. LOCEM-Telecommunication and Materials Science and Engineering of Laboratory (LOCEM)Physics Department, Federal University of Ceará (UFC), Campus PICI, P.O. Box 6030, Fortaleza, Ceará 60455-760, Brazil

3. Department of Organic and Inorganic Chemistry, Science Center, Federal University of Ceará (UFC), Fortaleza, Ceará, Brazil

4. Federal Institute of Education, Science and Technology of Ceará, PPGET, Fortaleza, Ceará, Brazil

5. Department of Chemical and Materials Engineering, DEQM, Pontifical Catholic University of Rio de Janeiro, Rio de Janeiro, Rio de Janeiro, Brazil

6. Group Functional Nanomaterials, Physics Department, Federal University of Sergipe, São Cristóvão, SE 49100-000, Brazil

7. Smart Sensors Systems Laboratory, National University, of Science and Technology MISiS, Moscow 119049, Russia

8. Laboratory of Magnetic Films Physics, Scientific Practical Materials Research Centre, NAS of Belarus, 220072 Minsk, Belarus

9. Electronic Materials Research Laboratory, Xi'an Jiaotong University, Xi'an 710049, China

10. School of Electronics and Electrical Engineering, Lovely Professional University, Phagwara, Punjab 144411, India

11. Instituto Federal de Educação, Ciência e Tecnologia do Ceará (IFCE), Campus Camocim, Camocim, CE 62400-000, Brazil

ANNEX F - STUDY OF ELECTRICAL PROPERTIES WITH TEMPERATURE VARIATION BY COMPLEX IMPEDANCE SPECTROSCOPY (CIS) AND EFFECTS ON THE Ba2TiSi2O8–TiO2 MATRIX. APPLIED PHYSICS A

ORIGINAL RESEARCH ARTICLE

Enhanced Microwave Dielectric Properties of the Ba$_2$TiSi$_2$O$_8$ Ceramic by the Addition of TiO$_2$

R. F. Abreu[1,2] · S. O. Saturno[1,2] · D. da M. Colares[1,2] · F. R. Silva[3] · F. A. C. Nobrega[2,4] · F. E. A Nogueira[1,2] · J. P. C do Nascimento[2,5] · S. J. T. Vasconcelos[2] · F. F. do Carmo[4] · T. O. Abreu[2,4] · A. Ghosh[6] · J. C. Sales[7] · R. S. Silva[8] · A. J. M. Sales[2] · M. A. S. Silva[2] · A. S. B. Sombra[2]

Abstract

This work studies the dielectric properties in the microwave region (MW) of the Ba$_2$TiSi$_2$O$_8$ (BTS) ceramic with TiO$_2$ additions and its applications as a dielectric resonator antenna (DRA). In this study, structural characterization through x-ray diffraction (XRD) is performed and the Rietveld refinement is used to confirm the phases formed. Analysis of the morphology of the materials is performed using scanning electron microscopy (SEM). The resonant frequency temperature coefficient (τ_f) reveals a variation from -47.0 ppm°C^{-1} to $+16.5$ ppm°C^{-1}. The dielectric properties in the MW region reveal an increase in the dielectric permittivity (ε_r) and a decrease in the loss tangent (tanδ) of the samples. Numerical simulation shows good fits of the experimental data, with gain and directivity standing out, ranging from 4 dBi to 6 dBi and radiation efficiency below 80%. The results demonstrate that the samples can operate in C-band electronics, Wi-Fi devices, meteorological radar systems, etc.

Keywords Dielectric properties · microwave · Ba$_2$TiSi$_2$O$_8$ · DRA · numerical simulation

Introduction

The need for technological innovation, miniaturization of electronic components, and the rise of microwave engineering has contributed strongly to a rapid expansion in the search for dielectric resonators (DR). DRs are extremely versatile and can assume different functions, such as oscillators, amplifiers, tuners, and antennas in microwave communication circuits. They also have advantages over other devices, as they are easily compressed and integrated into electronic circuits, with reduced antenna sizes, and avoiding radiation losses.[1–3] Ceramic materials are interesting candidates for these applications due to their low loss, moderate dielectric constant (ε_r), and other properties.[4–8]

Initial reports of Ba$_2$TiSi$_2$O$_8$ (BTS) ceramic dates back to 1960, when it was first observed at Rush Creek.[9–11] BTS

✉ R. F. Abreu
  roterdan.fernandes@gmail.com

1 Telecommunication Engineering Department, Federal University of Ceará (UFC), Fortaleza, Ceará 60755-640, Brazil

2 LOCEM-Telecommunication and Materials Science and Engineering of Laboratory (LOCEM), Physics Department, Federal University of Ceará (UFC), Campus PICI, P.O. Box 6030, Fortaleza, Ceará 60455-760, Brazil

3 Department of Materials Science and Engineering, Federal University of Ceará, Fortaleza, CE 60440-554, Brazil

4 Department of Organic and Inorganic Chemistry, Science Center, Federal University of Ceará (UFC), Fortaleza, CE, Brazil

5 Federal Institute of Education, Science and Technology of Ceará, PPGET, Fortaleza, Ceará, Brazil

6 LaMFA - Advanced Functional Materials Laboratory, Physics Department, Central Analítica, Federal University of Ceará - UFC, Fortaleza, Ceará 60440-554, Brazil

7 State University of Acaraú Valley, Center for Exact Sciences and Technology, Department of Civil Engineering, Sobral, Ceará, Brazil

8 Group Functional Nanomaterials, Physics Department, Federal University of Sergipe, São Cristóvão, SE 49100-000, Brazil

ANNEX G - INCREASED THERMAL STABILITY AND DIELECTRIC PROPERTIES OF Ba₂TiSi₂O₈–CaTiO₃ COMPOSITES FOR HIGH FREQUENCY. APPLIED PHYSICS A

Increased thermal stability and dielectric properties of Ba₂TiSi₂O₈-CaTiO₃ composites for high frequency applications

R. F. Abreu[1,2,6] · S. O. Saturno[2] · D. da M. Colares[2,3] · F. A. C. Nobrega[4] · P. M. O. Silva[2] · F. F. do Carmo[2] · J. P. C. do Nascimento[2,5] · T. O. Abreu · J. P. C. do Sales · A. S. da Silva[2] · R. S. da Silva[8] · A. S. B. Sombra[2,8]

Abstract

This work investigated composites formed from $Ba_2TiSi_2O_8 - CaTiO_3$ in the microwave region, as well as their dielectric properties, dielectric permittivity (ε'_r), dielectric loss ($tan\ \delta$), and quality factor ($Q \times fr$). Solid-state synthesis was employed for the preparation of the $Ba_2TiSi_2O_8$ ceramic matrix and the composites were obtained by mixing the matrix with 1%, 3%, 5% and 9% $CaTiO_3$ by weight. The structural characterization was performed through X-ray diffraction (XRD), and the phases were confirmed by Rietveld refinement. Scanning electron microscopy (SEM) was performed to analyze the surface morphology of the samples. The temperature coefficient of resonant frequency (τ_f) was obtained to verify the thermal stability of the samples. An analysis of τ_f, obtained through the Silva-Fernandes-Sombra (SFS) method, revealed that the addition of 5% $CaTiO_3$ provided a significant improvement in the thermal stability of the material (BTS5, $\tau_f = -9.57$ ppm·°C⁻¹). It is noteworthy that the value obtained for this parameter is within the range required for applications in electronic devices operating in the microwave region. The Hakki-Coleman method was used to analyze the dielectric properties of the samples in the microwave region, through which it was possible to observe a subtle increase in the dielectric permittivity ($11.00 \leq \varepsilon'_r \leq 16.71$) and a decreased level of the dielectric loss ($tan\ \delta$) of the samples. Finally, the dielectric resonator antenna (DRA) configuration was used to analyze the potential of the samples operating in the $HE_{11\delta}$ mode.

Keywords Ceramics · $Ba_2TiSi_2O_8$-$CaTiO_3$ · Dielectric properties · Microwave · DRA

1 Introduction

Inorganic materials can be used in a wide range of applications [1–5], whereas Microwave (MW) communications have become pillars in the progress of global technology, enabling a search for new materials with specific properties. In this context, dielectric ceramics stand out, as their application in the MW communications industry has allowed for the reduction of costs and sizes of electronic components, due to their high dielectric permittivities (ε'_r), low dielectric

✉ R. F. Abreu
  roterdan.fernandes@gmail.com

1   Laboratory of Signals and Systems (L2S, UMR 8506), CentraleSupélec and Paris-Saclay University, 3, rue Joliot Curie, Gif-sur-Yvette 91190, France

2   LOCEM-Telecommunication and Materials Science and Engineering of Laboratory (LOCEM), Campus PICI, P.O. Box 6030, Fortaleza, Ceará 60455-760, Brazil

3   Telecommunication Engineering Department, Federal University of Ceará (UFC), Fortaleza, Ceará 60755-640, Brazil

4   Department of Materials Engineering, Leibniz Institute for Polymer Research Dresden – IPF, Hole Straße 6, 01069 Dresden, Germany

5   Federal Institute of Education, Science and Technology of Ceará, PPGET, Fortaleza, Ceará, Brazil

6   Department of Organic and Inorganic Chemistry, Science Center, Federal University of Ceará (UFC), Fortaleza, Brazil

7   Center for Exact Sciences and Technology, Department of Civil Engineering, State University of Acaraú Valley, Sobral, Brazil

8   Group Functional Nanomaterials, Physics Department, Federal University of Sergipe, Sao Cristóvão, SE 49100-000, Brazil

ANNEX H - EFFECT OF Bi₂O₃ ADDITION ON THE DIELECTRIC PROPERTIES IN RADIO FREQUENCY RANGE OF THE BiCu₃Ti₃FeO₁₂ MATRIX. EMERGENT MATERIALS

ORIGINAL ARTICLE

Effect of Bi₂O₃ addition on the dielectric properties in radio frequency range of the BiCu₃Ti₃FeO₁₂ matrix

Diego da Mota Colares[1,2] · Roterdan Fernandes Abreu[1,2] · Francisco Alekson Chaves Nobrega[2,6] · ...ento[2,4] · Daniel Barros de Freitas[1,2] · Felipe Felix do Carmo[2,3] · Tallison Oliveira Abreu[3] · Marcelo Antonio Santos da Silva[2] · Ronaldo Santos da Silva[5] · Antonio Sérgio Bezerra Sombra[1,2]

Abstract
In this work, impedance spectroscopy (IS) was used to examine the dielectric characteristics of the BiCu₃Ti₃FeO₁₂ ceramic matrix added with bismuth oxide (Bi₂O₃) at different concentrations. The presence of new crystalline phases in the composites was investigated using the X-ray analysis (Rietveld refinement method). Impedance spectroscopy (IS) was used to study the dielectric properties of the samples in the radiofrequency region (<300 MHz). Furthermore, the IS allowed the study of the nature of the impedances and determined the activation energy (Ea) which show that the additions of Bi₂O₃ contributed to the increase in the activation energy. The Nyquist diagram was used and, through an equivalent circuit formed by an association with two resistors, each in parallel with a constant phase element (CPE), it was possible to numerically determine the behaviors of the grain and contour grain effects of the ceramic samples. In addition to dielectric analysis, impedance spectroscopy measurements were carried out to study the nature of impedance, and the measured data was also fitted to the famous Cole–Cole spectrum. The contribution of the grain and grain boundary to the resistance and capacitance for Bi₂O₃ replacement was calculated from the theoretical fitted data. The capacitance coeficient of temperature (TCC) was obtained and its values demonstrate that the Bi₂O₃ additions caused an increase in the thermal stability of the composites in relation to the pure matrix.

Keywords Impedance spectroscopy · BiCu₃Ti₃FeO₁₂ · Ceramic composites · Bi₂O₃

✉ Roterdan Fernandes Abreu
roterdan.fernandes@gmail.com

1 Telecommunication Engineering Department, Federal University of Ceará (UFC), Fortaleza, Ceará 60755–640, Brazil

2 Physics Department—Federal University of Ceará (UFC), LOCEM-Telecommunication and Materials Science and Engineering of Laboratory (LOCEM), Campus PICI, P.O. Box 6030, Fortaleza, Ceará 60455–760, Brazil

3 Department of Organic and Inorganic Chemistry, Science Center, Federal University of Ceará (UFC), Fortaleza, Brazil

4 Federal Institute of Education, Science and Technology of Ceará, PPGET, Fortaleza, Ceará, Brazil

5 Group Functional Nanomaterials, Physics Department, Federal University of Sergipe, Sao Cristóvão, SE 49100–000, Brazil

6 Department of Materials Engineering, Leibniz Institute for Polymer Research Dresden– IPF, Hole Straße 6, 01069 Dresden, Germany

1 Introduction

Electro-ceramic composites are dielectric materials that have great potential in the application of electrical, electronic, and telecommunications components [1–3]. Ceramic composites that have parameters such as high permittivity, low dielectric loss, and high thermal stability are strategic targets for scientific and technological studies [4]. Among this class of materials, we can mention the ceramic matrix BiCu₃Ti₃FeO₁₂ (BCTFO), which is a potential candidate for obtaining new electronic devices operating at radio frequency (RF) and microwave (MW) [5, 6].

BCTFO presents a structure associated with perovskite [7, 8], and high permittivity in the RF and MW region, showing potential for application as a dielectric resonator antenna (DRA) [9, 10]. This fact inspires other works and analyses on this ceramic matrix, studies that have not been explored in the literature. The selection of bismuth

ANNEX I - PATENT APPLICATION: UM NOVO COMPÓSITO DE BiCu$_3$Ti$_3$FeO$_{12}$ (BCTFO) ADICIONADO COM ÓXIDO DE BISMUTO (Bi$_2$O$_3$) COM COEFICIENTE DE TEMPERATURA DA FREQUÊNCIA RESSONANTE (τ_f) PRÓXIMO DE ZERO NA REGIÃO DE MICRO-ONDAS.

(21) BR 102020005805-3 A2

República Federativa do Brasil
Ministério da Economia
Instituto Nacional da Propriedade Industrial

(22) Data do Depósito: 24/03/2020

(43) Data da Publicação Nacional: 05/10/2021

(54) Título: UM NOVO COMPÓSITO DE BICU 3 TI 3 FEO 12 (BCTFO) ADICIONADO COM ÓXIDO DE BISMUTO (BI 2 O 3) COM COEFICIENTE DE TEMPERATURA DA FREQUÊNCIA RES- SONANTE (T F) PRÓXIMO DE ZERO NA REGIÃO DE MICRO-ONDAS

(51) Int. Cl.: C25B 11/04; B82Y 40/00; B82Y 30/00.

(52) CPC: C25B 11/04; B82Y 40/00; B82Y 30/00.

(71) Depositante(es): UNIVERSIDADE FEDERAL DO CEARÁ.

(72) Inventor(es): ANTÔNIO SÉRGIO BEZERRA SOMBRA; DIEGO DA MOTA COLARES; DANIEL BARROS DE FREITAS; ROTERDAN FERNANDES ABREU; SEBASTIÃO JUNIOR TEIXEIRA VASCONCELOS.

(57) Resumo: UM NOVO COMPÓSITO DE BICU3TI3FEO12 (BCTFO) ADICIONADO COM ÓXIDO DE BISMUTO (BI2O3) COM COEFICIENTE DE TEMPERATURA DA FREQUÊNCIA RESSONANTE (?F) PRÓXIMO DE ZERO NA REGIÃO DE MICRO-ONDAS. Nesta patente um novo compósito BiCu 3 Ti 3 FeO 12 (BCTFO) adicionado com óxido de bismuto (Bi 2 O 3) nas proporções de 20% 40%, 60%, 80% e 93% foi fabricado e estudado na região de micro-ondas. O coeficiente de temperatura da frequência ressonante (t f) apresenta valores bastante interessantes, principalmente para o compósito de 93%, onde o valor de (t f) foi muito próximo de zero (+9,56 ppm/°C). Essas propriedades garantem que ele pode ser usado com segurança para o bom funcionamento de componentes em circuitos de micro-ondas, antena ressoadora dielétrica (DRA), além de outros componentes eletrônicos de grande importância utilizados em microeletrônica.
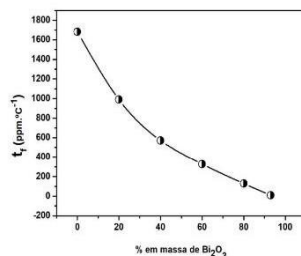
ANNEX J - PATENT APPLICATION: SÍNTESE E CARACTERIZAÇÃO DO COMPÓSITO DE VANADATO DE LANTÂNIO LaVO₄ (LVO) E DIÓXIDO DE TITÂNIO (TiO₂) COM COEFICIENTE DE TEMPERATURA DA FREQUÊNCIA DE RESSONANTE (τ_f) PRÓXIMO DE ZERO VISANDO A SUA APLICAÇÃO EM ENGENHARIA DE MICRO-ONDAS

República Federativa do Brasil
Ministério da Economia
Instituto Nacional da Propriedade Industrial

(21) BR 102020020636-2 A2

(22) Data do Depósito: 07/10/2020

(43) Data da Publicação Nacional: 19/04/2022

(54) Título: SÍNTESE E CARACTERIZAÇÃO DO COMPÓSITO DE VANADATO DE LANTÂNIO LAVO4 (LVO) E DIÓXIDO DE TITÂNIO (TIO2) COM COEFICIENTE DE TEMPERATURA DA FREQUÊNCIA DE RESSONANTE (TF) PRÓXIMO DE ZERO VISANDO A SUA APLICAÇÃO EM ENGENHARIA DE MICRO-ONDAS

(51) Int. Cl.: C01F 17/229; C01G 23/08.

(52) CPC: C01F 17/229; C01G 23/08; C01P 2006/40.

(71) Depositante(es): UNIVERSIDADE FEDERAL DO CEARÁ.

(72) Inventor(es): ANTONIO SERGIO BEZERRA SOMBRA; YGUATYARA DE LUNA MACHADO.; VALÉRIA LIMA BESSA; DIEGO DA MOTA COLARES; ANTÔNIO JEFFERSON OLIVEIRA DA SILVA; FRANCISCO NIVALDO AGUIAR FREIRE; JOÃO PAULO COSTA DO NASCIMENTO; TALLISON OLIVEIRA ABREU; MARCELO ANTONIO SANTOS DA SILVA.

(57) Resumo: Síntese e Caracterização do compósito de vanadato de lantânio LaVO4 (LVO) e dióxido de titânio (TiO2) com coeficiente de temperatura da frequência de ressonante (tf) próximo de zero visando a sua aplicação em Engenharia de microondas. Nesta patente, um novo compósito de vanadato de lantânio (LaVO4) e dióxido de titânio (TiO2) nas proporções de 13 %, 15 %, 20 % e 40% foram desenvolvidos e avaliados na região de micro-ondas. O coeficiente de temperatura da frequência de ressonante (tf) foi encontrado nas concentrações de 13 % e 15 %, apresentando os valores de 6,87 ppm/°C e 8,61 ppm/°C, respectivamente, os quais se encontraram dentro da faixa de limites aceitáveis entre (- 10 ppm/°C e + 10 ppm/°C) para a sua aplicação na região de micro-ondas. As propriedades obtidas, neste estudo, permitem que este compósito possa vir a ser utilizado em dispositivos eletrônicos, bem como possam garantir o funcionamento adequado de circuitos eletrônicos, da antena ressoadora dielétrica (DRA), dentre outros componentes eletrônicos de grande interesse industrial.
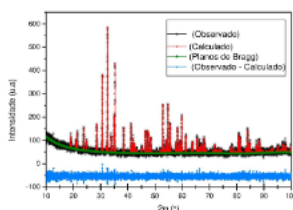
ANNEX K - PATENT APPLICATION: CRESCIMENTO DA ESTABILIDADE TÉRMICA DA MATRIZ ($Ba_2TiSi_2O_8$) COM ADIÇÃO DE TiO_2 PARA OPERAÇÃO NA REGIÃO DE MICRO-ONDAS.

República Federativa do Brasil

Ministério do Desenvolvimento, Indústria, Comércio e Serviços

Instituto Nacional da Propriedade Industrial

BR102021015932A2

(21) BR 102021015932-4 A2

(22) Data do Depósito: 12/08/2021

(43) Data da Publicação Nacional: 22/02/2023

(54) Título: CRESCIMENTO DA ESTABILIDADE TÉRMICA DA MATRIZ (BA2TISI2O8) COM ADIÇÃO DE TIO2 PARA OPERAÇÃO NA REGIÃO DE MICRO-ONDAS

(51) Int. Cl.: C04B 35/16.

(52) CPC: C04B 35/16; C04B 2235/3436; C04B 2235/3234; C04B 2235/9607.

(71) Depositante(es): UNIVERSIDADE FEDERAL DO CEARÁ.

(72) Inventor(es): ANTONIO SERGIO BEZERRA SOMBRA; ROTERDAN FERNANDES ABREU; DIEGO DA MOTA COLARES; TALLISON OLIVEIRA ABREU; FRANCISCO ALEKSON CHAVES NOBREGA; ANTONIO JEFFERSON OLIVEIRA DA SILVA; SAMUEL OLIVEIRA SATURNO; FELIPE RODRIGUES DA SILVA; JOÃO PAULO COSTA DO NASCIMENTO; YGUATYARA DE LUNA MACHADO.

(57) Resumo: CRESCIMENTO DA ESTABILIDADE TÉRMICA DA MATRIZ ($Ba_2TiSi_2O_8$) COM ADIÇÃO DE TiO PARA OPERAÇÃO NA REGIÃO DE MICRO-ONDAS. Algumas cerâmicas avançadas estão sendo utilizadas como dispositivos na região de micro-ondas, mas o problema é que a grande maioria destas não tem estabilidade térmica. No entanto, é necessário sintetizar um compósito cerâmico que opere na região de micro-ondas e tenha estabilidade térmica. Para solucionar este problema, nesta invenção é apresentado um novo compósito cerâmico, formado pela a matriz $Ba_2TiSi_2O_8$ com adição de óxido de titânio (TiO_2), que opere na região de micro-ondas e tenha estabilidade térmica. O compósito cerâmico foi sintetizado pela reação do estado sólido, em que os reagentes precursores $BaCO_3$, SiO_2 e TiO_2 foram calcinados a 1100 °C por 4 horas, após a calcinação a difração de Raios-X caracterizou a formação da matriz $Ba_2TiSi_2O_8$. Confirmada a formação da fase, foram adicionados TiO_2 na matriz e formando peças cilíndricas que foram sinterizadas a 1200 °C por 4 horas. Após a síntese foram obtidos compósitos formados pelo $Ba_2TiSi_2O_8$ e com adições de TiO_2 nas proporções de 10, 15, 20, 25, 30, 35 e 40%, que logo em seguida foram medidas sua estabilidade térmica. A estabilidade térmica foi obtida pelo método (...).
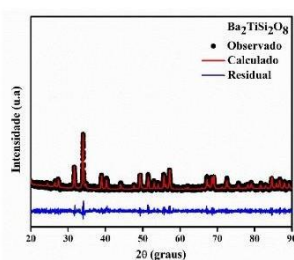
ANNEX L - PATENT APPLICATION: OBTENÇÃO DE NOVA MATRIZ DIELÉTRICA Sr$_2$TiSi$_2$O$_8$ (SILICATO DE ESTRÔNCIO-TITÂNIO) COM ALTA ESTABILIDADE TÉRMICA NA REGIÃO DE MICRO-ONDAS.

República Federativa do Brasil

Ministério do Desenvolvimento, Indústria, Comércio e Serviços

Instituto Nacional da Propriedade Industrial

(21) BR 102022015899-1 A2

(22) Data do Depósito: 11/08/2022

(43) Data da Publicação Nacional: 20/02/2024

(54) Título: OBTENÇÃO DE NOVA MATRIZ DIELÉTRICA SR2TISI2O8 COM ALTA ESTABILIDADE TÉRMICA NA REGIÃO DE MICRO-ONDAS

(51) Int. Cl.: H01L 23/14; H01L 23/15.

(71) Depositante(es): UNIVERSIDADE FEDERAL DO CEARÁ.

(72) Inventor(es): ANTONIO SERGIO BEZERRA SOMBRA; ROTERDAN FERNANDES ABREU; MARCELO ANTONIO SANTOS DA SILVA; FELIPE FELIX DO CARMO; DIEGO DA MOTA COLARES; FRANCISCO ALEKSON CHAVES NOBREGA; JOÃO PAULO COSTA DO NASCIMENTO; TALLISON OLIVEIRA ABREU.

(57) Resumo: OBTENÇÃO DE NOVA MATRIZ DIELÉTRICA SR2TISI2O8 COM ALTA ESTABILIDADE TÉRMICA NA REGIÃO DE MICRO-ONDAS. As cerâmicas dielétricas são constantemente utilizadas na fabricação de dispositivos que operam em circuitos eletrônicos na região de micro-ondas, mas um problema comum que estas apresentam é a falta de estabilidade térmica. Desta forma, sintetizar uma matriz cerâmica que opere na região de micro-ondas e possua alta estabilidade térmica, geralmente é um desafio para os pesquisadores. Nesse contexto, esta invenção propõe uma nova matriz cerâmica Sr2TiSi2O8 (STS) que opera na região de micro-ondas e possui uma alta estabilidade térmica. A matriz cerâmica Sr2TiSi2O8 foi sintetizada pela reação do estado sólido, em que os reagentes precursores (SrCO3, SiO2 e TiO2) foram misturados e moídos, formando a amostra que foi calcinada a 1200 °C por 6 horas. Para a caracterização do STS foi realizada a difração de Raios-X que confirmou a formação da fase cerâmica Sr2TiSi2O8. Confirmada a fase, pó resultante de STS foi compactado via pressão uniaxial de 16,5 MPa, obtido como resultado uma peça cilíndrica que foi sinterizada a 1300 °C por 4 horas. Após a síntese foi realizada a medida de Hakki-Coleman, obtendo os valores de (...).
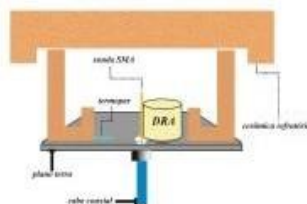
ANNEX M - PATENT APPLICATION: ALTA ESTABILIDADE TÉRMICA EM COMPÓSITOS FORMADOS A PARTIR DE Ba₂TiSi₂O₈ - CaTiO₃ PARA APLICAÇÕES NA REGIÃO DE MICRO-ONDAS

República Federativa do Brasil

Ministério do Desenvolvimento, Indústria, Comércio e Serviços

Instituto Nacional da Propriedade Industrial

(21) BR 102023003130-7 A2

(22) Data do Depósito: 17/02/2023

(43) Data da Publicação Nacional: 27/08/2024

(54) Título: ALTA ESTABILIDADE TÉRMICA EM COMPÓSITOS FORMADOS A PARTIR DE BA2TISI2O8 - CATIO3 PARA APLICAÇÕES NA REGIÃO DE MICRO-ONDAS

(51) Int. Cl.: C04B 35/46; C04B 35/468; H01C 7/04.

(52) CPC: C04B 35/46; C04B 35/468; C04B 2235/3436; H01C 7/045.

(71) Depositante(es): UNIVERSIDADE FEDERAL DO CEARÁ.

(72) Inventor(es): ANTONIO SERGIO BEZERRA SOMBRA; ROTERDAN FERNANDES ABREU; FRANCISCO ALEKSON CHAVES NOBREGA; SAMUEL OLIVEIRA SATURNO; TALLISON OLIVEIRA ABREU; DIEGO DA MOTA COLARES; FRANCISCO ENILTON ALVES NOGUEIRA; JOÃO PAULO COSTA DO NASCIMENTO; MARCELO ANTONIO SANTOS DA SILVA; FELIPE FELIX DO CARMO.

(57) Resumo: ALTA ESTABILIDADE TÉRMICA EM COMPÓSITOS FORMADOS A PARTIR DE Ba2TiSi2O8 - CaTiO3 PARA APLICAÇÕES NA REGIÃO DE MICRO-ONDAS. Este trabalho apresenta a proposta de patente de um novo compósito formado pela a matriz cerâmica $Ba_2TiSi_2O_8$ (BTS) com adições de $CaTiO_3$ (CTO) nas proporções de 1%, 3%, 5% e 9% em massa. A síntese do estado sólido foi empregada na produção do $Ba_2TiSi_2O_8$ (BTS). Na síntese da matriz cerâmica BTS foram utilizados os seguintes materiais precursores: $BaCO_3$ (99.99%,Vetec), TiO_2 (99.8%, Aldrich), e SiO_2 (99.9%, Aldrich). Os pós oriundos da mistura foram submetidos ao processo de moagem (360 rpm/4h) no moinho de alta energia Fritsch Pulverisette 5. Ao findar deste processo os pós foram calcinados (1100 °C/6h), em seguida compactados via pressão uniaxial (22, 20 utilizada para analisar MPa) e sinterizados (1200 oC/4h). A difração Raios-X (XRD) foi as estruturas das amostras, e através do Refinamento Rietveld as fases foram identificadas e os parâmetros da rede foram obtidos. O coeficiente de temperatura da frequência de ressonante (t f) das amostras foi calculado para estudar a estabilidade térmica dos materiais de acordo com o método de Silva-Fernandes-Sombra (SFS). O BTS apresentou um t f =- 47,00 ppm/°C. Entretanto, o melhor resultado foi obtido na (...).
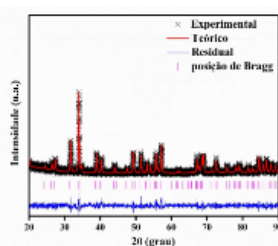
ANNEX N - PATENT APPLICATION: GRANDE ESTABILIDADE TÉRMICA DA MATRIZ DE Ba$_2$TiSi$_2$O$_8$ ADICIONADO COM SrTiO$_3$ PARA USO EM COMPONENTES NA REGIÃO DE MICRO- ONDAS.

SERVIÇO PÚBLICO FEDERAL
MINISTÉRIO DO DESENVOLVIMENTO, INDÚSTRIA, COMÉRCIO E SERVIÇOS
INSTITUTO NACIONAL DA PROPRIEDADE INDUSTRIAL

EXAME FORMAL PRELIMINAR – PEDIDO CONSIDERADO DEPOSITADO

N.º do Pedido:	BR102024016638-8	**N.º de Depósito PCT:**
Data de Depósito:	14/08/2024	

O pedido atende às condições formais estabelecidas pelo INPI na Portaria nº 14/2024 conforme disposto no art.19 da Lei da Propriedade Industrial (LPI) e é considerado como depositado.

Condições do Pedido	S	N
Formulário de depósito com os campos obrigatórios preenchidos	X	
Idioma Português	X	
Relatório Descritivo	X	
Reivindicações	X	
PI e CA – Apresenta desenhos (quando citados). MU – Apresenta desenhos.	X	
Resumo	X	
Formatado no padrão exigido	X	
Valor correto de Recolhimento	X	

Rio de Janeiro, 22 de novembro de 2024.

Andrea Massad Fonseca Barbosa
Mat. Nº 1466814
DIRPA / COSAP/SEFOR